Molecular mechanisms of von Willebrand Factor mechanoregulation

Arjen J. Jakobi

Arjen J. Jakobi
Molecular mechanisms of von Willebrand Factor mechanoregulation
Dissertation, Utrecht University, The Netherlands
ISBN 978-90-393-5821-4

Cover illustration by Juan Agüera and Arjen J. Jakobi

www.sodagraphics.com

Molecular mechanisms of von Willebrand Factor mechanoregulation

Moleculaire mechanismen betrokken bij de mechanoregulatie van von Willebrand Factor

(met een samenvatting in het Nederlands)

Proefschrift

ter verkrijging van de graad van doctor aan de Universiteit Utrecht op gezag van de rector magnificus, prof. dr. G.J. van der Zwaan, ingevolge het besluit van het college voor promoties in het openbaar te verdedigen op maandag 10 september 2012 des middags te 2.30 uur

door

Arjen-Joachim Jakobi

geboren op 29 oktober 1980,
te Wiesbaden, Duitsland

Promotor: Prof. dr. P. Gros
Co-promotor: Dr. E.G. Huizinga

Het in dit proefschrift beschreven onderzoek werd gefinancierd door de Nederlandse organisatie voor Wetenschapelijk Onderzoek (NWO), gebied Chemische Wetenschappen (CW).

Voor mijn ouders

Contents

Chapter 1 9
General Introduction: Molecular biophysics of von Willebrand Factor

Chapter 2 27
Calcium modulates force sensing in the von Willebrand Factor A2 domain

Chapter 3 47
Mechanistic studies of ADAMTS-13 substrate specificity

Chapter 4 69
A rapid cloning strategy employing orthogonal end protection

Chapter 5 85
General Discussion

Nederlandse samenvatting 97

Dankwoord 101

Curriculum vitae 105

CHAPTER 1

General Introduction

Arjen J. Jakobi
Crystal & Structural Chemistry, Bijvoet Center for Biomolecular Research, Department of Chemistry, Utrecht University, Padualan 8, 3584 CH Utrecht, The Netherlands

Injury of blood vessels necessitates robust mechanisms that rapidly seal off the disrupted endothelial cell layer to arrest excessive blood loss from circulation. In response to vascular damage, intricately regulated mechanisms lead to a chain of coordinated reactions that initially provoke activation and transient adhesion of platelets at the lesion, followed by permanent arrest and concomitant aggregation to form a primary platelet plug. At the same time, activation of the coagulation system mediates reinforcement of the haemostatic plug by polymerization of fibrin. Other mechanisms are in place to provide continuous feedback control in order to prevent the inadequate aggregation of platelets, which may otherwise lead to the pathologic occlusion of vessels (thrombosis). Significant hydrodynamic forces oppose the initial adhesion of platelets to the damaged vessel wall, particularly in small arterioles. Accumulating evidence suggests that these forces play an important role in maintaining haemostasis. In this introductory chapter we review recent progress in understanding force as a regulatory factor of platelet adhesion during this first and critical step of thrombus formation.

Platelets are indispensable for normal haemostasis, in particular in the rapid flow environment of small arterioles [1]. Endothelial cells lining the vessel wall constitute an inert surface over which platelets flow without interaction during normal vascular homeostasis. Upon vascular injury, the first step of bleeding arrest involves the adhesion of platelets to components of the subendothelial matrix that become exposed at the lesion. Hydrodynamic drag forces exerted by the blood flow counteract stable contacts of platelet receptors with matrix components, hampering firm adhesion at these thrombogenic surfaces. A comprehensive picture of the precise molecular mechanisms that regulate primary haemostasis therefore necessitates consideration of the particular hydrodynamic conditions and associated forces that affect dynamics and biological function of the adhesion molecules.

In vascular shear flow the distribution of fluid velocities across a vessel follows a characteristic profile with highest fluid velocity in the center and zero velocity at the vessel wall [2, 3] (**Fig. 1**). This velocity profile induces friction between adjacent fluid layers (lamina) and thereby generates shear stress on objects across such lamina. As a consequence,

the adhesion of platelets to vascular lesions is complicated by substantial shear gradients that generate tensile forces on adhesive bonds between ligands of the injured vessel wall and their corresponding adhesion receptors on the platelet surface. These shear gradients and associated tensile forces limit contact time (on-rate) and impinge on lifetime (off-rate) of adhesive interactions. Accordingly, the efficiency of the interaction of platelets with thrombogenic surfaces decreases with increasing shear rates [4]. The situation is further aggravated in small arterioles and capillaries. In the microvasculature, the confined vessel lumen leads to steep in velocity gradients and increased shear rate and shear stress [5]. To oppose these hydrodynamic forces and efficiently deposit platelets at vascular lesions in the microvascular system, the adhesion process under these conditions critically depends on the multimeric plasma glycoprotein **von Willebrand Factor** (VWF) [6].

VWF functions as a vessel wall damage sensor and, at high shear rates, serves as a molecular bridge in mediating transient adhesion of fast flowing platelets to subendothelial matrix collagen [6, 8-11] (**Fig. 2**). Recent years have seen rapid progress in understanding the molecular biophysics of VWF that underlie its haemostatic function and firmly established its role as a mechanical sensor protein regulated by hydrodynamic shear forces.

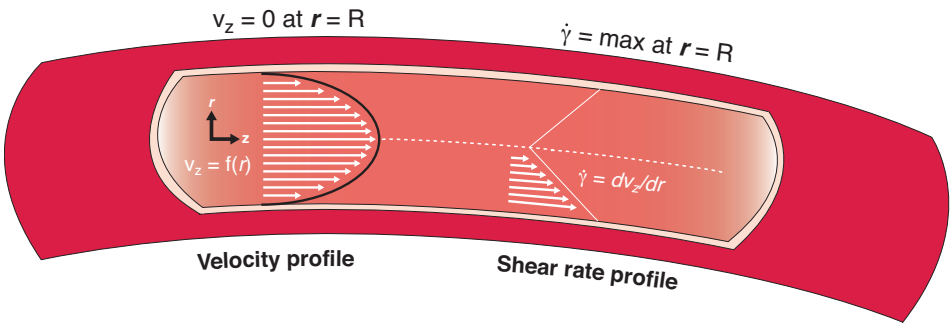

Figure 1: Schematic representation of radial velocity and shear rate profiles in a cylindrical blood vessel. Laminar blood flow can be approximated by an axisymmetric, parabolic velocity profile with highest velocity in the center of the vessel lumen and zero velocity at the vessel wall. Conversely, the shear rate g, defined as the gradient of the radial velocity profile, is zero at the center of the vessel and reaches its maximum at the vessel wall. White arrows represent radial velocity (left) or shear rate (right). The dashed line indicates the central axis (modified from [7]).

Structure and Function of Von Willebrand Factor

VWF has a central role in platelet-dependent primary haemostasis and thrombosis, particularly in the rapid flow environment of the microvascular circulation. Large VWF multimers support the adhesion of platelets to vascular lesions at high shear rates (> 500-800 s^{-1}) by binding to fibrillar collagen at the exposed subendothelial matrix and to the GPIbα subunit of the GPI-IX-V receptor complex on the platelet surface [12]. Although generally not sufficient for platelet arrest, the interaction with collagen-immobilized VWF results in deceleration of platelets relative to blood flow. The initial tethering via GPI-IX-V then triggers a signaling cascade that leads to activation of platelet integrin $a_{IIb}\beta_3$ [13, 14], which together with integrin $\alpha_2\beta_1$ [15] and GPVI [16] contributes to stable platelet adhesion and

thrombus growth. In addition to its adhesive function, VWF acts as a protective carrier for coagulation factor VIII (FVIII), which is rapidly cleared from circulation in the absence of VWF [17-19]. Mutations in VWF can compromise quantitative or qualitative aspects of VWF-mediated platelet adhesion and strongly impede efficient bleeding arrest. Paradoxically, mutations that increase and those that decrease platelet affinity of VWF equally result in bleeding [20].

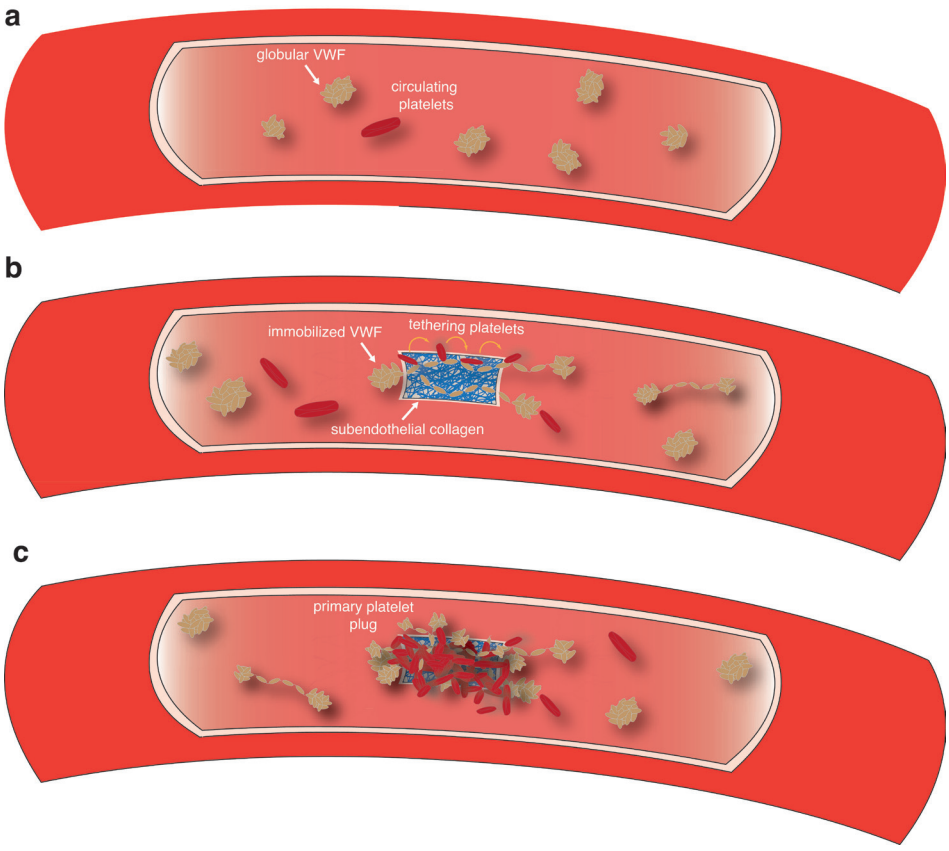

Figure 2: VWF mediates primary haemostasis at high shear. (a) In the absence of vascular injury and at low shear rates, platelets and globular VWF circulate without appreciable interaction in plasma. (b) VWF recognizes and binds fibrillar collagen (blue fibres) that becomes exposed at vascular lesions. Immobilized VWF assumes an elongated conformation and exposes binding sites for platelets. Platelets transiently tether to the VWF-coated lesion by interaction of the platelet GPIba receptors with the A1 domain in VWF. (c) Platelets stably interact with the collagen via their own integrin receptors and GPVI and self-associate to form aggregates that seal off the vascular lesion.

Biosynthesis And Secretion of VWF multimers

VWF is synthesized by endothelial cells [21] and platelet precursor megakaryocytes [22] as a linear multimer comprising up to several hundred monomeric subunits, which are covalently linked by disulphide bonds. The monomeric pro-VWF sequence is composed of repeated domain motifs arranged in the order D1-D2-D'-D3-A1-A2-A3-D4-B1-B2-B3-C1-C2-CK [12, 23] (**Fig. 3a**). The primary 2813 residue translation product (pre-pro-VWF) [24] consists of a 22 residue signal peptide, a large 741 residues propeptide (domains D1-D2) and the mature monomeric subunit of 2050 residues (domains D'-CK) [25]. The subsequent synthesis and intracellular storage of the multimeric protein chains poses a formidable challenge to the cellular machinery. The assembly of multimeric VWF initiates at the ER, where the pro-VWF monomer (domains D1-CK) undergoes extensive glycosylation [23, 25] and self-associates to form covalent homodimers by engaging interchain

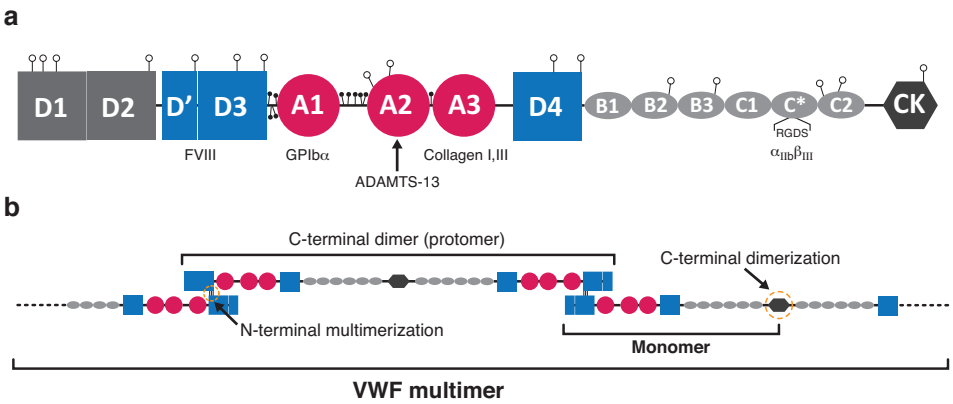

Figure 3: VWF domain architecture and multimerization. (a) VWF domain organization in pro-VWF. The propeptide consisting of the D1D2 domains is cleaved in the Golgi compartment. The mature polypeptide starts at domain D'. Open circles represent N-linked glycans; closed circles are O-linked glycans. Although the sequence between C1 and C2 has not been assigned to a domain family, electron microscopy analysis demonstrates that this sequence has a globular fold [48], hereafter referred to as C*. Important interaction sites are indicated. (b) Multimerization of VWF. Monomer units dimerize at the carboxyl-terminal CK domain to form the repeating unit (protomer) of multimeric VWF. Multimers assemble from protomers via the formation of head-to-head interchain disulphide bonds between adjacent amino-terminal D3 domains.

disulfide bonds between carboxyl-terminal cysteine knot (CK) domains [23, 26-29]. These tail-to-tail dimers are subsequently translocated to the Golgi compartment, where the propeptide is proteolytically cleaved off, presumably by furin [30, 31], and VWF homodimers concatamerize head-to-head at the amino termini by additional interchain disulphide linkages [32, 33] that form between the D3 domains [31, 34] (**Fig. 3b**).

During this process the cleaved propeptide remains associated with the mature protein chain [35] and is assumed to function as an endogenous oxidoreductase required to direct covalent multimerization of VWF in the acidic and chaperone-depleted environment of the *trans*-Golgi network [36-41]. In endothelial cells, ultra-large VWF multimers (ULVWF), which are most active in their capacity to bind GPIbα [42], are assembled into tubular supramolecular structures that are incorporated into nascent vesicles referred to as Weibel-

Palade bodies (WPBs) [43, 44]. WBPs are secretory granules of the regulated secretory pathway [44-46]. Upon stimulation by agonists, ULVWF is released from these storage granules. During normal catabolism these hyper-reactive ULVWF multimers are converted into a series of smaller multimers, mainly by cleavage of the Tyr1605-Met1606 bond within the A2 domain of VWF [47] (see below).

Functional aspects of VWF

Within VWF, the majority of domains for which a discrete function in haemostasis has been characterized, concentrate in the amino-terminal D'D3-A1-A2-A3 region (see **Fig. 3a**). The D3 domain is involved in head-to-head concatamerization of VWF [34] and in its dimeric form provides a binding platform for FVIII [18, 19]. The triple repeat of homologous VWF A-type domains carries the core of the haemostatic functionality. The A1 domain binds to the leucine-rich repeat (LRR) domain of the platelet receptor GPIbα [49-51] as well as heparin [50] and collagen type VI [52, 53]. The A2 domain contains a cleavage site for the metalloprotease ADAMTS-13 (a disintegrin and metalloproteinase with a thrombospondin-1 motif, member 13) [54-56] and has a function in size regulation of VWF multimers. The A3 domain holds a predominant role as the damage sensor domain of VWF by binding to collagen types I and III [57, 58]. Patient mutations resulting in functional deficiencies of these domains manifest in different forms of von Willebrand disease (VWD) [20], characterized by bleeding.

The function of carboxyl-terminal domains D4-B1-B2-B3-C1-C2-CK is less well defined. The D4 domain has been implicated in recognition of VWF by ADAMTS-13 [59]. The C-terminal C* domain (**Fig. 3**) contains an Arg-Gly-Asp-Ser (RGDS) sequence that is recognized by activated platelet integrin $\alpha_{IIb}\beta_3$ (GPIIb/IIIa) [60-62]. In contrast to the A1/GPbα interaction that only mediates transient tethering, binding of $\alpha_{IIb}\beta_3$ by VWF and fibrinogen contributes to stable platelet adhesion, spreading and aggregation [62, 63]. The absence of clinically relevant mutations in patients with VWD, however, questions an important physiological role of this sequence in VWF-mediated haemostasis.

Regulation of VWF function by hydrodynamic shear stress

One important aspect of platelet adhesion to VWF is that circulating VWF, in the absence of modulators, has no appreciable interaction with non-stimulated platelets at low shear rates, but paradoxically is very effective in mediating platelet tethering to vascular lesions at high shear rates [14, 64]. At low shear rates, adhesion of platelets to sites of vessel injury can occur independently of VWF via the platelet collagen receptor $\alpha_2\beta_1$ [65] or via binding of integrin $\alpha_{IIb}\beta_3$ to fibrinogen [6]. At high shear rates, the tethering of platelets to thrombogenic surfaces critically depends on the fast association kinetics of the GPIbα interaction with VWF-A1 and is particularly efficient in the presence of ultra-large immobilized VWF multimers [66]. The length of VWF multimers is therefore pivotal to their haemostatic potency. ULVWF multimers released from endothelial cells in response to acute injury were estimated to 50 x 10^6 M_r [67], whereas recent estimates suggest that freshly released surface-bound VWF strings may exceed 10^9 M_r [48]. Both activation of

VWF-mediated platelet recruitment and feedback regulation of its effectiveness appear to be intimately linked to the particular hydrodynamic conditions in the microvasculature.

VWF undergoes conformational changes in response to hydrodynamic forces

The functional relationship between platelet binding capacity, molecular size and shear rate suggests that VWF undergoes shear-dependent conformational changes that prime it for platelet recruitment, and that the probability for these structural transitions is related to multimer length. The overall structure of VWF multimers at physiological pH is highly flexible with repeating monomer units that show an organization of variably sized, closely interspaced beads on a flexible string [48, 67, 68]. In the absence of shear, VWF usually organizes in compact globular structures as observed by electron microscopy [67, 68]. Atomic force microscopy (AFM) experiments demonstrated that the application of shear results in a conformational transition of VWF from a condensed structure in stasis to an unfurled (extended) conformation at a fluid shear rate of approximately 3000 s^{-1} [69]. These results hold important functional consequences: In a compact, globular conformation of VWF platelet binding sites in the A1 domains are presumably buried, preventing unintended interaction with, and aggregation of, platelets under normal conditions. This hypothesis is supported by biochemical data demonstrating that the isolated recombinant A1 domain, but not multimeric VWF, has high affinity for GPIbα in the absence of shear (references). High shear gradients may be the relevant factor to overcome the threshold inducing the conformational transition to the extended conformation, which exposes the A1 domain for platelet recruitment. Indeed, using a microfluidic flow chamber and fluorescently labeled VWF, an abrupt conformational transition of freely suspended VWF from a collapsed to an extended state was observed when exceeding a critical shear threshold, even in the absence of adsorbing surfaces [70]. Importantly, the transition was found to be reversible and extended VWF molecules condense back to the collapsed conformation upon relaxation [70]. It is important to realize that, in the physiological situation, this stretching transition will preferentially occur at, or close to the vessel wall, where the velocity gradient is steepest and, thus, shear rates are maximal (see **Fig. 1**). This implies that the likelihood of the conformational transition to the extended, high affinity conformation will be highest precisely where activated VWF is required for platelet adhesion. Threshold-controlled conformational changes of VWF thus contribute to the regulation of VWF in response to a particular hydrodynamic environment by conferring switchable binding to both GPIbα on circulating platelets and to reactive components of the subendothelial matrix.

Monomer size and multimer length are key determinant of haemostatic potency

The unique threshold-dependent transition of VWF conformation can be understood from the general theoretical framework describing structural dynamics of collapsed homopolymers in shear flow [71]. A coupling of hydrodynamic drag and thermally induced protrusions in such idealized spherical polymer compactions is proposed to result in tensile stretching forces that induce reversible extension above a sharply defined threshold shear rate [72, 73]. An important concept in this context is that simple shear flow can

be conceived as a linear superposition of equally partitioned rotational and elongational components [72, 74] (**Fig. 4a**). In such a convoluted flow profile extensible particles will tumble and, above a certain shear threshold, will oscillate between extended and compact conformations [71-73] (**Fig. 4b**). Extensional force strongly correlates with the size of the polymer chain, since terminal protrusions in different shear lamina will have maximal separation in the largest multimers. Clearly, the tendency to stretch is then inversely related to the interaction free energy of cohesive self-association between individual monomer units.

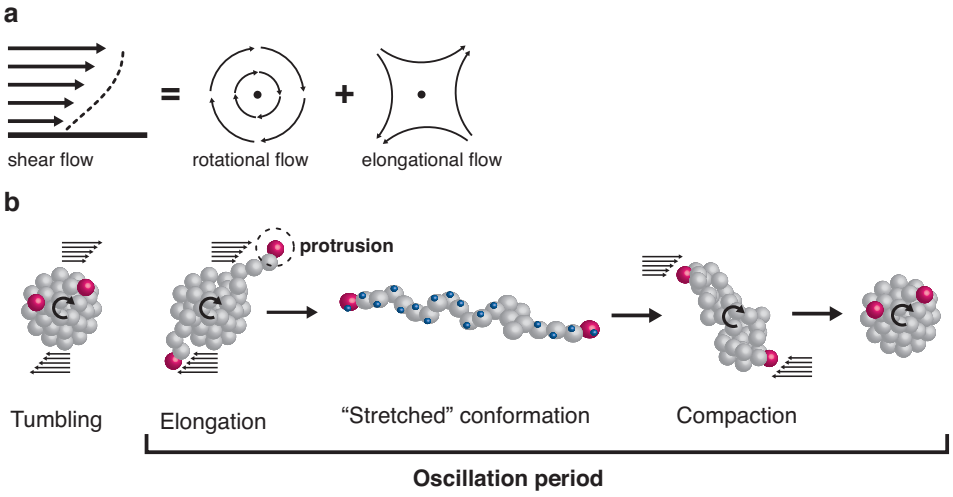

Figure 4: Shear flow and conformation of VWF multimers. (a) Characteristic laminar veolcity profile in shear flow. Individual lamina are represented by arrows. Shear flow can be conceptualized as a superposition of rotational components (inducing tumbling) and elongational flow components (inducing stretch). Modified from [71]. (b) The effect of shear flow on conformation of VWF multimers. Grey spheres represent individual monomer units. Terminal monomers are highlighted in magenta. Compact VWF will tumble in shear flow (far left). The presence of stochastic protrusions in different shear lamina induces stretching forces on the multimers (left) and leads to elongation and exposure of GPIbα binding sites (middle; blue spheres). Continuous tumbling results in velocity reversal of the termini and induces oscillation between stretched and compact conformations.

In addition, a linear and inverse dependence exists between the critical shear rate and monomer size [72, 73]. This implies that large repeating units lower the threshold of the unfolding transition and may explain the remarkable dimensions of VWF monomers (60-82 nm per monomer [48, 67]). Therefore, both VWF monomer size and multimer length are important factors contributing to the adhesive properties of VWF, presumably via a protrusion-induced mechanism that results in threshold-defined conformational changes.

A hierarchical model of VWF affinity modulation by force

Much effort in understanding VWF dynamics in response to shear forces has initially focused on overall conformational changes at the level of multimers. In addition to such changes, accumulating evidence suggests that tensile forces may similarly affect the tertiary structure of individual domains. Analogous to allosteric modulators, tensile force can transmit conformational changes that affect functional sites. Using single-molecule manipulation techniques such dynamics have for example been described for P-selectin [75],

cadherins [76], the bacterial adhesion receptor FimH [77], and have also been suggested for TGFβ [78] and integrins [79]. Several studies have put forward that similar structural dynamics may also exist in VWF. Biochemical studies demonstrated that both length and sequence of its flanking peptides strongly modulate affinity of the A1 domain for GPIbα [80, 81]. Crystal structures established that the conformation of amino- and carboxyl-terminal peptides flanking the isolated A1 domain [82, 83] differ substantially from that of A1 in complex with GPIbα [84, 85]. The flanking peptides in the A1 structures appear to approach one of the GPIbα interaction sites in the absence of the ligand, whereas in the complex structure they are displaced and protrude away from the domain. This lends support to the hypothesis that shear forces acting on immobilized VWF multimers may induce an extended conformation of these flanking peptides and thereby stabilize A1 in a high affinity state [86]. In accordance with this surmise, many VWD type 2B mutations locate in the terminal sequences or at sites contacting these flanking peptides [87]. Type 2B VWD is characterized by a gain-of-function phenotype with increased affinity for GPIbα [84], which paradoxically manifests as a bleeding tendency [20]. In analogy to type 2B VWD resulting from mutations in the A1 domain, mutations in GPIbα that increase affinity for VWF establish the identical clinical phenotype in platelet-type pseudo-VWD (ptVWD) [88, 89]. Dynamic force spectroscopy was used to demonstrate that such mutations affect dissociation kinetics under force [90]. It was proposed that A1 forms catch bonds with GPIbα, based on a force-dependent bond lifetime that increased with increasing force [91]. Very recently, single-molecule studies using a single chain ligand-and-receptor construct have challenged this view and instead suggested that the A1-GPIbα complex follows two distinctly different dissociation pathways and exhibits force-dependent switching between low affinity and high affinity states [92]. This argument was based on the interesting observation that the bond dissociation force changed from a unimodal to a bimodal distribution as a function of pulling rate, both of which show exponential decrease in lifetime with increase of force [92]. The observation that the antibiotic ristocetin, a compound known to mimic shear-dependent affinity maturation of the A1-GPIbα complex, modulated the equilibrium between both states [92] further substantiates this view. These data suggest that VWF has the ability to engage in interactions with GPIbα over a broad range of tensile forces by dynamically switching between different binding modes in response to the particular hydrodynamic conditions.

Substrate control in shear-dependent size regulation of VWF

Shear-dependent regulation of VWF function is not restricted to activation of platelet binding via A1/GPIbα. Upon secretion by stimulated endothelial cells, ULVWF strings are rapidly converted into smaller, less haemostatically active multimers through cleavage by the metalloprotease ADAMTS-13 at the Tyr1605-Met1606 bond in the A2 domain [54, 56, 93-95]. Only large VWF multimers are effective in supporting platelet adhesion under shear stress, but also constitute a potential threat for thrombosis during normal vascular homeostasis. As a consequence, ADAMTS-13 cleavage is an important mechanism to restrict the high avidity of ULVWF to the immediate vicinity of acute vascular injury.

Pathological conditions under which this process is inhibited by congenital or acquired deficiency of ADAMTS-13 result in a severe thrombotic microangiopathy referred to as thrombotic thrombocytopenic purpura (TTP). TTP is characterized by the abundant formation of platelet-rich thrombi in the microvasculature [42, 96, 97]. Contrary, mutations in the A2 domain that presumably increase susceptibility to cleavage by ADAMTS-13 result in depletion of ULVWF multimers from plasma and are causative for the bleeding tendency of type 2A VWD [20].

While VWF is resistant to cleavage by ADAMTS-13 under static conditions, it is readily cleaved to smaller multimers under conditions of high fluid shear stress [54-56] or the

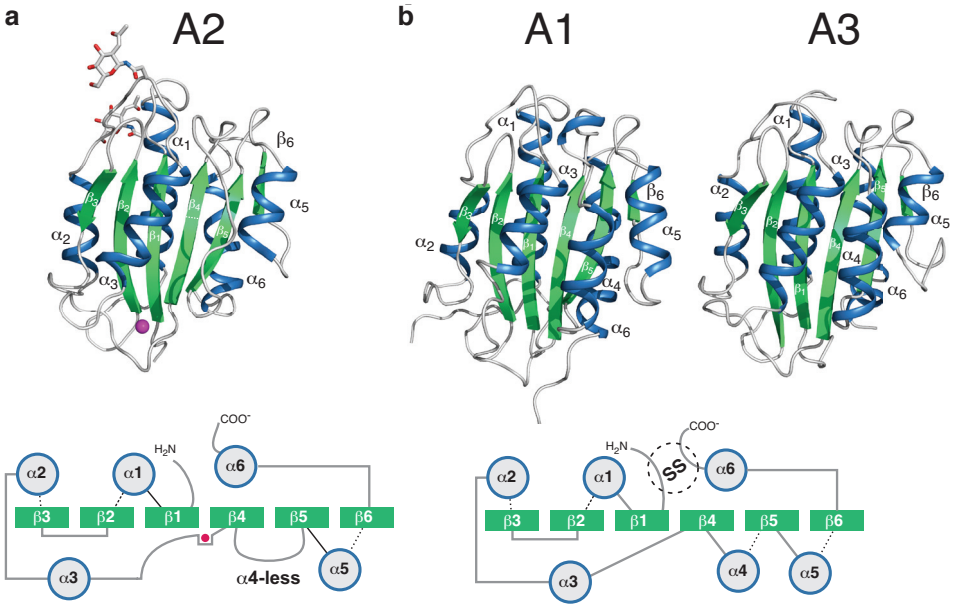

Figure 5: VWA-type domains in VWF. (a) Crystal structure of the A2 domain shown in cartoon representation (top; PDB ID 3zqk, **chapter 2**) and schematic sketch of the topology (bottom). Note the absence of the canonical α_4 helix. (b) Crystal structures of A1 (PDB ID 1auq, top left) and A3 (PDB ID 1atz, top right) and the associated topology (bottom). Contrary to A2, amino- and carboxyl termini of A1 and A3 are covalently connected by disulphide bridges (dashed circle).

presence of denaturating agents [56]. Crystal structures of the human VWF-A2 domain demonstrated that the scissile Tyr1605-Met1606 bond is inaccessible if A2 is in its native, folded conformation [98, 99] (**Fig. 5a** and **chapter 2**). This suggested that tensile forces from elongational flow induce local conformational changes that expose this bond for efficient cleavage by ADAMTS-13. Single-molecule optical tweezer experiments in which individual A2 domains were mechanically unfolded and exposed to ADAMTS-13 definitely established that the force-induced collapse of the native conformation of A2 is required for proteolytic cleavage [100] and occurs at time and force scales relevant *in vivo* ([100, 101] and **chapter 2**). Interestingly, polymer dynamics predict that tensile force on extended polymer chains scales with molecular weight, i.e. monomer number from each end of

the chain [102-104]. If a linear multimer is fully aligned along the direction of tensile load, forces are parabolically distributed along the extended polymer with the highest forces concentrated at the center of the chain [105] (**Fig. 6a**). Applied to ULVWF multimers in an elongational flow field, this concept defines large molecules to be the most susceptible substrate for ADAMTS-13 and successfully predicts the upper molecular weight limit of circulating VWF multimers found *in vivo* [100].

The A2 domain has evolved a number of unique structural features to adopt this mechanosensory function. Within immobilized VWF multimers, tensile force will be transmitted on individual domains via their respective amino- and carboxyl termini. In the neigbouring homologous A1 and A3 domains, amino- and carboxyl termini are structurally adjacent and connected via a disulphide bond between conserved cysteine residues (**Fig. 5b**). This architecture transmits the local tensile force directly from the amino- to the carboxyl terminus (and vice versa) via the disulphide bond and thereby effectively protects the secondary structural elements of the VWA fold from pulling forces. This mechanism leaves the conformation of the GPIbα and collagen binding sites unaffected by hydrodynamic drag on multimeric VWF. Unlike the A1 and A3 domains, A2 lacks the amino-terminal cysteine residue and instead forms a vicinal disulphide bond between two adjacent cysteine residues at its carboxyl terminus (**Fig. 5a**). The lack of a long range disulphide bond has important implications for the force-bearing topology, since in this case shear-induced pulling forces will be transmitted through the entire sequence of the A2 domain and act on individual secondary structural elements that are stabilized in their native conformation only by non-covalent interactions.

Owing to the topology of the VWA fold (**Fig. 5a**) and the lack of the long-range disulphide bridge, A2 is uniquely set to unfold from the carboxyl terminus in response to tensile forces ([98] and **chapter 2**). Force-probe molecular dynamics simulations indeed suggest that unfolding starts at the carboxyl-terminal α_6-helix and successively proceeds up to the scissile β_4-strand [106] (our own unpublished data). This conjecture is consistent with the finding that the carboxyl-terminal A2 residues Asp1596-Arg1668 (VWF73) constitute a minimal substrate for ADAMTS-13 [107]. Several key substrate recognition sites of ADAMTS-13 and essential residues within VWF73 have been identified by epitope mapping with autoinhibitory antibodies [108-111] and with variants of ADAMTS-13 or the VWF73 peptide [108, 112, 113] (**Fig. 6b** and **chapter 3**). ADAMTS-13 also binds to globular VWF with a K_D of ~ 50-90 nM [114], but does not cleave the substrate. Domains distal to the spacer domain (TSP5-8 and CUB1-2) mediate this interaction, presumably by binding to the D4 domain in VWF [59]. The affinity of ADAMTS-13 markedly increases in the presence of shear forces (K_D ~ 14 nM) [115], which is also the prerequisite for proteolysis to occur. The increased affinity depends on interactions of several exosites within the DTCS domains with a number of key residues in the carboxyl-terminal (VWF73) sequence of the A2 domain [112, 113, 116-120]. These residues are buried if A2 is in its native, folded conformation ([98] and **chapter 2**). Of importance in this context, a crystal structure spanning the disintegrin through spacer (DTCS) domains of ADAMTS-13 revealed an stretched-out arrangement of key substrate interaction sites [119], suggesting a model in which an elon-

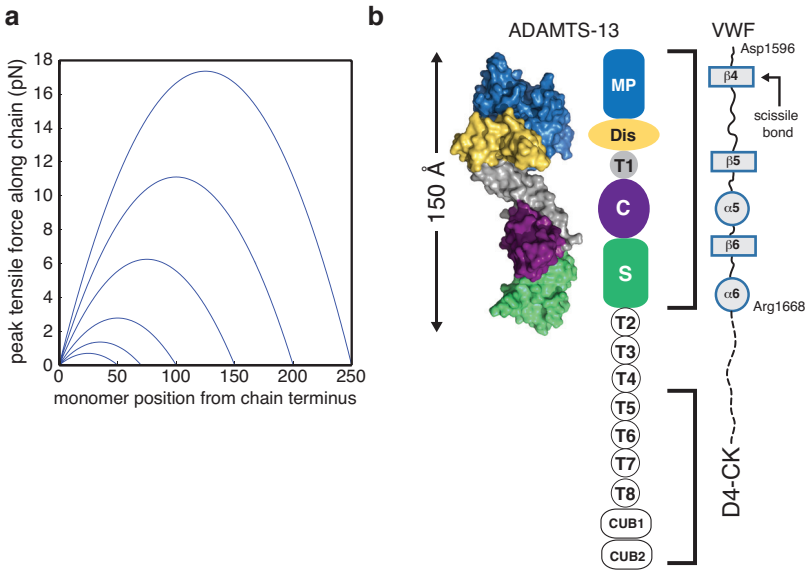

Figure 6: Forces on VWF multimers and ADAMTS-13. (a) Predicted peak forces on VWF multimers of varying length. Force is propagated throughout the chain and reaches its maximum at the chain center. Distributions are representative of 12 Nm^{-2}. Derived from polymer theory according to [100] (b) ADAMTS-13 binds an elongated substrate. The crystal structure of ADAMTS-13 DTCS domains (PDB ID 3ghm) (shown together with a homology model of the MP domain) reveals a linearly stretched-out domain arrangement (left). Domain organization of ADAMTS-13 (middle) and interaction sites with VWF. The carboxyl-terminal residues Asp1596-Arg1668 of the A2 domain bind across the MDTCS domains of ADAMTS-13, interacting with several topologically distant exosites to position the scissile bond. TSP5-CUB2 of ADAMTS-13 interact with several sites in the D4-CK sequence of VWF (right).

gated A2 substrate (residues Asp1596-Arg1668) binds across the ADAMTS-13 surface to position the scissile bond in the active site of the metalloprotease domain (**Fig. 6b**).

Proteolytic regulation is a common theme in haemostasis. Remarkably, ADAMTS-13 in circulation is constitutively active and the cleavage of VWF by ADAMTS-13 seems to differ from many of these proteolytic processes in the absence of a specific regulatory inhibitor. Instead, much of the current evidence from structural and biochemical studies supports a mechanism in which size regulation of VWF is predominantly driven by shear-dependent substrate availability that depends on force-induced conformational changes, leading to unfolding and exposure of the scissile bond. Upon unfolding, tensile force will stabilize an elongated substrate conformation that appears to be necessary for positioning the scissile bond in order for ADAMTS-13 to cleave [119] and possibly explains the increased affinity of mechanically stretched substrate relative to static assays [100].

Conclusion and scope of this thesis

VWF-mediated platelet adhesion appears to fit an hierarchical model of mechanoregulation, which is driven by shear-induced conformational changes ranging from threshold controlled unfurling of large VWF multimers to local conformational dynamics at the level of individual domains. A detailed understanding of structure and dynamics of VWF in response to tensile forces is therefore essential to comprehend the conformational complex-

ity underlying its haemostatic function. This thesis describes the structural and functional characterization of the central mechanoresponsive sensor domain in VWF. In **chaper 2**, we present the crystal structure of the human VWF-A2 domain and indentify a novel calcium-binding site. Using optical tweezers, we demonstrate at the single-molecule level that calcium binding at this site is a central element of the force sensing properties of VWF. Our data show for the first time that a calcium-dependent unfolding/refolding equilibrium regulates substrate availability in ADAMTS-13 cleavage and thereby haemostatic potency of VWF multimers in response to tensile forces. In **chapter 3** we characterize the specificity of the ADAMTS-13 metalloprotease domain toward its substrate VWF and propose a model for the ADAMTS-13 substrate interaction. Our biochemical data, in conjunction with molecular dynamics simulations, provide mechanistic insight into how the metalloprotease domain confers specificity to the scissile bond. In **chapter 4** we present a novel method that permits the rapid assembly of complex open reading frames by applying general concepts from synthetic chemistry to the in vitro assembly of DNA building blocks. We illustrate the applicability of this method by assembling genes encoding tandem repeat proteins for single-molecule studies. These results are summarized and discussed in **chapter 5**.

References

1. Sixma JJ, Wester J (1977)The hemostatic plug. *Semin Hematol* **14**: 265–99.
2. Baez S (1977) Microcirculation. *Annu Rev Physiol* **39**: 391–415.
3. Popel AS, Johnson PC (2005) Microcirculation and Hemorheology. *Annu Rev Fluid Mech* **37**: 43–69.
4. Ruggeri ZM, Mendolicchio GL (2007) Adhesion mechanisms in platelet function. *Circ Res* **100**: 1673–85.
5. Tangelder GJ, Slaaf DW, Arts T, Reneman RS (1988) Wall shear rate in arterioles in vivo: least estimates from platelet velocity profiles. *Am J Physiol* **254**: H1059–64.
6. Savage B, Saldívar E, Ruggeri ZM (1996) Initiation of platelet adhesion by arrest onto fibrinogen or translocation on von Willebrand factor. *Cell* **84**: 289–97.
7. Colman RW, Marder VJ, Clowes AW, George JN, Goldhaber SZ (2006) Hemostasis and Thrombosis: Basic Priciples and Clinical Practice. Lippincott Williams & Wilkins.
8. Packham MA, Mustard JF (1984) Platelet adhesion. *Prog Hemost Thromb* **7**: 211–88.
9. Packham MA, Mustard JF (1986) The role of platelets in the development and complications of atherosclerosis. *Semin Hematol* **23**: 8–26.
10. Ruggeri ZM (1995) The role of von Willebrand factor and fibrinogen in the initiation of platelet adhesion to thrombogenic surfaces. *Thromb Haemost* **74**: 460–3.
11. Sakariassen KS, Bolhuis PA, Sixma JJ (1979) Human blood platelet adhesion to artery subendothelium is mediated by factor VIII-Von Willebrand factor bound to the subendothelium. *Nature* **279**: 636–8.
12. Sadler JE (1998) Biochemistry and genetics of von Willebrand factor. *Annu Rev Biochem* **67**: 395–424.
13. Ikeda Y, Handa M, Kamata T, Kawano K, Kawai Y, Watanabe K, Kawakami K, Sakai K, Fukuyama M, Itagaki I (1993) Transmembrane calcium influx associated with von Willebrand factor binding to GPIb in the initiation of shear-induced platelet aggregation. *Thromb Haemost* **69**: 496–502.
14. Ikeda Y, Handa M, Kawano K, Kamata T, Murata M, Araki Y, Anbo H, Kawai Y, Watanabe K, Itagaki I (1991) The role of von Willebrand factor and fibrinogen in platelet aggregation under varying shear stress. *J Clin Invest* **87**: 1234–40.
15. Moroi M, Jung SM (2007) A mechanism to safeguard platelet adhesion under high shear flow: von Willebrand factor-glycoprotein Ib and integrin alphabeta-collagen interactions make complementary, collagen-type-specific contributions to adhesion. *J Thromb Haemost* **5**: 797–803.
16. Moroi M, Jung SM, Shinmyozu K, Tomiyama Y, Ordinas A, Diaz-Ricart M (1996) Analysis of platelet adhesion to a collagen-coated surface under flow conditions: the involvement of glycoprotein VI in the platelet adhesion. *Blood* **88**: 2081–2092.
17. Brinkhous KM, Sandberg H, Garris JB, Mattsson C, Palm M, Griggs T, Read MS (1985) Purified human factor VIII procoagulant protein: comparative hemostatic response after infusions into hemophilic and von Willebrand disease dogs. *Proc Natl Acad Sci USA* **82**: 8752–6.
18. Bahou WF, Ginsburg D, Sikkink R, Litwiller R, Fass DN (1989) A monoclonal antibody to von Willebrand factor (vWF) inhibits factor VIII binding. Localization of its antigenic determinant to a nonadecapeptide at the amino terminus of the mature vWF polypeptide. *J Clin Invest* **84**: 56–61.
19. Foster PA, Fulcher CA, Marti T, Titani K, Zimmerman TS (1987) A major factor VIII binding domain resides within the amino-terminal 272 amino acid residues of von Willebrand factor. *J Biol Chem* **262**: 8443–6.
20. Sadler JE (2005) New concepts in von Willebrand disease. *Annu Rev Med* **56**: 173-91.
21. Jaffe EA, Hoyer LW, Nachman RL (1974) Synthesis of von Willebrand factor by cultured human endothelial cells. *Proc Natl Acad Sci USA* **71**: 1906–9.
22. Nachman R, Levine R, Jaffe EA (1977) Synthesis of factor VIII antigen by cultured guinea pig megakaryocytes. *J Clin Invest* **60**: 914–21.
23. Wagner DD (1990) Cell biology of von Willebrand factor. *Annu Rev Cell Biol* **6**: 217–46.
24. Verweij CL, Diergaarde PJ, Hart M, Pannekoek H (1986) Full-length von Willebrand factor (vWF) cDNA encodes a highly repetitive protein considerably larger than the mature vWF subunit. *EMBO J* **5**: 1839–1847.
25. Titani K, Kumar S, Takio K, Ericsson LH, Wade RD, Ashida K, Walsh KA, Chopek MW, Sadler JE, Fujikawa K (1986) Amino acid sequence of human von Willebrand factor. *Biochemistry* **25**: 3171–3184.
26. Wagner DD, Lawrence S, Ohlsson-Wilhelm B, Fay P, Marder V (1987) Topology and order of formation of interchain disulfide bonds in von Willebrand factor. *Blood* **69**: 27–32.
27. Wagner DD, Marder V (1984) Biosynthesis of von Willebrand protein by human endothelial cells: processing steps and their intracellular localization. *J Cell Biol* **99**: 2123–2130.
28. Wagner DD, Marder VJ (1983) Biosynthesis of von Willebrand protein by human endothelial cells. Identification of a large precursor polypeptide chain. *J Biol Chem* **258**: 2065–7.
29. Katsumi A, Tuley E, Bodo I, Sadler J (2000) Localization of Disulfide Bonds in the Cystine Knot Domain of Human von Willebrand Factor. *J Biol Chem* **275**: 25585–25594.

30. Wise RJ, Barr PJ, Wong PA, Kiefer MC, Brake AJ, Kaufman RJ (1990) Expression of a human proprotein processing enzyme: correct cleavage of the von Willebrand factor precursor at a paired basic amino acid site. *Proc Natl Acad Sci USA* **87**: 9378–82.

31. Vischer U, Wagner D (1994) von Willebrand factor proteolytic processing and multimerization precede the formation of Weibel-Palade bodies. *Blood* **83**: 3536–3544.

32. Dong Z, Thoma R, Crimmins D, Mccourt D, Tuley E, Sadler J (1994) Disulfide bonds required to assemble functional von Willebrand factor multimers. *J Biol Chem* **269**: 6753–8.

33. Purvis AR, Gross J, Dang LT, Huang R-H, Kapadia M, Townsend RR, Sadler JE (2007) Two Cys residues essential for von Willebrand factor multimer assembly in the Golgi. *Proc Natl Acad Sci USA* **104**: 15647–15652.

34. Voorberg J, Fontijn R, Mourik JAV, Pannekoek H (1990) Domains involved in multimer assembly of von willebrand factor (vWF): multimerization is independent of dimerization. *EMBO J* **9**: 797–803

35. Wagner DD, Fay PJ, Sporn LA, Sinha S, Lawrence SO, Marder VJ (1987) Divergent fates of von Willebrand factor and its propolypeptide (von Willebrand antigen II) after secretion from endothelial cells. *Proc Natl Acad Sci USA* **84**: 1955–9.

36. Verweij CL, Hart M, Pannekoek H (1987) Expression of variant von Willebrand factor (vWF) cDNA in heterologous cells: requirement of the pro-polypeptide in vWF multimer formation. *EMBO J* **6**: 2885–2890.

37. Mayadas TN, Wagner D (1989) In vitro multimerization of von Willebrand factor is triggered by low pH. Importance of the propolypeptide and free sulfhydryls. *J Biol Chem* **264**: 13497–13503.

38. Mayadas TN, Wagner DD (1992) Vicinal cysteines in the prosequence play a role in von Willebrand factor multimer assembly. *Proc Natl Acad Sci USA* **89**: 3531–5.

39. Purvis AR, Sadler J (2004) A Covalent Oxidoreductase Intermediate in Propeptide-dependent von Willebrand Factor Multimerization. *J Biol Chem 279*: 49982–8.

40. Huang R-H, Wang Y, Roth R, Yu X, Purvis AR, Heuser JE, Egelman EH, Sadler JE (2008) Assembly of Weibel-Palade body-like tubules from N-terminal domains of von Willebrand factor. *Proc Natl Acad Sci USA* **105**: 482–7.

41. Wise R (1988) The propeptide of von Willebrand Factor independently mediates the assembly of von Willebrand multimers. *Cell* **52**: 229–236.

42. Moake JL, Rudy CK, Troll JH, Weinstein MJ, Colannino NM, Azocar J, Seder RH, Hong SL, Deykin D (1982) Unusually large plasma factor VIII:von Willebrand factor multimers in chronic relapsing thrombotic thrombocytopenic purpura. *N Engl J Med* **307**: 1432–5.

43. Lui-Roberts WWY (2005) An AP-1/clathrin coat plays a novel and essential role in forming the Weibel-Palade bodies of endothelial cells. *J Cell Biol* **170**: 627–636.

44. Wagner DD, Olmsted JB, Marder VJ (1982) Immunolocalization of von Willebrand protein in Weibel-Palade bodies of human endothelial cells. *J Cell Biol* **95**: 355–360.

45. Sporn LA, Marder VJ, Wagner DD (1986) Inducible secretion of large, biologically potent von Willebrand factor multimers. *Cell* **46**: 185–190.

46. Sadler JE (2009) von Willebrand factor assembly and secretion. *J Thromb Haemost* **7** Suppl 1: 24–7.

47. Dong J-F, Moake JL, Nolasco L, Bernardo A, Arceneaux W, Shrimpton CN, Schade AJ, McIntire LV, Fujikawa K, López JA (2002) ADAMTS-13 rapidly cleaves newly secreted ultralarge von Willebrand factor multimers on the endothelial surface under flowing conditions. *Blood* **100**: 4033–9.

48. Zhou Y-F, Eng ET, Nishida N, Lu C, Walz T, Springer TA (2011) A pH-regulated dimeric bouquet in the structure of von Willebrand factor. *EMBO J* **30**: 4098-4111.

49. Mohri H, Fujimura Y, Shima M, Yoshioka A, Houghten RA, Ruggeri ZM, Zimmerman TS (1988) Structure of the von Willebrand factor domain interacting with glycoprotein Ib. *J Biol Chem* **263**: 17901–4.

50. Mohri H, Yoshioka A, Zimmerman TS, Ruggeri ZM (1989) Isolation of the von Willebrand factor domain interacting with platelet glycoprotein Ib, heparin, and collagen and characterization of its three distinct functional sites. *J Biol Chem* **264**: 17361–7.

51. Gralnick HR, Williams SP, Mckeown L, Kramer W, Krutzsch H, Gorecki M, Pinet A, Garfinkel LI (1992) A monomeric von Willebrand factor fragment, Leu-504--Lys-728, inhibits von Willebrand factor interaction with glycoprotein Ib-IX [corrected]. *Proc Natl Acad Sci USA* **89**: 7880–4.

52. Hoylaerts MF, Yamamoto H, Nuyts K, Vreys I, Deckmyn H, Vermylen J (1997) von Willebrand factor binds to native collagen VI primarily via its A1 domain. *Biochem J* **324**: 185–191.

53. Mazzucato M, Spessotto P, Masotti A, De Appollonia L, Cozzi MR, Yoshioka A, Perris R, Colombatti A, De Marco L (1999) Identification of domains responsible for von Willebrand factor type VI collagen interaction mediating platelet adhesion under high flow. *J Biol Chem* **274**: 3033–3041.

54. Tsai H (1996) Physiologic cleavage of von Willebrand factor by a plasma protease is dependent on its conformation and requires calcium ion. *Blood* **87**: 4235–4244.

55. Tsai H, Sussman I, Nagel R (1994) Shear stress enhances the proteolysis of von Willebrand factor in normal plasma. *Blood* **83**: 2171–9.

56. Furlan M, Robles R, Lamie B (1996) Partial purification and characterization of a protease from hu-

man plasma cleaving von Willebrand factor to fragments produced by in vivo proteolysis. *Blood* **87**: 4223–4234.

57. Lankhof H, van Hoeij M, Schiphorst ME, Bracke M, Wu YP, Ijsseldijk MJ, Vink T, de Groot PG, Sixma JJ. (1996) A3 domain is essential for interaction of von Willebrand factor with collagen type III. *Thromb Haemost* **75**: 950–8.

58. Wu YP, van Breugel HH, Lankhof H, Wise RJ, Handin RI, de Groot PG, Sixma JJ (1996) Platelet adhesion to multimeric and dimeric von Willebrand factor and to collagen type III preincubated with von Willebrand factor. *Arterioscler Thromb Vasc Biol* **16**: 611–620.

59. Zanardelli S, Chion ACK, Groot E, Lenting PJ, McKinnon TAJ, Laffan MA, Tseng M, Lane DA (2009) A novel binding site for ADAMTS13 constitutively exposed on the surface of globular VWF. *Blood* **114**: 2819–2828.

60. Moake JL, Turner NA, Stathopoulos NA, Nolasco LH, Hellums JD (1986) Involvement of large plasma von Willebrand factor (vWF) multimers and unusually large vWF forms derived from endothelial cells in shear stress-induced platelet aggregation. *J Clin Invest* **78**: 1456–1461.

61. Gralnick HR, Williams SB, Coller BS (1984) Fibrinogen competes with von Willebrand factor for binding to the glycoprotein IIb/IIIa complex when platelets are stimulated with thrombin. *Blood* **64**: 797–800.

62. Lawrence JB, Gralnick HR (1987) Monoclonal antibodies to the glycoprotein IIb-IIIa epitopes involved in adhesive protein binding: effects on platelet spreading and ultrastructure on human arterial subendothelium. *J Lab Clin Med* **109**: 495–503.

63. Goto S, Ikeda Y, Saldívar E, Ruggeri ZM (1998) Distinct mechanisms of platelet aggregation as a consequence of different shearing flow conditions. *J Clin Invest* **101**: 479–486.

64. Goto S, Salomon DR, Ikeda Y, Ruggeri ZM (1995) Characterization of the unique mechanism mediating the shear-dependent binding of soluble von Willebrand factor to platelets. *J Biol Chem* **270**: 23352-61.

65. Nieuwenhuis HK, Akkerman J, Houdijk W, Sixma J (1985) Human blood platelets showing no response to collagen fail to express surface glycoprotein Ia. *Nature* **318**: 470–2.

66. Savage B, Sixma JJ, Ruggeri ZM (2002) Functional self-association of von Willebrand factor during platelet adhesion under flow. *Proc Natl Acad Sci USA* **99**: 425–430.

67. Fowler WE, Fretto LJ, Hamilton KK, Erickson HP, McKee PA (1985) Substructure of human von Willebrand factor. *J Clin Invest* **76**: 1491–1500.

68. Slayter H, Loscalzo J, Bockenstedt P, Handin RI (1985) Native conformation of human von Willebrand protein. Analysis by electron microscopy and quasi-elastic light scattering. *J Biol Chem* **260**: 8559–8563.

69. Siediecki C, Lestini B, Kottke-Marchant K, Eppell S, Wilson D, Marchant R (1996) Shear-dependent changes in the three-dimensional structure of human von Willebrand factor. *Blood* **88**: 2939–2950.

70. Schneider SW, Nuschele S, Wixforth A, Gorzelanny C, Alexander-Katz A, Netz RR, Schneider MF (2007) Shear-induced unfolding triggers adhesion of von Willebrand factor fibers. *Proc Natl Acad Sci USA* **104**: 7899-7903.

71. Smith DE, Babcock HP, Chu S (1999) Single-polymer dynamics in steady shear flow. *Science* **283**: 1724–7.

72. Alexander-Katz A, Schneider MF, Schneider SW, Wixforth A, Netz RR (2006) Shear-flow-induced unfolding of polymeric globules. *Phys Rev Lett* **97**: 138101.

73. Alexander-Katz A, Netz RR (2008) Dynamics and instabilities of collapsed polymers in shear flow. *Macromolecules* **41**: 3363–3374.

74. De Gennes PG (1974) Coil-stretch transition of dilute flexible polymers under ultrahigh velocity gradients. *J Chem Phys* **60**: 5030–5042.

75. Springer TA (2009) Structural basis for selectin mechanochemistry. *Proc Natl Acad Sci USA* **106**: 91–6.

76. Oroz J, Valbuena A, Vera AM, Mendieta J, Gómez-Puertas P, Carrión-Vázquez M (2011) Nanomechanics of the cadherin ectodomain: "canalization" by Ca^{2+} binding results in a new mechanical element. *J Biol Chem* **286**: 9405–9418.

77. Le Trong I, Aprikian P, Kidd BA, Forero-Shelton M, Tchesnokova V, Rajagopal P, Rodriguez V, Interlandi G, Klevit R, Vogel V, Stenkamp RE, Sokurenko EV, Thomas WE (2010) Structural basis for mechanical force regulation of the adhesin FimH via finger trap-like beta sheet twisting. *Cell* **141**: 645–655.

78. Shi M, Zhu J, Wang R, Chen X, Mi L, Walz T, Springer TA (2011) Latent TGF-β structure and activation. *Nature* **474**: 343–9

79. Astrof NS, Salas A, Shimaoka M, Chen J, Springer TA (2006) Importance of force linkage in mechanochemistry of adhesion receptors. *Biochemistry 45*: 15020–8.

80. Randi A, Jorieux S, Tuley E, Mazurier C, Sadler J (1992) Recombinant von Willebrand factor Arg578-->Gln. A type IIB von Willebrand disease mutation affects binding to glycoprotein Ib but not to collagen or heparin. *J Biol Chem* **267**: 21187–21192.

81. Nakayama T, Matsushita T, Dong Z, Sadler JE, Jorieux S, Mazurier C, Meyer D, Kojima T, Saito H (2002) Identification of the regulatory elements of the human von Willebrand factor for binding to platelet GPIb. Importance of structural integrity of the regions flanked by the Cys1272-Cys1458 disulfide bond. *J Biol Chem* **277**: 22063–22072.

82. Emsley J, Cruz M, Handin R, Liddington R (1998) Crystal Structure of the von Willebrand Factor A1 Domain and Implications for the Binding of Platelet Glycoprotein Ib. *J Biol Chem* **273**: 10396–10401.

83. Celikel R, Varughese KI, Madhusudan, Yoshioka A, Ware J, Ruggeri ZM (1998) Crystal structure of the von Willebrand factor A1 domain in complex with the function blocking NMC-4 Fab. *Nat Struct Biol* **5**: 189–194.

84. Huizinga EG, Tsuji S, Romijn RA, Schiphorst ME, de Groot PG, Sixma JJ, Gros P (2002) Structures of glycoprotein Ibalpha and its complex with von Willebrand factor A1 domain. *Science* **297**: 1176–9.

85. Dumas JJ, Kumar R, McDonagh T, Sullivan F, Stahl ML, Somers WS, Mosyak L (2004) Crystal structure of the wild-type von Willebrand factor A1-glycoprotein Ibalpha complex reveals conformation differences with a complex bearing von Willebrand disease mutations. *J Biol Chem* **279**: 23327–23334.

86. Huizinga EG, Tsuji S, Romijn RA, Schiphorst ME, de Groot PG, Sixma JJ, Gros P (2002) Structures of glycoprotein Ibalpha and its complex with von Willebrand factor A1 domain. *Science* **297**: 1176–9.

87. Goodeve A (2010) The genetic basis of von Willebrand disease. *Blood Rev* **24**: 123–134.

88. Miller JL, Cunningham D, Lyle VA, Finch CN (1991) Mutation in the gene encoding the alpha chain of platelet glycoprotein Ib in platelet-type von Willebrand disease. *Proc Natl Acad Sci USA* **88**: 4761–5.

89. Miller JL (1996) Platelet-type von Willebrand disease. *Thromb Haemost* **75**: 865-869.

90. Arya M, Kolomeisky A, Romo G, Cruz M, Lopez J, Anvari B. Dynamic Force Spectroscopy of Glycoprotein Ib-IX and von Willebrand Factor (2005) Biophys J **88**: 4391–4401.

91. Yago T, Lou J, Wu T, Yang J, Miner JJ, Coburn L, López JA, Cruz MA, Dong J-F, McIntire LV, McEver RP, Zhu C (2008) Platelet glycoprotein Ibα forms catch bonds with human WT vWF but not with type 2B von Willebrand disease vWF. *J Clin Invest* **118**: 3195–3207.

92. Kim J, Zhang C-Z, Zhang X, Springer TA (2010) A mechanically stabilized receptor-ligand flex-bond important in the vasculature. *Nature* **466**: 992–5.

93. Lankhof H, Damas C, Schiphorst ME, Ijsseldijk MJ, Bracke M, Furlan M, Tsai HM, de Groot PG, Sixma JJ, Vink T (1997) von Willebrand factor without the A2 domain is resistant to proteolysis. *Thromb Haemost* **77**: 1008–13.

94. Fujikawa K, Suzuki H, McMullen B, Chung D (2001) Purification of human von Willebrand factor-cleaving protease and its identification as a new member of the metalloproteinase family. *Blood* **98**: 1662–6.

95. Gerritsen HE, Robles R, Lämmle B, Furlan M (2001) Partial amino acid sequence of purified von Willebrand factor-cleaving protease. *Blood* **98**: 1654–1661.

96. Sadler JE (2008) Von Willebrand factor, ADAMTS13, and thrombotic thrombocytopenic purpura. *Blood* **112**: 11–18.

97. Levy GG, Nichols WC, Lian EC, Foroud T, Mcclintick JN, Mcgee BM, Yang AY, Siemieniak DR, Stark KR, Gruppo R, Sarode R, Shurin SB, Chandrasekaran V, Stabler SP, Sabio H, Bouhassira EE, Upshaw JD, Ginsburg D, Tsai H-M (2001) Mutations in a member of the ADAMTS gene family cause thrombotic thrombocytopenic purpura. *Nature* **413**: 488–494.

98. Zhang Q, Zhou Y-F, Zhang C-Z, Zhang X, Lu C, Springer TA (2009;) Structural specializations of A2, a force-sensing domain in the ultralarge vascular protein von Willebrand factor. *Proc Natl Acad Sci USA* **106**: 9226-9231.

99. Jakobi AJ, Mashaghi A, Tans SJ, Huizinga EG (2011) Calcium modulates force sensing by the von Willebrand factor A2 domain. *Nature Communications* **2**: 385.

100. Zhang X, Halvorsen K, Zhang C-Z, Wong WP, Springer TA (2009) Mechanoenzymatic cleavage of the ultralarge vascular protein von Willebrand factor. *Science* **324**: 1330–4.

101. Ying J, Ling Y, Westfield LA, Sadler JE, Shao J-Y (2010) Unfolding the A2 domain of von Willebrand factor with the optical trap. *Biophys J* **98**: 1685–1693.

102. Nguyen TQ, Kausch HH (1988) Chain scission in transient extensional flow kinetics and molecular weight dependence. *J Non-Newton Fluid* **30**: 125–140.

103. Odell J, Keller A, Rabin Y (1988) Flow-induced scission of isolated macromolecules. *J Chem Phys* **88**: 4022.

104. Rabin Y (1988) On the mechanism of stretching and breaking of polymers in elongational flows. *J Non-Newton Fluid* **30**: 119-123.

105. Perkins TT, Smith DE, Chu S (1997) Single polymer dynamics in an elongational flow. *Science* **276**: 2016–2021.

106. Baldauf C, Schneppenheim R, Stacklies W, Obser T, Pieconka A, Schneppenheim S, Budde U, Zhou J, Gräter F (2009) Shear-induced unfolding activates von Willebrand factor A2 domain for proteolysis. *J Thromb Haemost* **7**: 2096–2105.

107. Kokame K, Matsumoto M, Fujimura Y, Miyata T (2004) VWF73, a region from D1596 to R1668 of von Willebrand factor, provides a minimal substrate for ADAMTS-13. *Blood* **103**: 607–612.

108. Soejima K, Matsumoto M, Kokame K, Yagi H, Ishizashi H, Maeda H, Nozaki C, Miyata T, Fujimura Y, Nakagaki T (2003) ADAMTS-13 cysteine-rich/spacer domains are functionally essential for von Willebrand factor cleavage. *Blood* **102**: 3232–7.

109. Klaus C, Plaimauer B, Studt J-D, Dorner F, Lämmle B, Mannucci PM, Scheiflinger F (2004) Epitope mapping of ADAMTS13 autoantibodies in acquired thrombotic thrombocytopenic purpura. *Blood* **103**: 4514–9.

110. Luken BM, Turenhout EAM, Hulstein JJJ, Van Mourik JA, Fijnheer R, Voorberg J (2005) The spacer domain of ADAMTS13 contains a major binding site for antibodies in patients with thrombotic thrombocytopenic purpura. *Thromb Haemost* **93**: 267–274.

111. Pos W, Crawley JTB, Fijnheer R, Voorberg J, Lane DA, Luken BM (2010) An autoantibody epitope comprising residues R660, Y661, and Y665 in the ADAMTS13 spacer domain identifies a binding site for the A2 domain of VWF. *Blood* **115**: 1640–9.

112. Gao W, Anderson P, Sadler J (2008) Extensive contacts between ADAMTS13 exosites and von Willebrand factor domain A2 contribute to substrate specificity. *Blood* **112**: 1713–7.

113. Gao W, Anderson PJ, Majerus EM, Tuley EA, Sadler JE (2006) Exosite interactions contribute to tension-induced cleavage of von Willebrand factor by the antithrombotic ADAMTS13 metalloprotease. *Proc Natl Acad Sci USA* **103**: 19099–19104.

114. Feys HB, Anderson PJ, Vanhoorelbeke K, Majerus EM, Sadler JE (2009) Multi-step binding of ADAMTS-13 to von Willebrand factor. *J Thromb Haemost* **7**: 2088–2095.

115. Zhang P, Pan W, Rux AH, Sachais BS, Zheng XL (2007) The cooperative activity between the carboxyl-terminal TSP1 repeats and the CUB domains of ADAMTS13 is crucial for recognition of von Willebrand factor under flow. *Blood* **110**: 1887–1894.

116. Wu J-J, Fujikawa K, McMullen BA, Chung DW (2006) Characterization of a core binding site for ADAMTS-13 in the A2 domain of von Willebrand factor. *Proc Natl Acad Sci USA* **103**: 18470–4.

117. Zanardelli S, Crawley JTB, Chion CKNCK, Lam JK, Preston RJS, Lane DA (2006) ADAMTS13 substrate recognition of von Willebrand factor A2 domain. *J Biol Chem* **281**: 1555–1563.

118. De Groot R, Bardhan A, Ramroop N, Lane D, Crawley J (2009) Essential role of the disintegrin-like domain in ADAMTS13 function. *Blood* **113**: 5609–5616.

119. Akiyama M, Takeda S, Kokame K, Takagi J, Miyata T (2009) Crystal structures of the noncatalytic domains of ADAMTS13 reveal multiple discontinuous exosites for von Willebrand factor. *Proc Natl Acad Sci USA* **106**: 19274–9.

120. Kokame K, Matsumoto M, Soejima K, Yagi H, Ishizashi H, Funato M, Tamai H, Konno M, Kamide K, Kawano Y, Miyata T, Fujimura Y (2002) Mutations and common polymorphisms in ADAMTS13 gene responsible for von Willebrand factor-cleaving protease activity. *Proc Natl Acad Sci USA* **99**: 11902–7.

121. Nishio K, Anderson PJ, Zheng XL, Sadler JE (2004) Binding of platelet glycoprotein Ibalpha to von Willebrand factor domain A1 stimulates the cleavage of the adjacent domain A2 by ADAMTS13. *Proc Natl Acad Sci USA* **101**: 10578–10583.

122. Dong JF, Moake J, Bernardo A, Fujikawa K, Ball C, Nolasco L, Lopez JA, Cruz M (2003) ADAMTS-13 Metalloprotease Interacts with the Endothelial Cell-derived Ultra-large von Willebrand Factor. *J Biol Chem* **278**: 29633-9.

CHAPTER 2

Calcium modulates force sensing by the von Willebrand Factor A2 domain

Arjen J. Jakobi, Alireza Mashaghi, Sander J. Tans and Eric G. Huizinga
Crystal & Structural Chemistry, Bijvoet Center for Biomolecular Research, Department of Chemistry, Utrecht University, Padualaan 8, 3584 CH Utrecht, The Netherlands
AMOLF Institute, Science Park 104, 1098 XG Amsterdam, The Netherlands.

Nature Communications **2**: 385 (2011)

Von Willebrand factor (VWF) multimers mediate primary adhesion and aggregation of platelets. VWF potency critically depends on multimer size, which is regulated by a feedback mechanism involving shear-induced unfolding of the VWF-A2 domain and cleavage by the metalloprotease ADAMTS-13. Here we report crystallographic and single-molecule optical tweezers data on VWF-A2 providing mechanistic insight into calcium-mediated stabilization of the native conformation that protects A2 from cleavage by ADAMTS-13. Unfolding of A2 requires higher forces when calcium is present and primarily proceeds through a mechanically stable intermediate with non-native calcium coordination. Calcium further accelerates refolding markedly, in particular under applied load. We propose that calcium improves force sensing by allowing reversible force-switching under physiologically relevant hydrodynamic conditions. Our data show for the first time the relevance of metal coordination for mechanical properties of a protein involved in mechanosensing.

In response to vascular lesions, platelets are stimulated to secure bleeding arrest by formation of a platelet plug. In the high shear environment found in the microvasculature or stenosed arteries, the adhesion of platelets critically depends on interactions with the plasma glycoprotein von Willebrand Factor (VWF). This factor recruits platelets to sites of vascular damage by interacting with collagen and the platelet receptor GPIbα [1,2].

VWF is synthesized and assembled into large, disulfide-bonded multimers in endothelial cells and platelet precursor megakaryocytes, and the multimer size of VWF determines its platelet-adhesive potency in a force-dependent manner. VWF circulates in the bloodstream as a series of multimers with a broad size distribution, while ultra-large VWF-multimers (ULVWF) are stockpiled in specialized storage organelles of endothelial cells and platelets [3] from which they are released in response to thrombogenic stimuli. The circulating pool of smaller VWF multimers depends on high shear forces to become activated for platelet

recruitment while ULVWF molecules, which may exceed 50,000 kDa in size [4], avidly bind to their platelet receptor GPIbα even at low shear stress. Upon secretion, ULVWF multimers remain initially attached to the cell-surface where they are then progressively cleaved at the Tyr1605-Met1606 scissile bond located within its A2 domains into smaller, less adhesive multimers by a specialized VWF cleaving protease ADAMTS-13 (a disintegrin and metalloproteinase with thrombospondin type 1 motif, member 13) [5,6].

This proteolytic regulation represents a critical 'inactivation' process that precludes the formation of spontaneous platelet-rich thrombi that may occlude the microvasculature. Accordingly, defective regulation of VWF multimer size is the cause of severe disorders. Depletion of high-molecular weight multimers due to mutations in the A2 domain that presumably increase susceptibility to proteolysis by ADAMTS-13 cause a bleeding tendency named type 2A von Willebrand disease [7-9]. In contrast, accumulation of ULVWF in circulation due to a congenital or acquired deficiency of ADAMTS-13 is the cause of thrombotic thrombocytopenic purpura (TTP), which is characterized by severe thrombosis in the microvasculature [8-10].

Regulation of VWF multimer size is unique in its dependence on hydrodynamic shear forces. Recent studies show that the Tyr1605-Met1606 scissile bond is buried inside the VWF A2 domain, which must be unfolded to become a substrate for ADAMTS-13 [11-13]. Consistent with binding of an unfolded conformation of A2, a crystal structure of the non-catalytic DTCS domains of ADAMTS-13 described an elongated, discontinuous linear array of three VWF-binding exosites [14]. Very recently, Zhou et al. [15] identified a calcium-binding site in the crystal structure of a disulfide-engineered A2 domain and demonstrated that calcium binding impedes proteolytic processing by ADAMTS-13 in static cleavage assays.

Here we report the crystal structure of the wild-type A2 domain with bound calcium and show that it markedly increases its thermodynamic and mechanical stability and provides the capability to refold despite tensile forces. The crystal structure of the A2–Ca^{2+} complex together with molecular dynamics simulations reveals a long-range stabilizing effect of calcium on the scissile strand. This finding raises the question whether calcium modulates the force sensing function of A2 and hence regulates sensitivity to ADAMTS-13. Using optical tweezers we probed, at the single-molecule level, how calcium affects the mechanical response of A2 under tensile forces. We find that calcium has a dual role in mechanosensing: by (1) increasing force resistance of A2 and (2) stabilizing an intermediate fold that promotes refolding under applied load. Our data indicate a direct role of metal ions in modulating the functions of a protein force sensor.

Results

Crystal structure of calcium-bound VWF-A2

We obtained well diffracting crystals of the wild-type VWF A2 domain in complex with calcium ion and determined its structure to 1.7 Å resolution (**Table 1**). The crystal asymmetric unit contains three A2 molecules that are essentially identical and comprise residues 1478–1674; we do not observe interpretable density for N-terminal residues

1478–1493, most likely due to flexibility. The overall arrangement of A2, like observed previously [12,15], largely follows the canonical α/β topology of VWA domains with a parallel central β sheet (β_1–β_6), flanked on one side by an antiparallel edge strand (β_3) and encircled by amphipathic α helices (α_1–α_6) that pack against the two faces of the hydrophobic sheet (**Fig. 1a,b**). A2 is set apart from all other structurally characterized members of the VWA fold by its lack of the α_4 helix, which is substituted by an elongated loop referred to as the α_4-less loo [12]. The α_4-less loop appears flexible: it adopts distinctly different conformations in the three independent A2 molecules in our structure and in the structure of calcium-free A2. Unlike the structurally homologous neighboring domains A1 and A3, and in accordance with its role in the reduction of VWF multimer size, A2 is devoid of an intramolecular disulfide bond between N- and C-terminal cysteine residues. Instead, C-terminal residues Cys1669 and Cys1670 form a buried vicinal disulfide bond at the C-terminus of helix α_6. The cleavage site for ADAMTS-13 between residues Tyr1605 and Met1606 is centrally positioned in β_4, deeply buried in the middle of the hydrophobic core

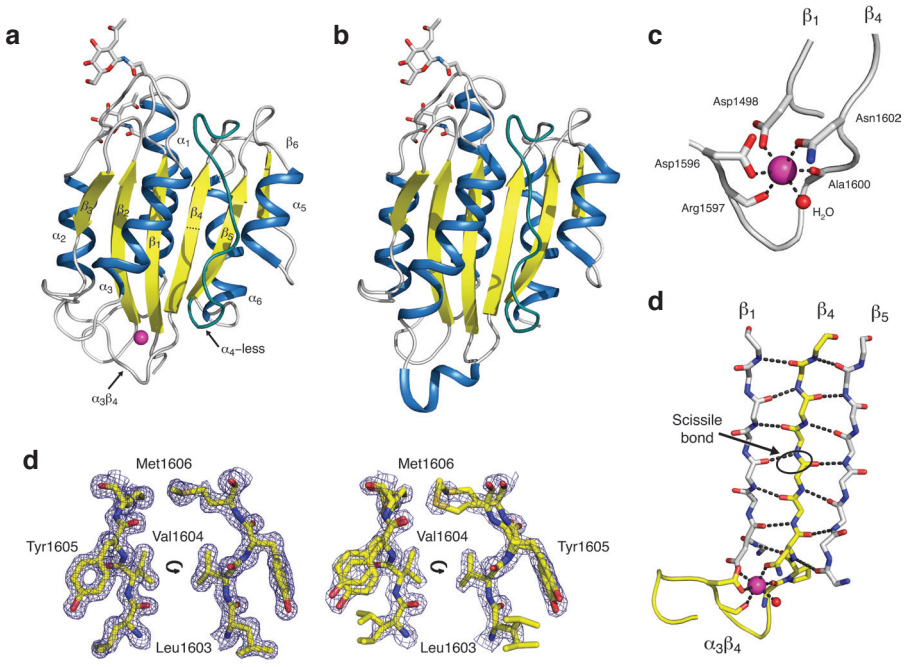

Figure 1 The calcium-binding site of A2 affects scissile strand dynamics and susceptibility to cleavage by ADAMTS-13. Crystal structures of calcium-bound wt-A2 (a) and, for comparison, calcium-free A2 (b; PDB 3GXB, [12]) are shown in cartoon representation. The central β sheet (yellow) is encircled by α helices (blue). Magenta, calcium ion; dark cyan, α_4-less loop; sticks, GlcNAG on residues Asn1515 and Asn1574. Both structures are similar, except for the clear rearrangement of the α3β4 loop (a 310 helix in calcium-free A2) that forms most of the calcium-binding site. (c) Close-up of the calcium-binding site of A2. The calcium ion is coordinated by the $\alpha_3\beta_4$ loop, Asp1498, and a water molecule (red sphere). Key side chains are shown in stick representation. (d) Close-ups of the scissile bond region in calcium-bound A2 (left) and calcium-free A2 (PDB 3GXB, ref. 12) (right) show, respectively, a single, well-defined conformation, and local disorder with multiple side and main chain conformations. Electron density is contoured at 0.6 e Å^{-3}. (e) Backbone representation of the β_4 scissile strand (yellow) and neighboring strands illustrating how calcium interlocks β_4 with β_1 via coordination by Asp1498 and Asn1602.

and inaccessible in the native conformation. The calcium ion predominantly interacts with the $\alpha_3\beta_4$ loop which, intriguingly, immediately precedes the scissile-bond bearing β_4 strand.

Calcium-binding affects scissile bond dynamics

The calcium ion is coordinated by four residues from the $\alpha_3\beta_4$ loop and a single residue, Asp1498, located in strand β_1 near the amino-terminus of the domain (**Fig. 1c**). The coordination motif of the class II calcium-binding site involves main chain carbonyl oxygen atoms of Arg1597 and Ala1600 and the side chain of Asn1602 as well as the monodentate carboxylate ligands of side chains of Asp1498 and Asp1596. A single water molecule completes the octahedral coordination sphere. The coordination stereochemistry is in very good agreement with reference values (**Supplementary Table S1**) [16-18] and together with the refined crystallographic parameters confirms calcium as the metal ion. As commonly observed for VWF-A domains [19,20], $\alpha_3\beta_4$ is additionally anchored by the side chain of the highly conserved Arg1597, which engages in ionic interactions with the carboxylate side chain, and hydrogen bonds to the main chain carbonyl, of Asp1498 (**Supplementary Fig. S1a-c**). Binding sites for divalent metal ions have been described for other proteins containing VWA domains. In I-domains of the integrin family of cell adhesion receptors, metal coordination by a metal ion-dependent adhesion site (MIDAS), located at the 'top' of the domain, plays an important role in ligand binding [21-23]. In contrast, the calcium-binding site of the A2 domain, which is strictly conserved in mammals (**Supplementary Fig. S1d**), is located at the 'bottom' of a VWA domain, and, in the absence of known VWF-A2 ligands, appears to have a functional role different from ligand binding.

While leaving the overall structure unchanged, calcium binding leads to a substantial rearrangement of the $\alpha_3\beta_4$ loop (**Supplementary Fig. S1e**). The calcium ion is located as far as 16 Å away from the peptide bond cleaved by ADAMTS-13, but nevertheless clear differences exist between the calcium-bound and calcium-free structures with respect to the dynamics of residues near the scissile bond. In the calcium-free structure, alternate backbone geometries and multiple side chain conformations exist for several residues within scissile strand β_4. In contrast, for calcium-bound A2 we observe a well-defined main chain trace and, with exception of Leu1603, single side chain conformations throughout the scissile strand (**Fig. 1d**). These apparent local differences in conformational flexibility cannot be attributed to differences in core packing (**Supplementary Fig. S2**). Molecular dynamics simulations show that the absence of calcium induces flexibility in the calcium-binding $\alpha_3\beta_4$ loop and that this mobility propagates to the two central strands β_1 and β_4 including the scissile bond (**Supplementary Fig. S3**). It appears therefore that extension of the hydrogen bond network between β_1 and β_4 with a pair of strong ionic and ion-dipole interactions, provided by the calcium-coordinating residues Asp1498 and Asn1602 (**Fig. 1e**), rigidifies the scissile bond region.

Electrostatic repulsion modulates stability of the native A2 domain

We used a thermal denaturation assay to assess the effect of calcium on the stability of the VWF-A2 domain by monitoring protein unfolding with an environment sensitive fluorescent

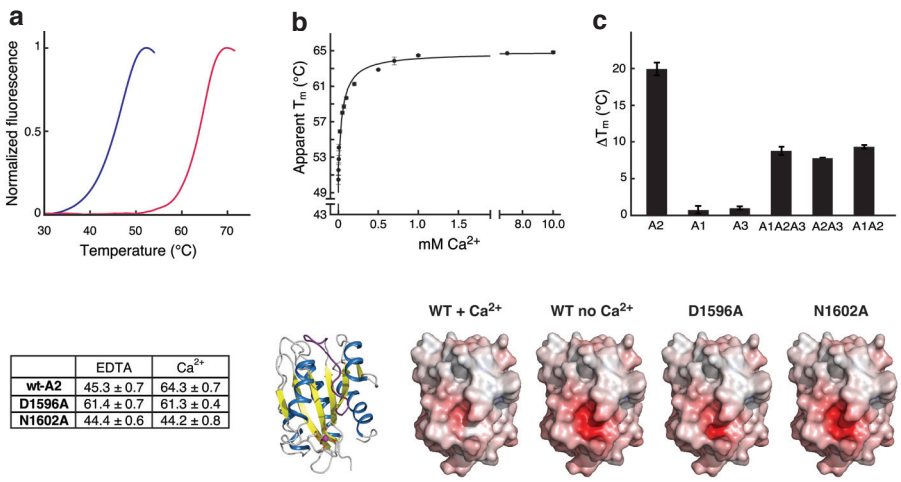

	EDTA	Ca^{2+}
wt-A2	45.3 ± 0.7	64.3 ± 0.7
D1596A	61.4 ± 0.7	61.3 ± 0.4
N1602A	44.4 ± 0.6	44.2 ± 0.8

Figure 2 Calcium stabilizes the native conformation of A2. (a) Thermofluor stability assays were performed with monomeric A2 in buffer without (blue) or with (red) 1 mM $CaCl_2$. Curves were normalized to maximum fluorescence signal. Data show representative curves of triplicate experiments. (b) Calcium binds A2 with high affinity and stabilizes A2 in a concentration-dependent manner. Apparent melting temperatures were extracted from the midpoint of the unfolding transition. (c) Comparison of the difference in apparent melting temperature for individual VWF A-domains and native tandem constructs determined in the presence and absence of 1 mM $CaCl_2$. A consistent shift of the unfolding temperature is only observed if A2 is part of the construct. Bar graphs represent mean Tm differences with respect to conditions containing EDTA (n=3). Error bars represent s.d. (d) Summary of unfolding temperatures (± s.d.) in the presence and absence of calcium. (e) Comparison of surface electrostatic potentials of wt-A2 and the D1596A and N1602A mutants. As reference, a ribbon model is shown in the same orientation. Electrostatic potentials were calculated on the solvent-accessible surface and contoured at -15 (red) to +15 (blue) kTe^{-1} (where k is the Boltzmann constant, T is temperature and e is elementary charge). The strongly negatively charged surface pocket forms the calcium-binding site. Thermal stability correlates with neutralization of electrostatic repulsion in the calcium-binding pocket.

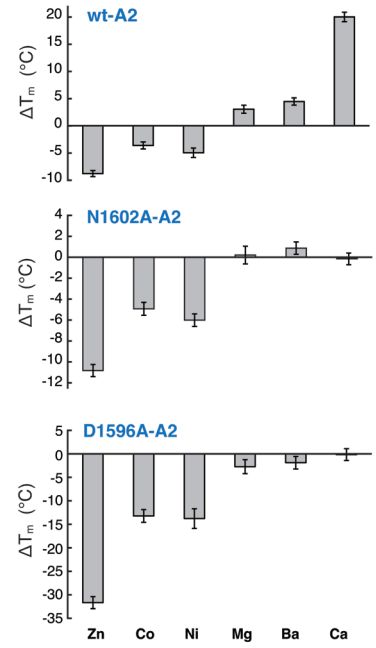

Figure 3 Thermal stabilization of A2 is specific for calcium. (a) Thermofluor stability assays were performed with monomeric wt-A2 or the calcium-binding deficient mutants N1602A and D1596A in buffer with 1 mM $CaCl_2$, 20 mM $BaCl_2$, 10 mM $MgCl_2$, 10 mM $CoCl_2$, 10 mM $NiCl_2$, or 10 mM $ZnCl_2$. Bar graphs represent mean Tm differences with respect to conditions containing EDTA (n=3). The qualitative similarity of the data obtained for wt-A2 and both mutants with respect to the effect of Co^{2+}, Ni^{2+} and Zn^{2+} indicates that the destabilizing effect observed for these metal ions does not result from competition with the calcium site. Error bars represent s.d.

dye [24,25] in the presence and absence of calcium. A marked increase in thermal stability was observed after addition of calcium ions, which shifted the T_m of A2 in a concentration-dependent manner from 45 °C to 64 °C (**Fig. 2a**). Analysis of the concentration-dependent T_m shift [26] observed upon titration with calcium (**Fig. 2b**) suggests that VWF-A2 binds calcium with an apparent K_D of 0.2 ± 0.04 (s.e.m.) μM. Comparison with unfolding curves obtained for a series of different divalent cations demonstrates that the observed stabilizing effect is specific for calcium (**Fig. 3**). Importantly, a consistent shift in T_m upon addition of calcium is also observed for constructs of A2 that contain its flanking domains A1 and/or A3, whereas no significant shift in T_m is observed for the isolated A1 or A3 domain (**Fig. 2c**). These data show that VWF-A2, both in isolation and in the relevant domain-context of full-length VWF, is stabilized by a metal ion binding-site that displays high affinity and specificity for calcium.

Thermal stability assays with alanine-mutants of calcium-coordinating residues Asp1596 and Asn1602 (the D1498A mutant could not be expressed, likely because its above-mentioned interaction with Arg1597 is essential for domain stability) gave intriguing results. Despite its inability to bind calcium the D1596A mutant shows thermal stability comparable to wt-A2 in the presence of saturating calcium concentrations**.** In contrast, N1602A unfolds at a temperature similar to wt-A2 in the absence of calcium (**Fig. 2d)**. Apparently, loss of thermal stability due the absence of a positively charged calcium ion can be compensated by the removal of the negatively charged side chain of Asp1596. These results suggest that neutralization of electrostatic repulsion by binding of calcium to the highly negatively charged calcium-binding pocket (**Fig. 2e**) is a prominent factor of domain stability.

ADAMTS-13 sensitivity parallels thermal stability

Cleavage of A2 by ADAMTS-13 requires partial unfolding of A2 to uncover the buried cleavage site [13]. The cleavage rate of any proteolysis reaction will involve a balance between the accessibility of the cleavage site, i.e. substrate availability, and the efficiency of the cleavage reaction. To discern these effects we performed cleavage experiments with both a folded A2 domain and with a calcium-binding deficient, unstructured substrate polypeptide comprising C-terminal residues Asp1596 – Arg1668 of A2 [15] fused to human growth hormone (hGH-VWF73). Since ADAMTS-13 requires divalent metal ions for activity we performed experiments either in the presence of 5 mM calcium or 5 mM barium, which similarly activates ADAMTS-13 [5,6], but only marginally stabilizes A2 (**Fig. 3**).

Proteolysis of the folded wild-type A2 domain or the calcium-binding deficient mutants D1596A and N1602A reveals a clear correlation between thermal stability and ADAMTS-13 sensitivity (**Fig. 4a**). In the presence of calcium only low cleavage levels of wild-type A2 were observed, while cleavage occurred readily when calcium was substituted by barium (**Fig. 4b**). Consistent with the thermal stability data, cleavage levels for the thermostable D1596A mutant were similar to calcium-stabilized wt-A2 no matter whether cleavage conditions contained calcium or barium, thus confirming that stability of this mutant is independent of metal coordination. The thermolabile mutant N1602A was cleaved

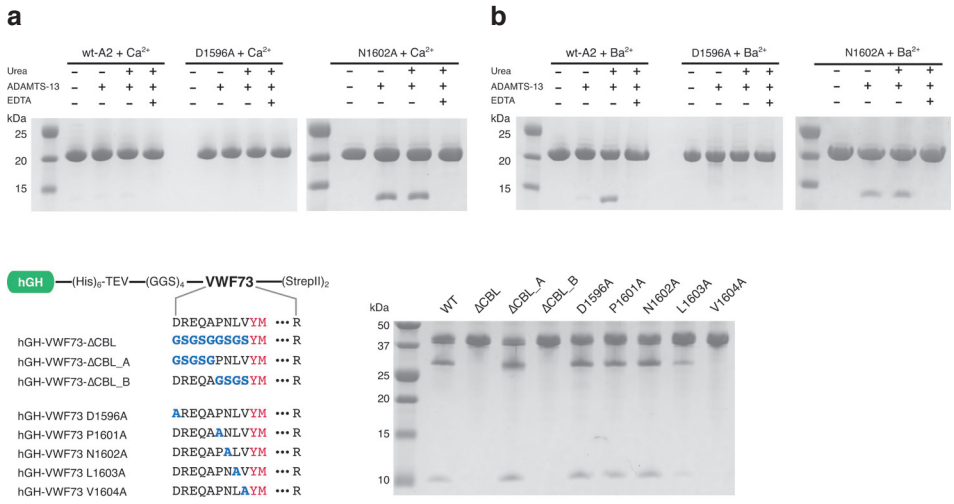

Figure 4 VWF-A2 proteolysis by ADAMTS-13. (a) Recombinant wt-A2 or the calcium-binding deficient mutants D1596A and N1602A were incubated with 6 nM ADAMTS-13 and 5 mM CaCl2, with and without 1.5 M urea. No cleavage is observed under these conditions for wt-A2 and D1596A, whereas the destabilized N1602A mutant is cleaved efficiently. (b) ADAMTS-13 cleaves wt-A2 and N1602A, but not D1596A if BaCl2 replaces CaCl2. Due to divalent ion dependence of ADAMTS-13 no cleavage occurs in the presence of EDTA. (c) hGH-VWF73 fusion constructs. A (Gly-Gly-Ser)4 linker was engineered between hGH and VWF73 to ensure that substrate cleavage is not influenced by vicinity of the hGH fusion. Substituted fragments of the α3β4 loop are highlighted in blue; the Tyr1605-Met1606 cleavage site is shown in magenta. (d) ADAMTS-13 cleavage of hGH-VWF73 constructs. VWF73 proteins with D1596A, P1601A and N1602A mutations are cleaved at similar rates as the wild-type sequence. Substrate specificity resides in the P3 and P2 residues Leu1603 and Val1604. Arrows indicate N- (upper arrow) and C-terminal (lower arrow) cleavage products.

efficiently and at a similar rate as wt-A2 in the absence of calcium **(Fig. 4a,b**). These data demonstrate that calcium binding by native A2 decelerates cleavage under static conditions and supports a functional role of calcium in stabilizing the scissile bond in its native, concealed conformation.

Proteolysis of the unstructured hGH-VWF73 construct showed that the wild-type sequence and the D1596A and N1602A mutants are cleaved at similar rates (**Fig. 4d**). This indicates that the calcium-binding side chains of Asp1596 and Asn1602 do not directly contribute to substrate recognition. Our observation that the N1602A mutant is cleaved efficiently by ADAMTS-13 contrasts data by Zhou et al. [15] who, using a similar construct, observed no cleavage for this mutant. While we cannot currently explain this discrepancy, it has been shown previously that deletion of $\alpha_3\beta_4$ residues Asp1596–Val1604 from an unstructured C-terminal A2 fragment prevents proteolysis of this fragment by ADAMTS-13 [11,27], which suggests that this stretch of residues does contain elements that are essential for recognition by ADAMTS-13. To clarify this point we systematically mutated the sequence that constitutes the $\alpha_3\beta_4$ loop and β_4 strand up to the scissile bond within the context of the hGH-VWF73 construct (**Fig. 4c**). Our data demonstrate that the residues critical for substrate recognition reside within the Pro1601–Val1604 sequence, since substitution of this sequence by GlySerGlySer abrogates cleavage completely, while substitution of residues D1596-A1600 by GlySerGlySerGly has no effect (**Fig. 4d**). Using

individual alanine mutants of the P1601-V1604 sequence, we find that the L1603A and V1604A mutations significantly affect the extent of cleavage, indicating that the P3 and particularly, the P2 sites are important recognition elements for ADAMTS-13. On the basis of our data we find no evidence for participation of Asn1602 at the P4 site in recognition by ADAMTS-13. Instead our data suggest that its effect on the proteolysis rate is a consequence of reduced thermal stability due to loss of calcium binding.

Calcium stabilizes a mechanical unfolding intermediate and promotes refolding against tensile force

The previous results show that calcium plays an important role in protecting VWF from ADAMTS-13 cleavage under static, low shear stress conditions. These findings raise the question whether calcium might also play a role in high shear stress situations where the A2 domain can unfold. To address this issue, we used optical tweezers to apply tensile forces on single A2 molecules and followed their unfolding and refolding transitions in the presence or the absence of calcium. N-glycosylated A2 molecules containing an amino-terminal $(cmyc)_4$-tag and a carboxy-terminal biotin tag were immobilized on anti-myc coated polystyrene beads and tethered to a second polystyrene bead via a ~ 2500 bp DNA spacer by biotin-streptavidin interactions (**Fig. 5**). We stretched and relaxed individual A2 molecules by displacing the bead on the pipette relative to the force-transducing bead in the optical trap and measured the resultant force versus extension curves at constant trap velocity.

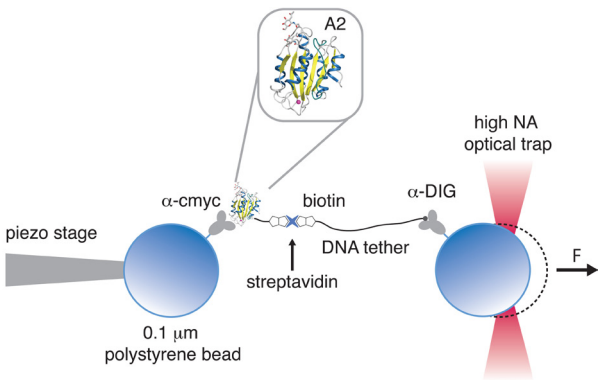

Figure 5 Schematic illustration of the optical tweezers experiment. Single A2 domains (enlarged inset) are tethered between polystyrene beads that are held by a piezo-controlled micropipette and the optical trap. The tether includes a 2500 bp DNA spacer to prevent unspecific bead-bead interactions.

First we stretched individual tethers in the presence of EDTA to characterize the mechanical behavior of A2 in the absence of calcium. At forces between 5 and 15 pN we observe abrupt changes in extension, associated with a drop in force on the tether, which indicate unfolding transitions (**Fig 6a,b**). To relate the observed extension changes to the sequence of the protein molecule we used a serial worm-like-chain (WLC) model [28] to fit our force-extension data. We obtain a total length increment (78 ± 4 nm) that is in good agreement with the total length of A2 (196 residues) assuming a contour length contribution of 0.4 nm per residue [29]. The data suggests disruption of individual A2 molecules in a single unfolding transition, consistent with recent experiments performed

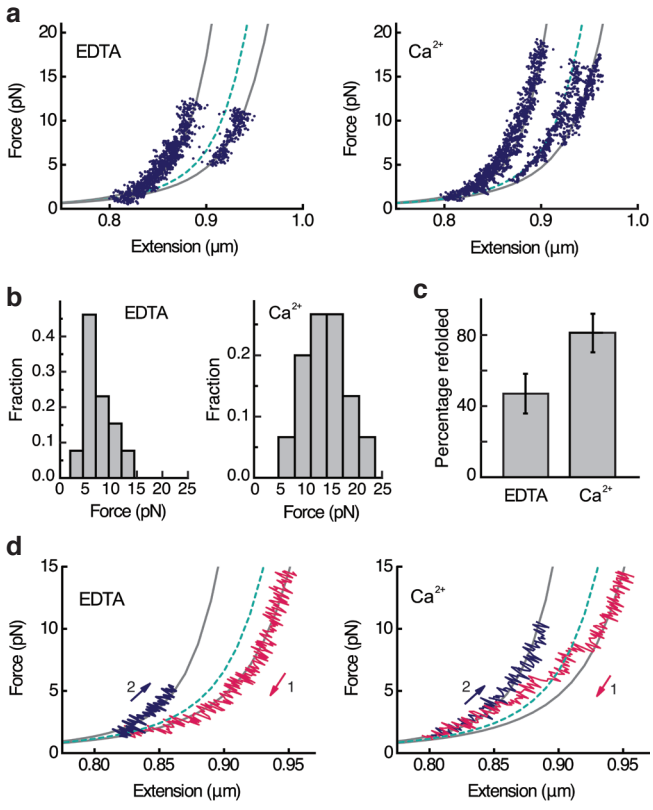

Figure 6 Calcium modulates the folding and unfolding pathways of A2 under tensile force. (a) Representative force-extension data showing six unfolding experiments, without (left) and with (right) calcium. Gray lines represent worm-like chain (WLC) fits to the native and unfolded states. The green dashed line is the WLC fit to a subset of the data that populates an intermediate state. (b) Force distribution histograms for unfolding events with and without calcium obtained at a loading rate of 5 pN s^{-1}. Mean unfolding forces are 7 ± 3 pN (n=13) and 14 ± 4 pN (n=15), respectively. (c) Probability to refold to the native state at zero load significantly increases in the presence of calcium (P<0.03). T-bars represent s.d. from counting statistics. (d) Relaxation traces (magenta) of A2 molecules without (left) or with (right) calcium show A2 is able to refold against load only when calcium is present. The dashed line is the WLC fit to the intermediate observed during unfolding. Stretching traces observed after successful refolding are shown in blue.

with a similar construct [13,30].

Next, we repeated the experiments in the presence of calcium. Two marked differences were observed. First, the average force required for complete unfolding of A2 increased to 14 ± 4 pN, a substantial (7 ± 3 pN) and significant (P<0.0001) increase of the resistance of the native state against tensile forces compared to the situation without calcium (**Fig. 6b**). Second, in 59% of the observed transitions (n=17), unfolding in the presence of calcium proceeded in a two-step manner via a well discernible intermediate that is stable against applied loads of up to 16 pN **(Fig. 6a)**. The intermediate is consistent with a contour length that corresponds to 122 ± 5 residues. In contrast, this intermediate is populated in only 21% of the unfolding events (n=13) if calcium-binding of A2 is suppressed by EDTA (**Supplementary Fig. S4a**); in all other events unfolding under these conditions proceeded via a single transition.

We investigated whether calcium also affects the folding pathway of A2. After each unfolding cycle we relaxed the tether and waited for 5 seconds at zero force to allow the A2 domain to refold. Subsequently the protein was stretched again to assess whether it had refolded, as identified by an unfolding force and length that are typical for the native state (**Supplementary Fig. S4b**). Again two pronounced differences were observed. With EDTA, native refolding was observed in 47% of the experiments (n=17) while with calcium, refolding occurred in 81% of the experiments (n=16, P=0.03) (**Fig. 6c**). Assuming first

order kinetics we roughly estimate that calcium increases the folding rate constant 6–7 fold, which is a striking acceleration of the refolding process. Secondly, we found that 37% of the relaxation traces with calcium displayed clear deviations from the WLC model that indicate contraction of the polypeptide chain. Closer inspection suggests that at ~ 5 pN, 71% of these traces transiently follow the same WLC curve that corresponds to the intermediate visited during unfolding, before displaying the native contour length at lower forces (**Fig. 6d**). Although the structural changes underlying the observed compaction under load remain unclear, our data suggest folding of A2 proceeds via one or more intermediates that are induced by interactions with calcium.

The increased probability to unfold via the intermediate in the presence of calcium suggests that calcium stabilizes the intermediate state. Intriguingly, the structure of the intermediate observed during unfolding does not seem to be a purely native sub-structure. The minimal sub-structure within the native state that contains all the native calcium interactions comprises 104 residues (see **Fig. 1c**), which is significantly more than the 74 ± 6 residues that we find experimentally when unfolding the intermediate. If refolding would occur through the same intermediate this would suggest the formation of non-native contacts that are subsequently broken when folding to the native state. Overall, the single-molecule data indicate that calcium at physiological concentrations has a pronounced effect on the folding and unfolding pathway of A2 and support a dual functional role of calcium in both stabilizing A2 against mechanical unfolding and promoting refolding by acting as a folding cofactor that facilitates refolding against tensile load.

Discussion

In the circulation, where hydrodynamic forces are ubiquitous, a unique regulatory mechanism has evolved to achieve efficient adhesion to vascular lesions while avoiding excessive aggregation of platelets [31]. At the molecular level this process involves the multimeric VWF molecule, which forms an avid binding platform for platelets. VWF responds to force on different levels. First, hydrodynamic shear forces induce a conformational change in VWF multimers [32,33], thus revealing a hidden binding site and activating VWF for binding of platelets [34]. Second, the adhesive potential of VWF – which is determined by the size of its multimers – is negatively regulated by a feedback mechanism, in which critical shear forces lead to unfolding of the A2 domain, exposing a proteolytic cleavage site for ADAMTS-13. In this sense the A2 domain of VWF is a mechanosensor that detects changes in hydrodynamic shear force to control platelet recruitment to lesions.

Here we show that calcium-binding to VWF-A2 critically affects its mechanosensing function, using a combination of structural, biochemical and single-molecule experiments. We find that the calcium-binding site visualized in our crystal structure stabilizes the native conformation of both the isolated A2 domain and of A2 in its natural context. A2 binds calcium with micromolar affinity, implying that the metal-binding site in circulating VWF is saturated with calcium. Both the crystal structure and molecular dynamics simulations reveal that calcium-binding restrains structural flexibility of the scissile strand environment. Using a single-molecule approach, we find that calcium coordination markedly increases

the resistance of A2 against mechanical unfolding while at the same time accelerating native refolding and promoting folding in the presence of tensile forces by stabilizing an intermediate fold. These findings provide fundamental new insights in shear force sensing by VWF and its cleavage by ADAMTS-13.

Calcium coordination, by stabilizing VWF-A2 in its native conformation, protects VWF-A2 from premature cleavage by ADAMTS-13 at low hydrodynamic forces, which is essential to preserve VWF multimers of sufficient size to elicit strong platelet interaction. The role of calcium in ADAMTS-13 proteolysis of VWF is janus-faced: it protects VWF, but at the same time activates ADAMTS-13 [6,35-37]. This concept explains previous observations on the effect of calcium and barium: barium can replace calcium as a co-factor of ADAMTS-13 activity [5], but only marginally stabilizes A2 (see **Fig. 3**). Activation by barium far outweighs its stabilizing effect on A2 in static cleavage assays ADAMTS-13 (see **Fig. 4b**). Our data therefore resolve a persisting controversy concerning the dependence of ADAMTS-13 on calcium and barium for optimal activity in cleavage assays.

Our single molecule data indicate a central role of unfolding and refolding dynamics in VWF-A2 force sensing. A force sensor requires elastic elements that not only turn a signal 'on' once a certain threshold force is crossed, but also turn it off again when the force drops below a critical value. Without calcium, A2 provides the first capability by unfolding beyond the unfolding force and exposing the cleavage site, but is poor at the second as it requires zero force for efficient refolding. Our study shows that calcium coordination fills this gap by promoting refolding despite an applied load, while at the same time increasing stability against forced unfolding. Such reversibility of switching enables a more dynamic and precise regulation by VWF-A2: once cleavage attenuates the shear force below a critical value, the remaining A2 domains can refold to maintain a balanced level of platelet recruitment.

The data put a new perspective on the role of metal coordination in general. While metal coordination is pervasive in proteins and its effect on equilibrium stability has been well studied, its potential role in shaping protein folding pathways remains largely unexplored. Our results offer a first example of metal coordination that alters the folding and unfolding pathway of a protein under mechanical load. This pathway-level information may also help to explain the observed increases in refolding propensity, as our data suggest refolding occurs via a calcium-induced intermediate state. Intermediate states can lower energy barriers and thus increase folding propesities, as has for instance been shown for filamin ddL4 in single-molecule studies [38,39]. It has recently been shown theoretically that length and force jumps observed with optical traps do not necessarily indicate the existence of a folding barrier in the absence of force, such as observed in bulk folding experiments [40]. While folding at zero force is the pertinent physical condition for most proteins, A2 in contrast, is constantly subject to transient shear forces in its physiological environment and accordingly transitions across barriers of energy surfaces under load are of direct physiological relevance. Our data demonstrates that calcium modulates the collapse trajectory and enables A2 to refold against applied tensile forces.

It would be of interest to know the precise structural changes underlying the transitions

to and from the calcium-stabilized intermediate state observed during unfolding of A2, and to determine whether they can be cleaved by ADAMTS-13. The data provide intriguing hints. First, the observed calcium-induced unfolding intermediate is different from a VWF-A2 intermediate observed previously in the absence of calcium [13], as well as from an intermediate suggested by molecular dynamics simulations in the presence of calcium [15] (and simulations performed by us; data not shown), which suggests that more than one intermediate structure might play a role. Second, while the observed refolding intermediate is calcium dependent, it does not contain the calcium coordination as found in the native structure, which indicates non-native contacts are formed and broken during folding.

Our data demonstrate, for the first time, that calcium coordination critically affects force sensing in VWF, and suggests that folding and unfolding equilibrium under tensile force to be a regulatory mechanism of VWF multimer size by ADAMTS-13 cleavage. Furthermore, it is intriguing to consider whether metal coordination also affects function and folding dynamics of other mechanosensitive proteins.

Methods

Protein expression and purification. VWF residues 1478–1674 (A2), 1261–1674 (A1A2), 1478–1874 (A2A3), and 1261–1874 (A1A2A3) were expressed in HEK293-EBNA1-S cells. Culture supernatants were harvested 5 days post transfection and concentrated using a Quixstand hollow fiber system (GE Healthcare) prior to diafiltration into 25 mM HEPES pH 7.8, 0.5 M NaCl. A1 (residues 1261–1468) was expressed in *P. pastoris* as described previously [41]. Recombinant proteins were purified by Ni-NTA affinity chromatography followed by proteolytic cleavage of the hexahistidine tag and further purified by ion exchange chromatography with MonoQ (GE Healthcare) in 20 mM HEPES pH 7.8 with a 0–0.25 M NaCl gradient (A2, A1A2, A2A3, A1A2A3) or MonoS (GE Healthcare) in 20 mM MES pH 5.5 with a 0.2–0.3 M NaCl gradient (A1). N-glycans were trimmed by incubating proteins (~ 1 mg ml^{-1}) with $EndoH_f$ (NEB) in 0.1 M NaAc (pH 5.5), 100 mM NaCl for 2 h at 37 °C. $EndoH_f$ was removed by affinity chromatography on amylose sepharose (NEB) in PBS. Proteins were finally purified by size exclusion chromatography in 15 mM HEPES (pH 7.5), 20 mM NaCl (100 mM for A1) and 1mM $CaCl_2$ (A2, A2A3, A1A2 and A1A2A3). We noted that both mutant A2 constructs and wt-A2 in buffer without calcium are prone to aggregation during freeze-thawing or prolonged storage at 4°C. The presence of aggregates affected thermal stability and ADAMTS-13 cleavage assays and we therefore exclusively used material for which monodispersity was confirmed by analytical gel filtration immediately prior to the experiments.
To study substrate specificity of ADAMTS-13, VWF73 constructs (residues 1596-1668) [27] with a C-terminal $(StrepII)_2$ tag were inserted into an expression vector encoding human growth hormone containing a His-tag and TEV cleavage site and including an additional $(GGS)_4$ spacer between the TEV site and the VWF73 fragment. hGH-VWF73 fusion proteins were expressed in HEK293-EBNA1-S cells. Proteins were purified by Ni-NTA/StrepTactin tandem affinity chromatography, followed by size exclusion chromatography in 15 mM HEPES (pH 7.5), 20 mM NaCl.

Crystallization, data collection and refinement. Crystals of A2 carrying a V1565L polymorphism (see **Supplementary Fig**. **S5**) were grown using hanging drop vapor diffusion at 292 K by mixing equal volumes of 9 mg ml^{-1} protein and reservoir solution. Within 24 h crystals appeared as stacked needles in 0.1 M MMT (pH 4.3–4.7), 0.2 M $(NH_4)_2SO_4$, 18–20 % (w/v) PEG2000 MME. Tiny needles (10 × 3 × 3 μm) were obtained by streak seeding with a cat whisker into 0.1 MMT (pH 4.0–5.5), 0.15 M $(NH_4)_2SO_4$, 18–23 % (w/v) PEG2000 MME. For cryoprotection, crystals were soaked in the crystallization condition supplemented with 20% (v/v) glycerol. Diffraction data were collected on the ESRF ID23-2 microfocus beamline and processed with XDS [42] and SCALA [43]. The crystal structure was solved using molecular replacement in PHASER [44]. Models were obtained from the

human VWF-A3 domain (PDB 1ATZ, [20]) with all side chains truncated to C_β atoms and VWF-A2 (PDB 3GXB, [12]). The structure was built in part using Arp/Warp [45] and completed manually in COOT [46]. The initial models were refined using PHENIX [47] and manual model building in COOT. Positional non-crystallographic symmetry constraints were imposed only during the initial steps of refinement. Calcium-ligand distances were initially restrained according to Harding[16,18] and refined unrestrained in the final steps of refinement. **Table 1** summarizes data collection and refinement statistics. The crystal structure was validated with MolProbity [48] and showed 96.4 % of all residues in Ramachandran-favored and 99.3% in Ramachandran-allowed regions. There is one outlier, Ser1543, in all three copies of the asymmetric unit for which the density convincingly supports the modeled conformation.

MD simulations. All simulations and analysis were carried out using GROMACS version 3.3.3 [49]. The OPLS-AA all atom force field [50] and the TIP4P [51] water model were used. Proteins were solvated in cubic boxes with a minimum distance of 10 Å between solute and box edge. Sodium and chloride ions were added to an ionic strength of 150 mM and the appropriate number of additional ions was added to neutralize the system. The system was minimized by steepest descent minimization and a subsequent 250 ps MD simulation with harmonic restraints on the protein main-chain atoms was carried out to equilibrate the solvent and ions. The final structure of this run served as starting structure for the subsequent MD simulations. Constant pressure periodic boundary water box MD simulations were performed using particle-mesh Ewald summatiom [52] for long-range electrostatics. The systems were equilibrated for 5 ns before production runs. Temperature was kept constant at 300 K by coupling to the Nosé-Hoover thermostat and a Parrinello-Rahman barostat was applied for pressure coupling. During the equilibration, the positional restraints on main-chain atoms were reduced stepwise. No restraints were applied in the production phase and the equilibration part of the MD trajectories was not used for data analysis. During the final production runs an integration step of 2.0 fs was used by applying the LINCS algorithm [53] to constrain bonds. The cutoff for vdW interactions was set to 10 Å during all simulations.

Thermal denaturation assays. Protein was dialyzed into 50 mM HEPES (pH 7.5), 20 mM NaCl, 10 mM EDTA to remove divalent metal ions. Next, EDTA was removed by three successive dialysis steps into a 10000-fold excess of 50 mM HEPES (pH 7.5), 20 mM NaCl in Chelex100-filtered H_2O (BioRad). All additives were dissolved in 50 mM HEPES (pH 7.5). 12.5 μl of a solution containing 500 ng protein was diluted in H_2O with 5x Sypro Orange (Sigma Aldrich) and immediately mixed with an equal volume of assay condition. All conditions were assessed in triplicate. Fluorescence increase was monitored on a MyiQ real-time PCR instrument (BioRad). Assays were performed over a temperature range of 15–90 °C using a ramp rate of 1 °C min^{-1} in steps of 0.5 °C. Fluorescence data from triplicate measurements were baseline-corrected individually and unfolding curves were normalized to maximum fluorescence to yield fractional denaturation curves. The apparent T_m was determined as the inflection point of a sigmoidal fit to the normalized fluorescence signal. The apparent K_D was calculated from the concentration-dependent T_m shift at varying calcium concentrations [26]. All calcium concentrations used for the K_D calculations were corrected for a free calcium concentration of 1.0 ± 0.1 (s.e.m) μM as determined for the Chelex100-filtered buffer stock by titration with the chromophoric chelator 1,2-Bis(2-amino-5-bromophenoxy)ethane-N,N,N',N'-tetraacetic acid (5,5'-Dibromo-BAPTA) [54].

ADAMTS-13 cleavage assays. Proteolysis assays were performed essentially as described by Pos et al. [55]. Briefly, 5 μl of 6 nM recombinant ADAMTS-13 were pre-incubated in 20 mM Tris (pH 7.8), 150 mM NaCl, and 5 mM $CaCl_2$ (or $BaCl_2$) for 45 min at 37 °C before addition of 10 μM substrate (wt-, D1596A-, N1602A-A2 or hGH-VWF73). Similar reactions were also performed in the presence of 1.5 M urea. At these urea concentrations ADAMTS-13 is active [1,2,56]. After 1 h samples were analyzed by SDS gel electrophoresis on 15% Tris-Tricine gels.

Optical tweezers. A2 (residues 1478–1674) containing an N-terminal $(cmyc)_4$-tag and C-terminal Avi-tag were expressed in HEK293-EBNA1 cells. Protein was purified by Ni-NTA affinity chromatography followed by proteolytic cleavage of the His-Tag, biotinylated using BirA enzyme [57], and further purified by size exclusion chromatography in 20 mM HEPES (pH 7.5), 150 mM NaCl, containing 2.5 mM $CaCl_2$ (HBS-Ca) or 10 mM EDTA (HBS-EDTA). The dsDNA linker, anti-dig and anti-cmyc beads were prepared as described [58]. Typically, 1 μl anti-dig beads were diluted in 10 μl HBS and mixed

with 250 ng of dioxigenin- and biotin-labeled dsDNA. Likewise, 1 μl of a suspension of anti-cmyc beads was mixed with 1–4 μl of 1 mg ml^{-1} A2. After 30 min incubation on a rotary mixer, beads were resuspended in 250 μl HBS-Ca or HBS-EDTA for use in the optical tweezers experiments.
The optical tweezers setup was essentially as described [58]. Detection of forces on the trapped microsphere was performed using back focal plane interferometry. Forces were recorded at 50 Hz. Trap stiffness was 169±24 pN μm^{-1}, and sensitivity was 2.74±0.24 V μm^{-1}. A piezo-nanopositioning stage (Physik Instrumente) was used to move the sample cell and micropipette at a speed of 50 nm s^{-1}, resulting in a pulling rate on the tethered A2 construct of ~5 pN s^{-1} at unfolding. The microspheres were trapped in a flow chamber consisting of three parallel streams in laminar flow: one containing microspheres with A2, one containing microspheres with the DNA handle, and a central buffer channel in which the measurements took place. Statistical significance of mean unfolding forces derived from force distributions was tested using Student's t-test. Barnard's exact test was applied for differences in refolding probability.

Table 1 X-ray data collection and refinement statistics

Data collection	
Space group	C2
Cell dimensions	
a, *b*, *c* (Å)	156.0, 35.5, 88.5
a, b, g (°)	90, 96.3, 90
Resolution (Å)*	30.8–1.7 (1.79-1.70)
R_{merge}	8.5 (59.8)
$I / s I$	10.0 (2.8)
Completeness (%)	99.6 (99.1)
Redundancy	3.8 (3.8)
Refinement	
Resolution (Å)	29.3–1.7
No. reflections	51448
R_{work} / R_{free}	16.0(22.2)/19.4(26.2)
No. atoms	
Protein	4397
Ligand/ion	116/3
Water	586
B-factors (Å^2)	
Protein	15.6
Ligand/ion	27.3/16.2
Water	31.9
R.m.s. deviations	
Bond lengths (Å)	0.006
Bond angles (°)	2.9

Acknowledgements
We thank the European Synchrotron Radiation Facility (ESRF), Grenoble, France and the beamline scientists at ESRF ID23-2 for excellent support. The authors thank J. Voorberg and W. Pos of Sanquin Research (Amsterdam) for providing ADAMTS-13, S. Graham (Oxford University) for providing a BirA expression plasmid, and P. Bechtluft (AMOLF, Amsterdam) for his contribution to the early stages of the optical tweezers experiments. This work was supported by an ECHO grant of the Council for Chemical Sciences of the Netherlands Organization for Scientific Research to EGH.

Author contributions
AJ designed experiments, produced proteins, carried out crystallographic studies, performed and analyzed biochemical assays, MD simulations and optical tweezers experiments; AM performed and analyzed optical tweezers experiments; SJT designed and supervised optical tweezers experiments and data analysis; EGH conceived and supervised the project. AJ, EGH and SJT wrote the manuscript.

Accession codes. Atomic coordinates and structure factors have been deposited with the Protein Data Bank under accession code 3zqk.

Competing financial interests
The authors declare no competing financial interests

References

1. Sadler JE (1998) Biochemistry and genetics of von Willebrand factor. *Annu Rev Biochem* **67**, 395–424.
2. Ruggeri ZM (2003) Von Willebrand factor. *Curr Opin Hematol* **10**: 142–149.
3. Wagner DD (1990) Cell biology of von Willebrand factor. *Annu Rev Cell Biol* **6**: 217-246.
4. Fowler WE, Fretto LJ, Hamilton KK, Erickson HP, McKee PA (1985) Substructure of human von Willebrand factor. *J Clin Invest* **76**: 1491–1500.
5. Furlan M, Robles R, Lamie B (1996) Partial purification and characterization of a protease from human plasma cleaving von Willebrand factor to fragments produced by in vivo proteolysis. *Blood* **87**: 4223–4234.
6. Tsai H (1996) Physiologic cleavage of von Willebrand factor by a plasma protease is dependent on its conformation and requires calcium ion. *Blood* **87**: 4235–4244.
7. Sadler JE (2005) New concepts in von Willebrand disease. *Annu Rev Med* **56**: 173–191.
8. Sadler, JE (2008) Von Willebrand factor, ADAMTS13, and thrombotic thrombocytopenic purpura. *Blood* **112**, 11–18.
9. Goodeve A (2010) The genetic basis of von Willebrand disease. *Blood Rev* **24**: 123–134.
10. Moake JL et al. (1982) Unusually large plasma factor VIII:von Willebrand factor multimers in chronic relapsing thrombotic thrombocytopenic purpura. *N Engl J Med* **307**: 1432–1435.
11. Gao W, Anderson P, Sadler J (2008) Extensive contacts between ADAMTS13 exosites and von Willebrand factor domain A2 contribute to substrate specificity. *Blood* **112**: 1713–1719.
12. Zhang Q et al. (2009) Structural specializations of A2, a force-sensing domain in the ultralarge vascular protein von Willebrand factor. *Proc Natl Acad Sci USA* **106**, 9226–9231.
13. Zhang X, Halvorsen K, Zhang C-Z, Wong WP, Springer TA (2009) Mechanoenzymatic cleavage of the ultralarge vascular protein von Willebrand factor. *Science* **324**: 1330–1334.
14. Akiyama M, Takeda S, Kokame K, Takagi J, Miyata T (2009) Crystal structures of the noncatalytic domains of ADAMTS13 reveal multiple discontinuous exosites for von Willebrand factor. *Proc Natl Acad Sci USA* **106**: 19274–19279.
15. Zhou M et al. (2011) A novel calcium-binding site of von Willebrand factor A2 domain regulates its cleavage by ADAMTS13. *Blood* **117**: 4623–4631.
16. Harding MM (2004) The architecture of metal coordination groups in proteins. *Acta Crystallogr D Biol Crystallogr* **60**: 849–859.
17. Harding MM (2002) Metal-ligand geometry relevant to proteins and in proteins: sodium and potassium. *Acta Crystallogr D Biol Crystallogr* **58**: 872–874.
18. Harding MM (2001) Geometry of metal-ligand interactions in proteins. *Acta Crystallogr D Biol Crystallogr* **57**: 401–11.
19. Emsley J, Cruz M, Handin R, Liddington R (1998) Crystal Structure of the von Willebrand Factor A1 Domain and Implications for the Binding of Platelet Glycoprotein Ib. *J Biol Chem* **273**: 10396–10401.
20. Huizinga EG, van der Plas RM, Kroon J, Sixma JJ, Gros P (1997) Crystal structure of the A3 domain of human von Willebrand factor: implications for collagen binding. *Structure* **5**: 1147–1156.
21. Tozer EC, Liddington RC, Sutcliffe MJ, Smeeton AH, Loftus JC (1996) Ligand binding to integrin alphaIIbbeta3 is dependent on a MIDAS-like domain in the beta3 subunit. *J Biol Chem* **271**: 21978–21984.
22. Loftus JC, Liddington, RC (1997) New insights into integrin-ligand interaction. *J Clin Invest* **99**: 2302–2306.
23. Lee JO, Bankston LA, Arnaout MA, Liddington RC (1995) Two conformations of the integrin A-domain (I-domain): a pathway for activation? *Structure* **3**: 1333–1340.
24. Pantoliano M. et al. (2001) High-density miniaturized thermal shift assays as a general strategy for drug discovery. *J Biomol Screen* **6**: 429-440.
25. Ericsson U, Hallberg B, DeTitta G, Dekker N, Nordlund P (2006) Thermofluor-based high-throughput stability optimization of proteins for structural studies. *Anal Biochem* **357**: 289–298.
26. Lo M.-C. et al. (2004) Evaluation of fluorescence-based thermal shift assays for hit identification in drug discovery. *Anal Biochem* **332**: 153–159.
27. Kokame K, Matsumoto M, Fujimura Y & Miyata T (2004) VWF73, a region from D1596 to R1668 of von Willebrand factor, provides a minimal substrate for ADAMTS-13. *Blood* **103**: 607–612.
28. Bustamante C, Marko JF, Siggia ED & Smith S (1994) Entropic elasticity of lambda-phage DNA. *Science* **265**: 1599–1600.
29. Ainavarapu SRK. et al. (2007) Contour length and refolding rate of a small protein controlled by engineered disulfide bonds. *Biophys J* **92**: 225–233.
30. Ying J, Ling Y, Westfield LA, Sadler JE, Shao J-Y (2010) Unfolding the A2 domain of von Willebrand factor with the optical trap. *Biophys J* **98**: 1685–1693.

31. Ruggeri ZM, Orje JN, Habermann R, Federici AB, Reininger AJ (2006) Activation-independent platelet adhesion and aggregation under elevated shear stress. *Blood* **108**: 1903–1910.

32. Sing CE, Alexander-Katz A (2010) Elongational flow induces the unfolding of von Willebrand factor at physiological flow rates. *Biophys J* **98**: L35–37.

33. Alexander-Katz A, Schneider MF, Schneider SW, Wixforth A, Netz RR (2006) Shear-flow-induced unfolding of polymeric globules. *Phys Rev Lett* **97**: 138101.

34. Schneider SW et al. (2007) Shear-induced unfolding triggers adhesion of von Willebrand factor fibers. *Proc Natl Acad Sci USA* **104**: 7899–7903.

35. Bode W, Gomis-Rüth FX,Stöckler W (1993) Astacins, serralysins, snake venom and matrix metalloproteinases exhibit identical zinc-binding environments (HEXXHXXGXXH and Met-turn) and topologies and should be grouped into a common family, the 'metzincins'. *FEBS Lett* **331**, 134–140.

36. Porter S, Clark IM, Kevorkian L, Edwards DR (2005) The ADAMTS metalloproteinases. *Biochem J* **386**: 15–27.

37. Anderson PJ, Kokame K & Sadler JE (2006) Zinc and calcium ions cooperatively modulate ADAMTS13 activity. *J Biol Chem* **281**: 850–857.

38. Schwaiger I, Schleicher M, Noegel AA, Rief M. (2005) The folding pathway of a fast-folding immunoglobulin domain revealed by single-molecule mechanical experiments. *EMBO Rep* **6**: 46–51.

39. Schlierf M, Berkemeier F, Rief M (2007) Direct observation of active protein folding using lock-in force spectroscopy. *Biophys J* **93**: 3989–3998.

40. Berkovich R, Garcia-Manyes S, Klafter J, Urbakh M, Fernández JM (2010) Hopping around an entropic barrier created by force. *Biochem Biophys Res Commun* **403**: 133–137.

41. Huizinga EG et al. (2002) Structures of glycoprotein Ibalpha and its complex with von Willebrand factor A1 domain. *Science* **297**: 1176–1179.

42. Kabsch W (2010) XDS. *Acta Crystallogr D Biol Crystallogr* **66**: 125–132.

43. Collaborative Computational Project 4. (1994) The CCP4 suite: programs for protein crystallography. *Acta Crystallogr D Biol Crystallogr* **50**: 760–763.

44. McCoy AJ et al. (2007) Phaser crystallographic software. *J. Appl. Crystallogr.* **40**: 658–674.

45. Langer G, Cohen SX, Lamzin VS, Perrakis A (2008) Automated macromolecular model building for X-ray crystallography using ARP/wARP version 7. *Nat Protoc* **3**: 1171–1179.

46. Emsley P, Cowtan K (2004) Coot: model-building tools for molecular graphics. *Acta Crystallogr D Biol Crystallogr* **60**: 2126–2132.

47. Adams PD et al. (2010) PHENIX: a comprehensive Python-based system for macromolecular structure solution. *Acta Crystallogr D Biol Crystallogr* **66**: 213–221.

48. Chen VB et al. (2010) MolProbity: all-atom structure validation for macromolecular crystallography. *Acta Crystallogr D Biol Crystallogr* **66**: 12–21.

49. Van Der Spoel D et al. (2005) GROMACS: fast, flexible, and free. *J Comp Chem* **26**: 1701-1718.

50. Jorgensen W, Ulmschneider J, Tirado-Rives J (2004) Free energies of hydration from a generalized Born model and an ALL-atom force field. *J Phys Chem B* **108**: 16264–16270.

51. Lawrence C, Skinner J (2003) Flexible tip4p model for molecular dynamics simulation of liquid water. *Chem. Phys Lett* **372**: 842–847.

52. Darden T, York D, Pedersen L (1993) Particle mesh Ewald: An N · log (N) method for Ewald sums in large systems. *J Chem Phys* **98**: 10089-10092.

53. Hess B, Bekker H, Berendsen H, Fraaije J (1997) LINCS: a linear constraint solver for molecular simulations. *J Comp Chem* **18**: 1463–1472.

54. Linse, S. Calcium Binding to Proteins Studied via Competition with Chromophoric Chelators. in *Calcium-Binding Protein Protocols*, Vol. 2 (ed. Vogel, H.J.) (Humana Press, Totowa, NJ, 2002).

55. Pos W et al. (2010) An autoantibody epitope comprising residues R660, Y661, and Y665 in the ADAMTS13 spacer domain identifies a binding site for the A2 domain of VWF. *Blood* **115**: 1640–1649.

56. Zanardelli S et al. (2006) ADAMTS13 substrate recognition of von Willebrand factor A2 domain. *J Biol Chem* **281**: 1555–1563.

57. Howarth M, Howarth M, Ting AY, Ting AY (2008) Imaging proteins in live mammalian cells with biotin ligase and monovalent streptavidin. *Nat Protoc* **3**: 534–545.

58. Bechtluft P et al. (2007) Direct observation of chaperone-induced changes in a protein folding pathway. *Science* **318**: 1458–1461.

Supplementary Information

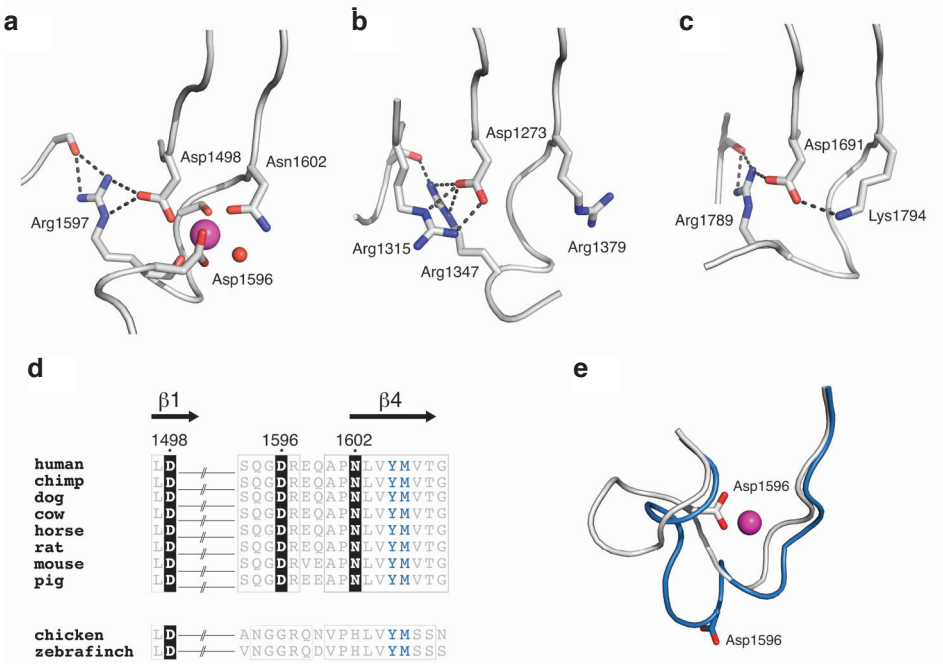

Supplementary Figure S1 The calcium-binding site of VWF-A2. Close up of the $\alpha_3\beta_4$ loop of (a) VWF-A2, (b) VWF-A1 and (c) VWF-A3. In all VWF-A domains, $\alpha_3\beta_4$ is anchored via electrostatic interaction between a conserved aspartate in β_1 and a conserved arginine in the $\alpha_3\beta_4$ loop. In agreement with our results from thermal stability assays structural comparison shows that among the VWA domain repeat, metal binding functionality at this site is unique to A2. In A2 calcium binds to a negatively charged pocket formed by the $\alpha_3\beta_4$ loop. In A1 and A3, the positively charged side chains of A1-Arg1374 and A3-Lys1794, which replace A2-Asn1602, point into the cavity formed by the $\alpha_3\beta_4$ loop, obliterating calcium binding by charge repulsion. Key side chains are shown as sticks; calcium ion, magenta sphere; H_2O, red sphere. (d) Asp1596 and Asn1602 that coordinate calcium through side chain atoms are strictly conserved in mammalian, but absent from avian VWF sequences. (e) Calcium coordination by A2 leads to a marked rearrangement of the $\alpha_3\beta_4$ loop triggered by Asp1596, which moves more than 16 Å to coordinate the calcium ion.

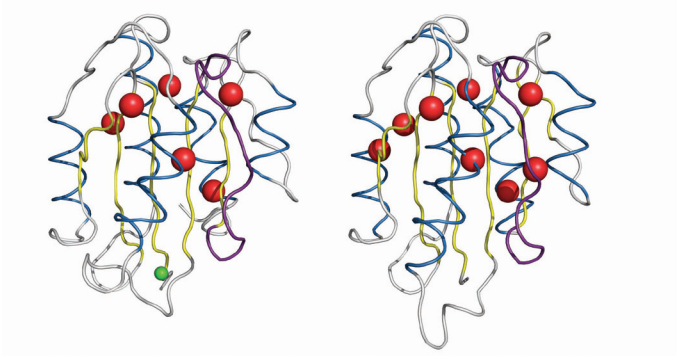

Supplementary Figure S2 Global packing analysis of calcium-bound A2 (left) and calcium-free A2 (right; PDB 3GXB). A Voronoi cell algorithm [59] was applied to determine local packing densities and interior cavities. The α_4-less loop is shown in purple; the calcium ion in green; local cavities due to packing defects are depicted as red spheres. Both structures show similar packing defects on either side of the central beta sheet, indicating that the stabilizing effect observed by calcium binding is not due to overall improvement of side chain packing.

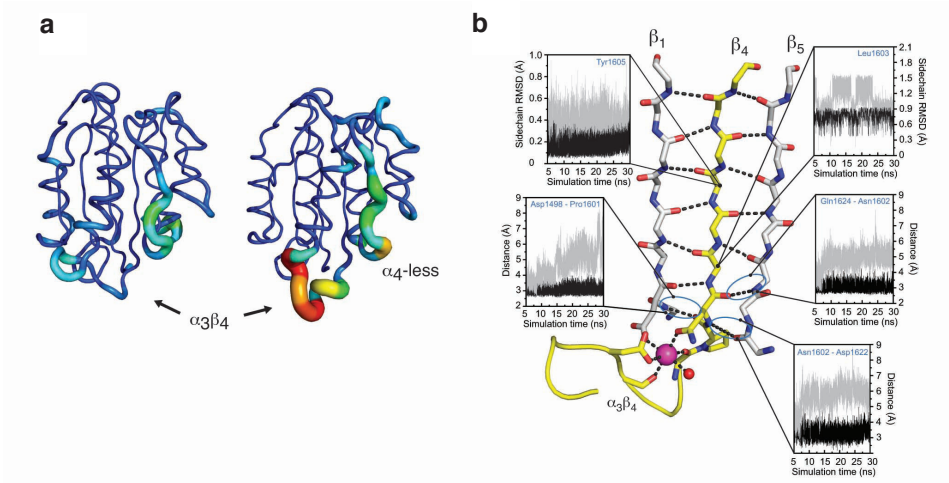

Supplementary Figure S3 Calcium binding modulates dynamics of $\alpha_3\beta_4$ and scissile strand β_4. (a) Root mean square fluctuations of the protein main chain averaged over three independent 30 ns molecular dynamics simulations are projected onto the tube representation of the backbone traces of calcium-bound (left) and calcium-free (right) A2. Rmsf amplitudes are represented by tube diameter and color-coded by decreasing amplitude from red (4 Å) to blue (0.3 Å). Consistent with the experimental B-factor distributions in the calcium-free system we observe highest rmsf values for the $\alpha_3\beta_4$ and α_4-less loops that both flank the scissile strand. In particular, the $\alpha_3\beta_4$-loop deviates markedly from the reference conformation of the starting structure. As anticipated, this loop is significantly less flexible in the calcium-bound ensemble. It can be appreciated that the large movements of the flanking loop regions in the calcium-free structure impose substantial strain on the β_4-strand. This is reflected by the quality of hydrogen bonds formed during the simulation between β_4 and its neighboring strands. (b) Backbone representation of the β4 scissile strand (yellow) and neighboring strands illustrating how calcium interlocks β_4 with β_1 via coordination by Asp1498 and Asn1602. Also depicted are representative trajectories for selected hydrogen bond donor-acceptor distances and side chain rmsds from molecular dynamics simulations of calcium-free (gray) and calcium-bound (black) A2, showing that metal coordination directly affects the dynamics of scissile strand β_4. Throughout the simulations marked deviations from ideal hydrogen-bond geometries are observed for the calcium-free structures on either side of the β_4 strand.

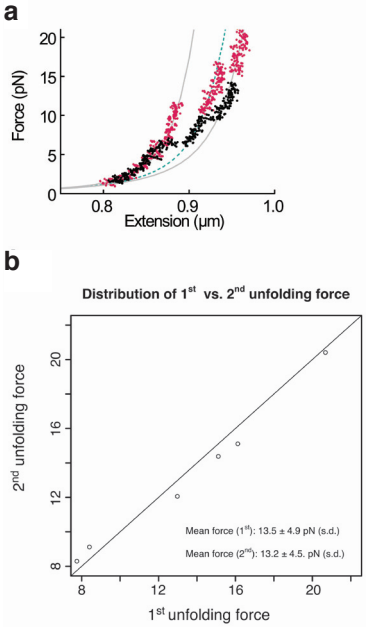

Supplementary Figure S4 Analysis of force spectroscopy data. (a) Representative trace for rare unfolding transitions in the presence of EDTA (black) that proceeds via an intermediate. Comparison with a trace in the presence of calcium (red) indicates that the intermediates follow the same WLC. (b) Q-Q plot of force distributions obtained from a first stretching experiment and a second stretch after refolding at zero force for A2 with calcium (n1=6, n2=6); mean forces for both distributions are listed. The similarity of force distributions resulting from the first and a second stretch indicate that A2 refolds to the native conformation. In the presence of EDTA mean force for unfolding were 7.8 ± 2.9 pN (s.d.) for the first stretch, and a similar 6.8 ± 3.7 pN (s.d.) after refolding

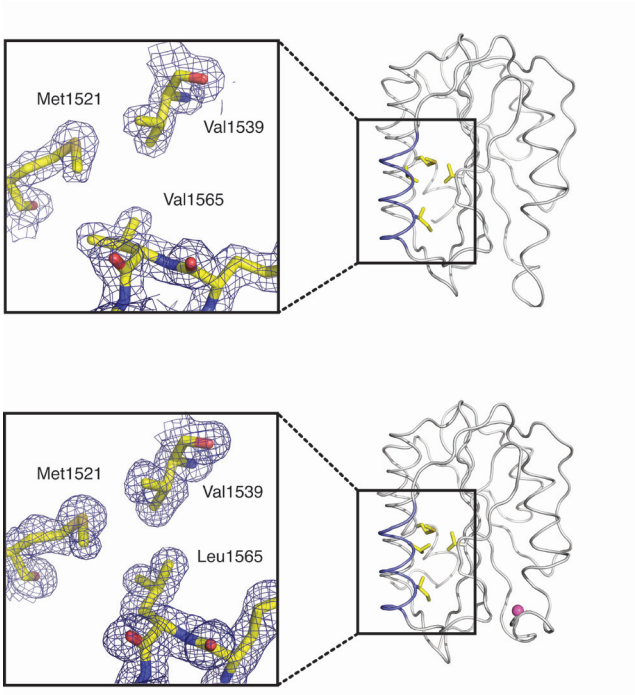

Supplementary Figure S4 Location of the V1565L polymorphism within the A2 structure. We crystallized an A2 variant carrying a 4693G/T single nucleotide polymorphism (SNP), leading to the amino acid substitution V1565L within helix α_2. This polymorphism is reported to slightly increase VWF proteolysis [60], but has not been listed as a VWD 2A mutant (www.shef.ac.uk/vwf). Close up of the environment of Val1565 in PDB 3GXB (top) and Leu1565 in calcium-bound A2 (bottom). The right panels show the location of the polymorphism in the overall structure. The α_2-helix is highlighted in purple and important side chains that interact with residue 1565 are shown in yellow. Leu1565 in calcium-bound A2 forms favorable contacts with Met1521 and Val1639, allowing for tighter packing than observed for the wild type Val1565 (left) in PDB 3GXB. This is also evident from the analysis of local packing densities (Supplementary Fig. S2), where we find a packing defect for PDB 3GXB at this position. From our analysis we are not able to identify a structural explanation for the observed increase in proteolysis rate of the Leu1565 variant.

Supplementary Table 1 Geometry of the calcium-binding site

Residue	Atom	Monomer A		Monomer B		Monomer C		Reference values (‡)
		Distance (Å)	B (Å^2)	Distance (Å)	B (Å^2)	Distance (Å)	B (Å^2)	Distance (Å)
Asp498	OD2	2.35	9.6	2.37	11.4	2.35	14.1	2.36 ± 0.11
Asp1596	OD1	2.35	12.6	2.35	24.1	2.34	22.7	2.36 ± 0.11
Arg1597	O	2.37	12.8	2.38	10.7	2.38	12.5	2.36 ± 0.13
Ala1600	O	2.35	13.7	2.37	11.0	2.37	13.8	2.36 ± 0.13
Asn1602	OD	2.43	9.1	2.42	9.7	2.42	9.4	2.40 ± 0.11
H_2O	O	2.60	18.7	2.63	25.5	2.62	23.1	2.42 ± 0.16
Calcium	CA		16.2		13.4		16.8	

Supplementary References

59. Rother K, Hildebrand PW, Goede A, Gruening B, Preissner R (2009) Voronoia: analyzing packing in protein structures. *Nucleic Acids Res* **37**: 393-395.

60. Davies J, Bowen D (2007) An association between the L1565 variant of von Willbrand factor and susceptibility to proteolysis by ADAMTS-13. *Haematologica* **92**: 240-243

CHAPTER 3

Mechanistic studies of ADAMTS-13 substrate specificity

Arjen J. Jakobi and Eric G. Huizinga

Crystal & Structural Chemistry, Bijvoet Center for Biomoelcular Research, Department of Chemistry, Utrecht University, Padualaan 8, 3584 CH Utrecht, The Netherlands

Manuscript in preparation

ADAMTS-13 (a disintegrin and metalloprotease with thrombospondin type 1 motif, member 13) regulates haemostatic potency of von Willebrand factor (VWF) by cleaving VWF multimers at Tyr1605-Met1606 in the A2 domain. Cleavage requires unfolding of the A2 domain by hydrodynamic forces and is influenced by calcium binding to A2. We studied substrate specificity of ADAMTS-13 by screening of VWF-A2 mutants and investigated the mechanism by which naturally occurring A2 variants Pro1601Thr, Leu1603Pro and Val1604Phe affect ADAMTS-13 cleavage efficiency. An extensive series of P5-P1' variants of the unstructured hGH-VWF73 substrate was prepared for kinetic analysis. We used the kinetic data in conjunction with molecular dynamics simulations to propose an improved model of substrate binding at the active site. We demonstrate that the specificity of ADAMTS-13 is not primarily conferred by the Tyr1605-Met1606 motif, but rather by the P3 and P1 residues. P3 mainly determines substrate affinity whereas P1 is essential for proper positioning of the scissile bond in the catalytic site. The P2 residue is only marginally involved in substrate binding, but ensures proper orientation of residues P1 and P3. These features, in combination with the previously characterized exosites in ADAMTS-13 appear to curtail the high specificity of ADAMTS-13 for its substrate VWF. The natural sequence variants studied affect ADAMTS-13 cleavage efficiency toward the hGH-VWF73 construct and modulate calcium binding and/or stability of the natively folded A2 domain. Our data suggest that disrupted calcium binding by the Leu1603Pro variant may be an important factor contributing to its type 2A von Willebrand disease phenotype.

Von Willebrand factor (VWF) is a multimeric plasma glycoprotein with an essential role in platelet-dependent haemostasis under conditions of elevated hydrodynamic shear forces, such as found in the arteriolar system. The potency of VWF to recruit platelets is dependent on the length of its multimers [1]. Stimulated endothelial cells secrete ultra-large VWF

multimers (ULVWF), which are particularly efficient in binding platelets [2]. To preserve normal haemostasis, the thrombogenic potential of these ULVWF multimers is regulated through proteolytic cleavage by ADAMTS-13, a plasma resident member of the ADAMTS family of secreted zinc metalloproteases [3,4]. Pathological disorders associated with compromised functioning of ADAMTS-13 lead to accumulation of large VWF multimers that induce the formation of platelet-rich microvascular thrombi [5,6], which are the pathological hallmark of the occlusive microangiopathy thrombotic thrombocytopenic purpura (TTP) [7]. Conversely, mutations in the A2 domain that render VWF more susceptible to cleavage by ADAMTS-13 lead to a loss of large multimers in plasma and result in the bleeding tendency associated with type 2A von Willebrand disease (VWD) [8].

ADAMTS-13 is a multidomain protease that circulates in plasma in its catalytically active form. ADAMTS-13 cleaves VWF at the Tyr1605-Met1606 peptide bond located in the A2 domain [3,4]. Proteolytic cleavage requires activation of the substrate by shear-induced unfolding of the A2 domain to expose the scissile bond [3,9]. Since ADAMTS-13 is constitutively active, accessibility of the cleavage site is important in regulating the extent of VWF cleavage in vivo. Using optical tweezers to mechanically unfold A2, we have recently demonstrated that accessibility of the cleavage site is modulated by calcium binding at the $\alpha_3\beta_4$ loop in the A2 domain, which restricts exposure of the scissile bond by mechanically stabilizing A2 and promoting refolding into its native conformation [10]. The remarkable specificity of ADAMTS-13 toward VWF has been attributed mainly to cooperative interactions between substrate sequences and an extended array of exosites located in the non-catalytic domains of ADAMTS-13, at substantial distance from the active site (**Fig. 1A,B**) [11-16]. Importantly, binding to all of these exosites is required to preserve full proteolytic activity [17-19]. The isolated metalloprotease domain appears to have no detectable affinity for VWF [18]. However, its high specificity toward hydrolyzing the Tyr1605-Met1606 peptide bond suggests that the metalloprotease domain does contain recognition elements important for specific cleavage at this site. Accordingly, deletion and substitution of substrate residues in the immediate vicinity of the scissile bond have been found to prevent cleavage [12]. Moreover, sequences of the metalloprotease domain that are variable between the different members of the ADAMTS family were demonstrated to affect proteolytic activity and substrate specificity, and are therefore predicted to form the substrate binding pockets around the active site [20,21]. The precise molecular determinants that define specificity, however, remained poorly understood. More recently, mutagenesis studies by us and others have established a critical role in proteolytic activity of substrate residues Leu1603 (residue P3) and Val1604 (residue P2) [10,22] (by convention, substrate residues surrounding the cleavage site are denoted …P2-P1-P1'-P2'…, where the scissile bond is located between the P1 and P1' residues. The corresponding binding sites in the enzyme are referred to as …S2-S1-S1'-S2'…, where S2 interacts with the P2 residue of the substrate etc.). It has recently been proposed that P3 and P2 substrate residues act in conjunction with the various exosites in positioning the scissile bond at the active site [22]. In the present study we develop a detailed model of substrate specificity of the ADAMTS-13 metalloprotease domain by extensively screening the effect on catalysis

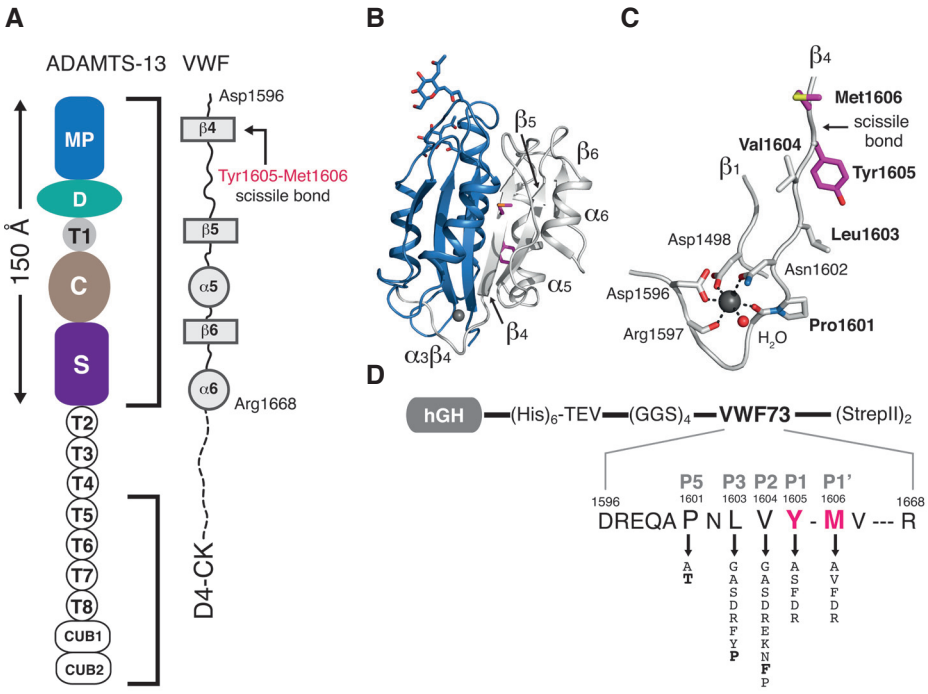

Fig. 1 VWF and ADAMTS-13. (A) Schematic representation of the ADAMTS-13 domain organization (left). Exosites interacting with carboxyl-terminal binding sites in the unfolded A2 domain (right) are located in the metalloprotease (MP), disintegrin (D), thrombosponding-type 1 (T1), cysteine-rich (C) and spacer (S) domain of ADAMTS-13. The carboxyl-terminal T5-CUB2 domains interact with VWF domains other than A2. (B) Crystal structure of VWF-A2 (PDB ID 3zqk) shown in cartoon representation. The Tyr1605-Met1606 scissile bond (magenta sticks) is buried in the native conformation. Unfolding exposes the carboxyl-terminal sequence (gray) including the scissile bond. This sequence contains several binding sites that can cooperatively interact with the various exosites in ADAMTS-13. GlcNAGs of N-linked glycans are shown as blue sticks, the calcium ion as sphere. (C) Close-up of the scissile bond environment including the calcium-binding site. (D) VWF73 and its variants. Schematic representation of the VWF73 construct (Asp1596 – Arg1668 of VWF) fused to human growth hormone (hGH). A $(GlyGlySer)_4$ linker serves to ensure an average 15 Å separation of VWF73 from the fusion protein. The cleavage site between Tyr1605 and Met1606 is highlighted in magenta. Arrows indicate individual VWF73 variants of residues at position P5 (P1601), P3 (Leu1603), P2 (Val1604), P1 (Tyr1605) and P1' (Met1606). Naturally occurring sequence variants are highlighted in bold.

of single-point mutations at substrate positions P5 (P1601) to P1' (Met1606). On the basis of homology modeling and molecular dynamics simulations, we propose a provisional structural model for substrate binding by the ADAMTS-13 metalloprotease domain that is consistent with the discriminatory subsite preferences observed in our cleavage assays and points towards an important role of the scissile bond geometry for optimal catalytic activity. By assessing cleavage efficiency toward the naturally occurring sequence variants Pro1601Thr, Leu1603Pro and Val1604Phe in the hGH-VWF73 substrate, as well as their effect on calcium binding and stability of the full-length A2 domain, we further establish the mechanism by which these variants affect VWF multimer size distribution in vivo.

Results

Functional analysis of VWF variants

In the absence of structural information of the ADAMTS-13 substrate interaction, we set out to further refine the precise molecular determinants in the immediate vicinity of the Tyr1605-Met1606 scissile bond that define ADAMTS-13 specificity. We introduced single amino acid substitutions at the P5 (Pro1601), P3 (Leu1603), P2 (Val1604), P1 (Tyr1605) and P1' (Met1606) positions in a recombinant substrate fragment spanning VWF residues Asp1596-Arg1668 of the A2 domain flanked by the human growth hormone (hGH) and a $(His)_6$ tag at the amino terminus and a $(StrepII)_2$ tag at the carboxyl terminus (hGH-VWF73; **Fig. 1D**). Unlike the native A2 domain and multimeric VWF, this fragment is permissive to ADAMTS-13 cleavage under physiologic buffer conditions. To examine the functional importance of the P5-P1' substrate residues, we analyzed proteolytic cleavage by SDS-PAGE and quantified the activity of ADAMTS-13 toward the hGH-VWF73 variants by densitometry of the reaction products (**Fig. 2A**).

Leu1603 and Tyr1605 are the main determinants of ADAMTS-13 substrate specificity

The most pronounced effect on proteolytic activity was observed for variants of Leu1603 and Tyr1605 at the P3 and P1 positions (**Fig. 2A**). Whereas variants of Leu1603 with polar (Leu1603Ser) or charged residues (Leu1603Asp, Leu1603Arg), as well as increased main chain flexibility (Leu1603Gly), drastically reduced proteolytic activity, variants with small aliphatic (Leu1603Ala) and aromatic side chains (Leu1603Phe) were cleaved efficiently by ADAMTS-13 (**Fig. 2A,B**). In agreement with a recent study using similar constructs [22], our data suggest a preference of ADAMTS-13 for hydrophobic substrate residues at its S3 site and, in addition, demonstrate that this site is quite insensitive to the size of the P3 residue. The preference for apolar residues at the S3 site is particularly evident from a direct comparison of the P3 Ala and Ser or Phe and Tyr variants. Although each individual variant pair has similar steric requirements, the polar hydroxyl substituent substantially reduces cleavage efficiency (**Fig. 2A,B,D**).

Variants of the P1 residue (Tyr1605) all showed reduced cleavage levels (**Fig. 2A,E**). Charged variants (Tyr1605Asp, Tyr1605Arg) were particularly poor substrates. Interestingly, in spite of its direct involvement in the proteolytic reaction, the relative differences in cleavage efficiency for variants of Tyr1605 at the P1 position are less prominent than those observed for similar variants of Leu1603 at position P3. This observation indicates that the ADAMTS-13 metalloprotease domain does not primarily discriminate the scissile peptide bond through S1 subsite selectivity, but requires adjacent subsites, and possibly exosites for accurate positioning of the scissile residues at the active site.

We determined catalytic parameters of a subset of interesting variants by quantifying initial product formation as a function of substrate concentration (**Fig. 3A**). Due to technical limitations of densitometric quantification, we had to restrict our analysis to variants that have > 15 % cleavage efficiency compared to the wild-type sequence. Notably, we found an apparent K_M of 10.2±1.8 μM (s.d.) for the wild-type hGH-VWF73 sequence, which is approximately 6-fold higher than previously reported for similar substrates [11,23,24].

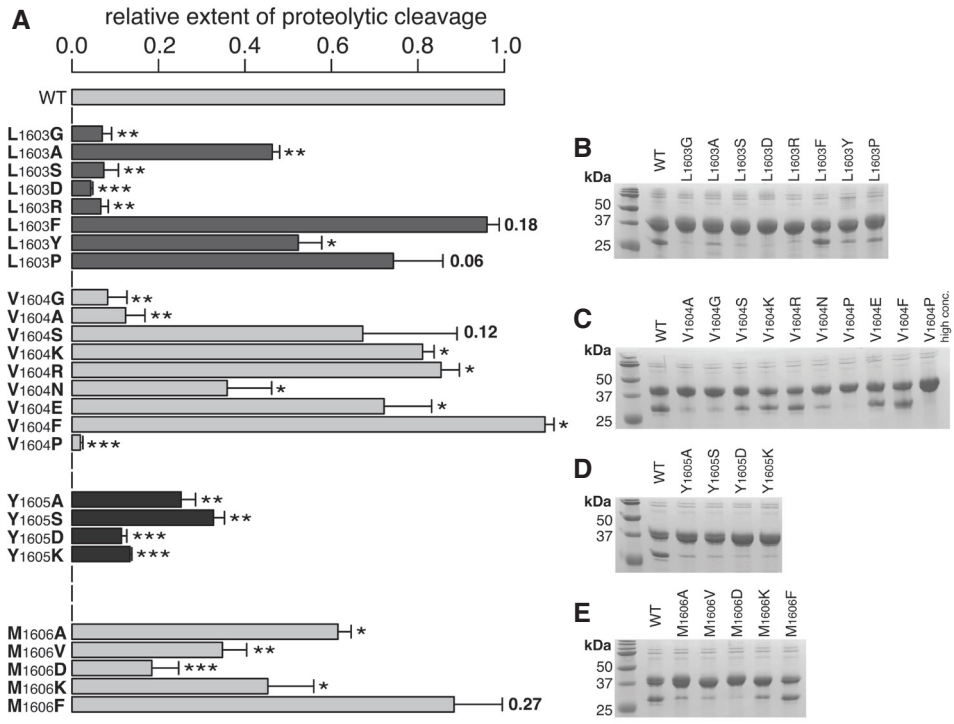

Fig. 2 Effect of hGH-VWF73 P3-P1' variants on cleavage by ADAMTS-13. (A) Bar diagrams of cleavage levels as quantified by densitometry. Average cleavage efficiencies are expressed as the relative extent of proteolytic cleavage levels with respect to the WT-VWF73 sequence. Error bars represent s.d. (n=3-6). Asteriks indicate significance levels from a two-tailed t test with $P < 0.05$ (*), $P < 0.001$ (**) and $P < 0.0001$ (***). P values are stated explicitly otherwise. (B-E) Representative Coomassie stained SDS-PAGE gels of individual VWF73 substrate variants (6 μM) after 60 min cleavage with ADAMTS-13 (2-4 nM). Heterogeneity of the substrate arises from different N-linked glycosylation of hGH in the chimeric construct, but does not affect cleavage of the substrate.

We cannot currently decide whether this discrepancy is a consequence of variations in assay conditions, or of disparity in substrate or enzyme. However, for the Tyr1605Ala and Met1606Ala variants for which kinetic data is available form other studies [20,21,25], we find similar changes in specificity constants k_{cat}/K_M compared to wild-type. Our data show that proteolytic cleavage of the Leu1603Phe variant proceeds with a k_{cat}/K_M similar to that observed for the wild-type sequence (**Fig. 3A,B**). The moderate increase in apparent K_M for this variant furthermore confirms that occupancy of the S3 subsite is not restricted by steric factors. In agreement with previous observations [22], we observe a reduction of k_{cat}/K_M for the Tyr1605Ala variant of approximately 30-fold. Notably, this difference arises from a modest twofold increase in K_M and an associated 15-fold decrease in substrate turnover as reflected by the catalytic rate constant k_{cat}, which has a value of 0.08 s^{-1} compared to 1.2 s^{-1} for the wild-type sequence. From the relative contribution of these parameters we conclude that Tyr1605 at P1 is not essential for substrate recognition, but important for catalytic turnover. In support of this argument, variants with other aromatic side chains (Tyr1605Phe, Tyr1605Trp) are cleaved with similar efficiency as the wild-type

A

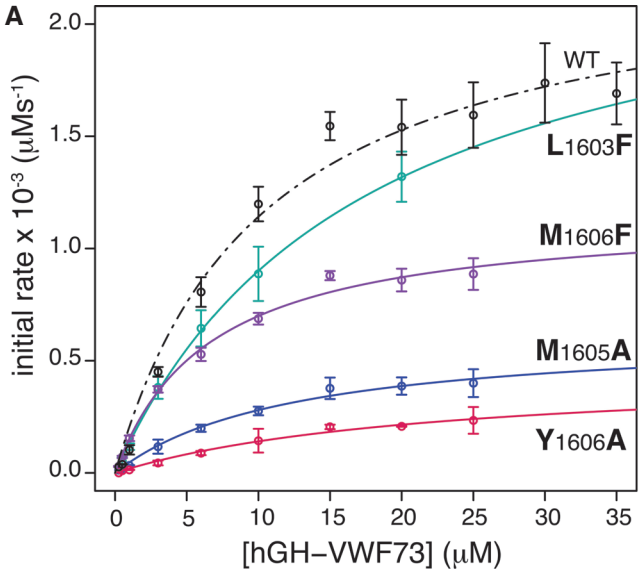

Fig. 3 Kinetic characterization of hGH-VWF73 constructs. (A) Determination of catalytic constants for selected variants from cleavage at different substrate concentrations. Product formation after 15 min was quantified by densitometry as the ratio of cleaved and uncleaved substrate. Error bars report s.d. (n=3). Lines are non-linear regression fits of the Michaelis-Menten equation to the experimental data. (B) Tabulated catalytic constants. Efficiency index reports the k_{cat}/K_M ratio between variant and WT.

B

	K_M (μM)	k_{cat} (s^{-1})	k_{cat}/K_M (10^4 x $M^{-1}s^{-1}$)	Efficiency index*
WT	10.2 ± 1.8	1.2 ± 0.08	12 ± 0.2	-
L1603F	17.3 ± 1.7	1.3 ± 0.07	7.5 ± 0.1	0.66
Y1605A	22.3 ± 5.7	0.08 ± 0.01	0.37 ± 0.3	0.03
M1606A	12.4 ± 2.1	0.12 ± 0.01	1.0 ± 0.2	0.08
M1606F	6.6 ± 0.9	0.6 ± 0.03	9.2 ± 0.1	0.77

sequence [26]. Together, these data underline the requirement for strong non-polar contacts at the P1 site for optimal catalytic turnover.

Val1604 is required for proper positioning of P3 and P1 residues

Our results presented in the previous section demonstrate that important factors determining specificity of ADAMTS-13 toward the VWF Tyr1605-Met1606 peptide bond reside within the S3 and S1 subsites of the catalytic metalloprotease domain. However, we have recently found that a Val1604Ala variant at the P2 position also displays severely impaired cleavage, suggesting that the P2 residue contributes to substrate recognition [10]. To further investigate the importance of the P2 residue, we systematically substituted Val1604 with a broad panel of different residues (see **Fig. 1D**). As opposed to the P3 and P1 sites, we found proteolytic activity of ADAMTS-13 toward the Val1604 variants to be largely insensitive to the physicochemical properties of the residue at the P2 position. Catalytic efficiency toward charged (Val1604Glu, Val1604Lys, Val1604Arg) and polar (Val1604Ser) P2 residue variants was not, or only moderately affected (**Fig. 2A,C**). In contrast to substitution by bulky substituents, exchange of Val1604 with small residues (Val1604Gly, Val1604Ala) as well as proline severely reduced cleavage. These residues

expand (Gly, Ala) or constrain (Pro) the conformational space of main chain dihedral angles relative to that accessible by other amino acids, which suggests that the observed differences in cleavage efficiency can be attributed to different propensities in populating a particular main chain conformation that serves to position P3 and P1 residues into their respective subsites. Consistent with this hypothesis is the observation that cleavage of the Val1604Asn variant is also markedly decreased. Asparagine is frequently found in partially allowed (high energy) regions of the Ramachandran map and shows a general preference for regions outside regular secondary structure, a property generally attributed to its unique ability of forming dipole-dipole interactions between the side chain and main chain carbonyl groups [27,28]. Together, our data demonstrate that ADAMTS-13 has loose subsite preferences at the P2 position, indicating that the S2 site is not well defined and that P2 likely does not contribute side chain interactions important for recognition of the substrate.

Interestingly, the effect on cleavage efficiency of most variants of Met1606 at the P1' position was less prominent than observed for substrate residues P3 and P1 (**Fig. 2A, Fig. 3A,B**), indicating that the S1' subsite in ADAMTS-13 is rather tolerant in accepting residues with physicochemical properties different from those in the natural substrate. Promiscuity at the scissile P1' position is also observed for ADAMTS-4, which was shown to efficiently cleave Glu-Ala, Glu-Gly and Glu-Leu peptide bonds [27, 28]. Analogous to the Tyr1605Ala mutant, kinetic parameters of the Met1606Ala and Met1606Phe variants show that the reduced catalytic activity is primarily linked to differences in turnover number k_{cat} (**Fig. 3B**).

Modeling substrate binding at the active site

In an attempt to rationalize our mutagenesis data in terms of molecular interactions, we built a homology model of the ADAMTS-13 metalloprotease domain (see Methods) and manually docked a substrate peptide spanning VWF residues Leu1603-Met1606 into this model. Docking of the peptide was guided by reported experimental data of ADAMTS-13 subsite selectivity [10,20-22] and sequence-structure-function information available for the metalloprotease domains of ADAMTS family members and related matrix metalloproteases (MMPs) [29-32]. Since the architecture of the Zn^{2+}-coordinating active site is well conserved among all of the structurally characterized metalloprotease domains of ADAMTS members [32-36] and MMPs [30], it is reasonable to assume that this is also the case for ADAMTS-13. Formation of the Michaelis complex requires coordination of the Zn^{2+} ion by the carbonyl oxygen of the P1-P1' peptide bond [30], which provides a stringent restraint on the position of the P1 residue. Further restraints on substrate binding are imposed by the presence of a characteristic linear cleft extending from the catalytic Zn^{2+} ion and walled off on one side by the β_4 strand in all structurally characterized ADAMTS metalloprotease domains [32-36]. This cleft likely accommodates the substrate in an extended conformation as is also observed for MMPs for which structural data on substrate binding are available [30]. In addition, the relative location of exosites with respect to the metalloprotease domain [37] defines the direction of substrate binding in ADAMTS-13

(**Fig. 1A,B**). On the basis of these restraints, we derive two putative binding modes that differ mainly in the conformation of the Tyr1605 side chain and hence in the location and physicochemical properties of the S1 pocket.

In binding mode A P1 residue Tyr1605 is partially exposed to solvent, whereas the phenolic side chain is buried by the ADAMTS-13 $\beta_3\beta_4$ loop in binding mode B (**Fig. 4A**). The $\beta_3\beta_4$ loop, which is variable among the different ADAMTS members (Supplementary **Fig. 1**), covers part of the active site cleft in the crystal structures of ADAMTS-1, -4 and -5. Mutagenesis data support a direct role of the $\beta_3\beta_4$ loop in ADAMTS-13 substrate recognition [20]. A conserved calcium-binding site located immediately adjacent to the $\beta_3\beta_4$ loop (**Supplementary Fig. S1)** was also demonstrated to be critical for ADAMTS-13 activity [21]. Calcium coordination by Asp182 and Glu212 imposes restraints on the conformation of the $\beta_3\beta_4$ loop that preclude its interaction with Tyr1605 in binding mode A. This binding mode therefore does not provide an obvious explanation for the essential role of the $\beta_3\beta_4$ loop. Strikingly, the Tyr1605 side chain is engaged in stable interactions with Val195, Leu185 and Val192 of the $\beta_3\beta_4$ loop throughout molecular dynamics simulations starting from binding mode B (**Fig. 4B**). In addition, the polar hydroxyl substituent is able to hydrogen bond with Gln191 located in the same $\beta_3\beta_4$ loop. In contrast, during simulations starting from mode A the Tyr1605 side chain conformation is poorly restrained,

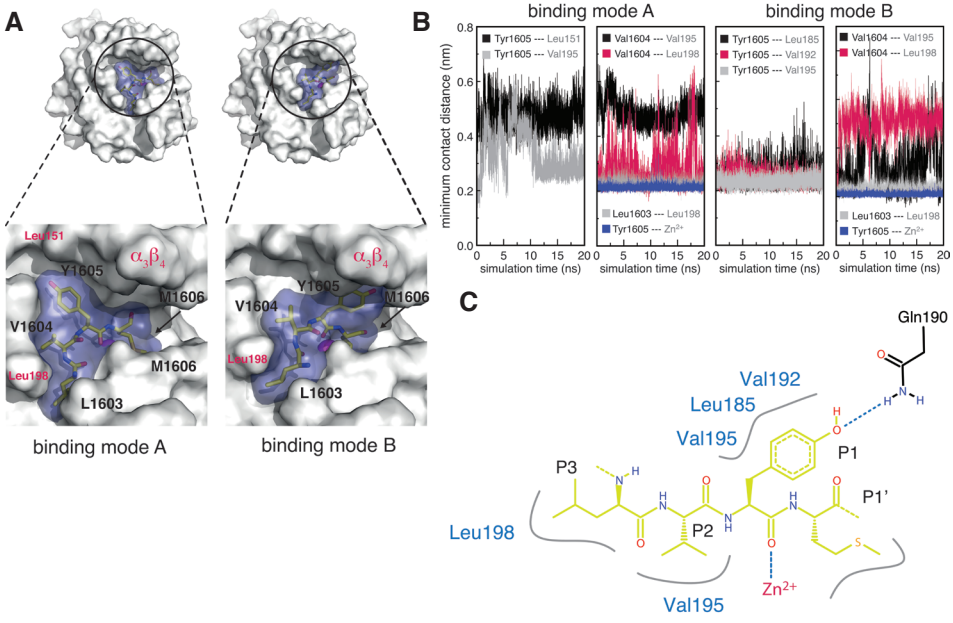

Fig. 4 Modeling substrate binding at the active site. (A) Putative binding modes of residues Leu1603-Met1606. The ADAMTS-13 metalloprotease domain is shown in surface representation (gray). VWF residues Leu1603-Met1606 are shown in stick representation and the corresponding van der Waals surface is shown in blue. (B) Minimum contact distances between putative interacting residues during representative molecular dynamics trajectories. (C) Interaction map of residues involved in recognition of VWF at the ADAMTS-13 active site as derived from molecular simulations.

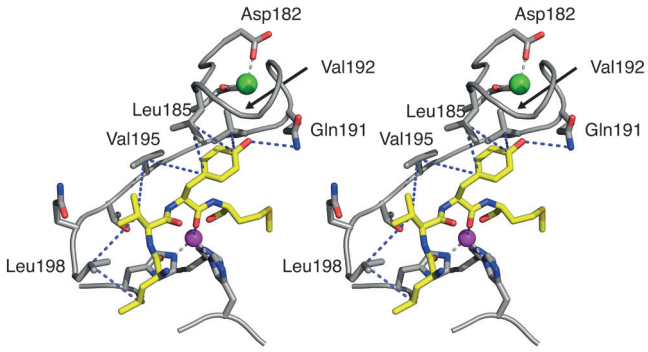

Fig. 5 Substrate interactions with the metalloprotease domain. Cross-eyed stereo view of interactions formed between the metalloprotease domain of ADAMTS-13 and the Leu1603-Met1606 substrate in binding mode B. Non-covalent interactions formed between metalloprotease domain (gray) and substrate (yellow) are indicated with blue dotted lines. The calcium ion restraining the conformation of the $\beta_3\beta_4$ loop via coordination by Asp182 and Glu212 is shown as green spehere. The active site zinc ion is shown in magenta; the coordinating active site histidines are also shown. Note the hydrogen bond between the phenolic hydroxyl substituent of Tyr1605 and Gln191 in the $\beta_3\beta_4$ loop.

a situation not likely to favor catalysis. Further support for the relevance of binding mode B comes from the marked preference of the S1 pocket for aliphatic and aromatic substrates, which is consistent with the solvent inaccessible nature of the S1 pocket in mode B, but not with partial solvent exposure of the P1 residue as is the case in mode A. Moreover, conformational confinement of Tyr1605 by interactions with the $\beta_3\beta_4$ loop (Supplementary **Fig. 2A**) fits the requirement for firm positioning of the scissile bond suggested by the strong effect on k_{cat} of variants at this position.

Whereas these considerations suggest binding mode B to be more realistic, this view is challenged by a recent study, where, on the basis of mutagenesis data, it was proposed that Tyr1605 interacts with ADAMTS-13 residues Val195 and Leu151 [22], an interaction network that would require a conformation of the P1 residue resembling binding mode A. Close inspection of our model shows, however, that even in this case only weak interaction would be possible between Tyr1605 and Leu151, which due to the restraints resulting from Zn^{2+} coordination by the scissile bond carbonyl would involve a strained conformation of Tyr1605. In addition, during molecular dynamics simulations, Tyr1605 does not interact with Leu151 throughout the 20 ns trajectories, and, if enforced in the starting configuration, such contacts are broken instantly (Figure 4B). On the basis of this data we like to propose a purely structural role for Leu151 of ADAMTS-13. This view is supported by (i) strict conservation of Leu151 in all human ADAMTS metalloprotease domains (Supplementary **Fig. 1**) and (ii) the involvement of Leu151 in extensive hydrophobic contacts with conserved isoleucine or valine residues as observed in all crystal structures of ADAMTS metalloprotease domains [32-36]. Together, these findings lead us to suggest that the experimentally observed decrease in cleavage efficiency for the Leu151Ala mutation in ADAMTS-13 [22] is likely caused by conformational changes in the catalytic domain rather than loss of specific interaction with Tyr1605 in VWF.

On the basis of our bioinformatics analysis, mutagenesis data and molecular dynamics simulations we therefore propose a putative interaction map of VWF residues P3-P1' that is based on mode B of our docking models (**Fig. 4C,Fig. 5**). Our model currently precludes analysis of specific interactions formed between the P1' residue Met1606 and ADAMTS-13, since the vicinity of the adjacent disintegrin domain, which is absent in our models, may participate in or affect the conformation of elements forming the S1' pocket. Our putative model of substrate binding is consistent with experimental data suggesting that the P2 residue Val1604 does not contribute directly to substrate binding. In our model, the side chain of Val1604 is largely solvent-exposed (**Fig. 4A**), consistent with our observation that polar residues at position P2 are also cleaved efficiently. In spite of the broad substrate tolerance at the S2 site, the existence of infrequent contacts between Val1604 and Val195 in the ADAMTS-13 metalloprotease domain (**Fig. 4B**) is in agreement with our observation that substrates with large hydrophobic residues at position P2 are cleaved most efficiently (see **Fig. 2A,C**). In accordance with the requirement for aliphatic residues at P3, highly stable interactions are formed between Leu1603 and Leu198 in ADAMTS-13 (**Fig. 4B**), the relevance of which is supported by mutagenesis studies with ADAMTS-13 variants [20].

To debar potential bias during manual model building in hindsight, we used the HADDOCK webserver [38] to predict minimum energy binding poses by docking a clustered molecular dynamics ensemble of the Leu1603-Met1606 substrate peptide (**Supplementary Fig. S2**) against the 10 best MODELLER structures of the ADAMTS-13 metalloprotease domain. By using only the distance of the Tyr1605 carbonyl oxygen to the active site Zn^{2+} ion as an unambiguous restraint and defining solvent-accessible apolar residues located within a radius of 10 Å of the Zn^{2+} ion as passive residues, we obtain structures in the best scoring cluster that are very similar to our manually built model B (Supplementary **Fig. 2C,D**). Importantly, all stable interactions observed in our molecular simulations are also present in the HADDOCK models.

Natural sequence variants affect calcium binding and stability of the VWF-A2 domain

The A2 domain binds calcium with its $\alpha_3\beta_4$ loop (**Fig. 1B**) [10] in the immediate vicinity of the scissile bond. Intriguingly, several natural sequence variants affect residues that flank the metal coordinating residue Asn1602 (**Fig. 1B**). The variants Leu1603Pro and Val1604Phe are implicated in type 2A VWD [39-41], whereas the Pro1601Thr variant has been reported to decelerate cleavage of VWF [26]. ADAMTS-13 requires calcium for optimal activity, but the presence of calcium also renders the native A2 domain resistant to ADAMTS-13 proteolysis in cleavage assays [10]. To analyze the effect of these variants on ADAMTS-13 cleavage, we therefore first investigated sequence-specific proteolytic activity toward variants of the unstructured hGH-VWF73 substrate that does not bind calcium (**Fig. 6A-C**) and subsequently assessed to what extent the variants affect calcium binding, domain stability and ADAMTS-13 cleavage in the context of the native A2 domain (**Fig. 6D-F**).

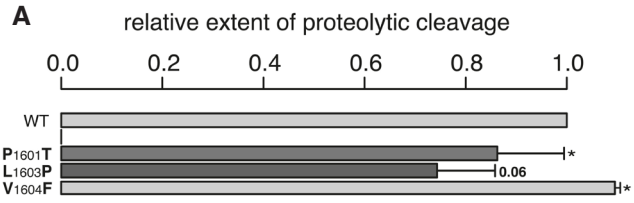

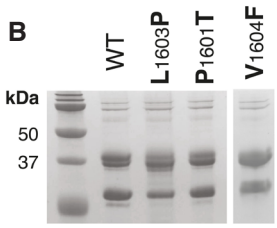

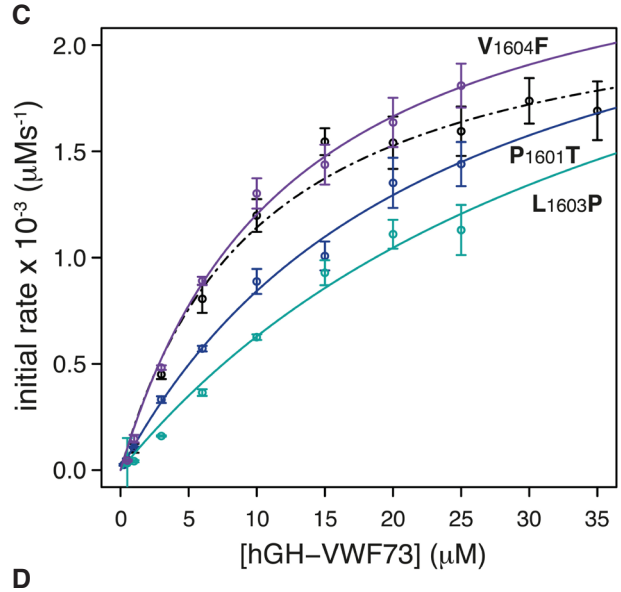

D

	K_M (μM)	k_{cat} (s^{-1})	k_{cat}/K_M (10^4 x $M^{-1}s^{-1}$)	Efficiency index*
WT	10.2 ± 1.8	1.2 ± 0.08	12.0 ± 0.2	-
P1601T	23.0 ± 4.1	1.1 ± 0.12	4.8 ± 0.2	0.40
L1603P	39.0 ± 5.1	1.4 ± 0.44	4.1 ± 0.2	0.34
V1604F	12.4 ± 1.8	1.4 ± 0.09	11.2 ± 0.1	1.07

Fig. 6 Variants with naturally occurring sequence variations affect ADAMTS-13 cleavage efficiency. (A) Representative Coomassie-stained SDS-PAGE gels of ADAMTS-13 cleavage reactions. (B) Bar diagrams of cleavage levels after 60 min as quantified by densitometry. Average cleavage efficiencies from three independent experiments are expressed as relative cleavage levels with respect to the wt-VWF73 sequence. Error bars represent s.d. Asteriks indicate significance levels from a two-tailed t test with $P < 0.05$ (*). (C) Determination of catalytic constants for Pro1601Thr, Leu1603Pro and Val1604Phe variants from cleavage at different substrate concentrations. Product formation after 15 min was quantified by densitometry as the ratio of cleaved and un-cleaved substrate. Error bars report s.d. (n=3). Lines are non-linear fits of the Michaelis-Menten equation to the experimental data. (D) Tabulated catalytic constants. Efficiency index reports the k_{cat}/K_M ratio between variant and WT.

The single nucleotide polymorphism C/T4801 leading to the Pro1601Thr variant has been reported to result in decelerated cleavage of VWF multimers and of the unstructured VWF115 fragment comprising VWF residues 1554-1668 that is similar to our hGH-VWF73 construct [26]. Consistent with these observations, we find a specificity constant k_{cat}/K_M of $4.8*10^4$ $M^{-1}s^{-1}$, which is ~2.5 fold decreased compared to wild-type hGH-VWF73 (Table 1). Our data thus confirm the moderate reduction in cleavage efficiency observed previously for the Pro1601Thr variant [23]. The Leu1603Pro variant, in spite of causing type 2A VWD also displayed somewhat reduced cleavage (**Fig. 4A-C**). The observation that cleavage is only moderately decreased (k_{cat}/K_M of $4.1*10^4$ $M^{-1}s^{-1}$) agrees well with the preference for aliphatic residues at the P3 position. At the same time reduced cleavage suggests that

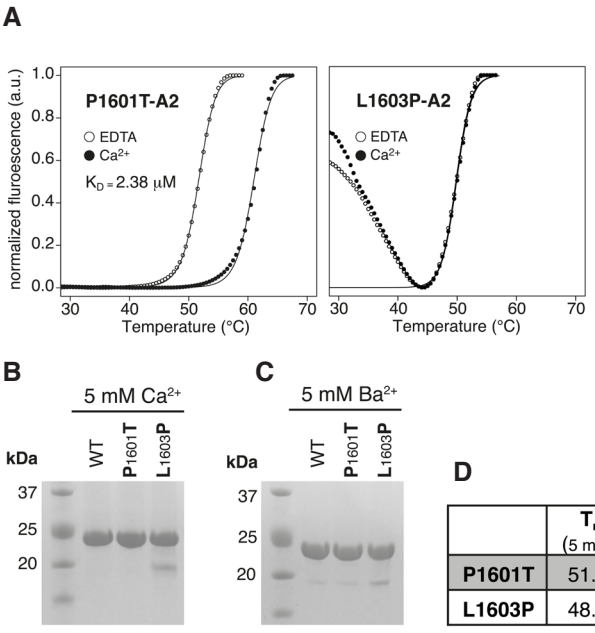

Fig. 7 Pro1601Thr and Leu-1603Pro variants affect calcium binding and stability of VWF-A2. Thermal stability assays with Pro1601Thr and Leu-1603Pro variants of VWF-A2. (A) Representative unfolding curves in the presence of or 5 mM EDTA (open circles) or 5 mM $CaCl_2$ (closed circles) are shown. Solid lines are non-linear regression fits to the experimental data. Errors reported for apparent K_D are s.d. (n=6). (B,C) Representative Coomassie-stained SDS-PAGE gels after ADAMTS-13 cleavage of VWF-A2 variants in buffer containing 5 mM $CaCl_2$ (B) or 5 mM $BaCl_2$ (C).

D

	T_m [°C] (5 mM EDTA)	T_m [°C] (5mM $CaCl_2$)	K_D [μM]
P1601T	51.7 ± 0.1	60.9 ± 0.1	2.4 ± 0.1
L1603P	48.2 ± 0.1	48.0 ± 0.1	-

the type 2A VWD phenotype of the Leu1603Pro variant must be the result of increased exposure of the scissile bond through destabilization of the A2 domain. Interestingly, the Val1604Phe variant, which is also implicated in type 2A VWD was cleaved slightly more efficiently than the wild-type sequence (Fig 6A-C) and kinetic analysis demonstrates that it has a marginally increased k_{cat} (1.4 s^{-1}) and a similar apparent K_M (12.4±1.8 μM) compared to the wild-type sequence. It seems unlikely, however, that such a modest increase in cleavage efficiency would be sufficient to explain the observed 2A VWD phenotype.

We next investigated whether these variants affect calcium binding, thermal stability and susceptibility to ADAMTS-13 cleavage in native A2. To this end, we expressed Pro1601Thr, Leu1603Pro and V1604Phe single-point mutants of the full-length, glycosylated A2 (residues 1478-1674) and analyzed stability of these variants in the absence and the presence of calcium by monitoring temperature-dependent protein unfolding with a fluorescent dye. Consistent with the apparent lack of a type 2A VWD phenotype associated with the Pro1601Thr mutation, thermal stability of this variant in the presence of 5 mM EDTA or 5 mM $CaCl_2$ is similar to wild-type A2 (**Fig. 7A**). The significant shift in melting temperature upon addition of calcium (ΔT_m = 9.2±0.1°C; **Fig. 7A,D**) clearly demonstrates that this mutant is still able to bind calcium. We find the dissociation constant for calcium to be 2.4±0.1 μM, about 12-fold higher than the 0.2±0.04 μM determined for wild-type A2 [10]. Thermal stability in the absence of calcium is slightly higher than observed for wild-type A2, possibly because substitution of Pro1601 allows formation of one additional hydrogen bond in strand β_4.

Our cleavage data obtained with the hGH-VWF73 Leu1603Pro variant suggested that

the type 2A VWD phenotype of this variant must be a consequence of reduced stability of the A2 domain. When expressing the Leu1603Pro variant in the context of full-length VWF-A2 we observed a significantly reduced level of expressed protein compared to wild-type VWF-A2 or the Pro1601Thr construct, which suggests that this variant is less stable. Partial protein misfolding is also suggested by a high fluorescence signal observed prior to the unfolding transition in thermal stability assays (**Fig. 7A**), which typically results from dye binding to exposed hydrophobic residues at the start of the experiment. In spite of the background signal, we do observe a clear unfolding transition. The T_m of this transition in the presence and absence of calcium (**Fig. 7D**) is similar and close to that observed for wt-A2 in the absence of calcium [10], strongly suggesting that this variant has lost the ability to bind calcium.

The Val1604Phe mutant of the full-length A2 domain could not be expressed in HEK-E cells. Inspection of the crystal structure of the A2 domain [10] reveals that substitution with phenylalanine at Val1604 leads to severe steric conflicts and our data thus suggest that the type 2A VWD phenotype associated with this variant is the consequence primarily of structural de-stabilization of the A2 domain rather than the slight increase in cleavage efficiency for Val1604Phe that we observed in our cleavage assays (see **Fig. 2A,C**).

Finally, we investigated the effect of the Pro1601Thr and Leu1603Pro variants on ADAMTS-13 cleavage in the context of the full-length, folded A2 domain. Consistent with our thermal stability data we observe that wt-A2 and Pro1601Thr-A2 are resistant to proteolysis in buffer conditions containing calcium, whereas Leu1603Pro-A2 is cleaved under these conditions (**Fig. 7B**). It has been established that substitution of calcium with barium in ADAMTS-13 proteolysis assays abrogates the stabilizing effect that calcium binding confers on A2, while at the same time preserving full activity of ADAMTS-13 [10]. Under these conditions, cleavage of both wt-A2 and Pro1601Thr-A2 can now be observed (**Fig. 7C**). Importantly, the extent of cleavage for Leu1603Pro-A2 remains unchanged compared to that in conditions containing calcium (**Fig. 7C**), confirming its decreased stability is due to the inability to bind calcium. The cleavage data thus parallel our thermal stability analysis in demonstrating that stability of the Leu1603Pro variant is unaffected by the presence of calcium.

Discussion

Cleavage of VWF by ADAMTS-13 requires unfolding of the A2 domain, which in the physiological situation is achieved by hydrodynamic shear forces acting on VWF multimers. Once unfolded, A2 exposes a number of interaction sites in its carboxyl-terminal sequence, which bind to exosites in the non-catalytic domains of ADAMTS-13 [11,12]. Partial VWF substrates that do not adopt a stable native fold have proven particularly useful in studying such interactions under static conditions, since they enable separation of effects related to the substrate conformation from substrate binding and proteolysis – both of which could affect cleavage efficiency. Most efforts have previously been directed at mapping and characterizing interaction sites located at a considerable distance from the cleavage site and these sequences seem to contribute most of the affinity and general specificity for

the VWF substrate [11,12,14]. These interaction sites appear to operate cooperatively in facilitating the approach and positioning of the P1-P1' peptide bond at the catalytic Zn^{2+} ion in the metalloprotease domain of ADAMTS-13 [11]. However, substrate residues flanking the scissile bond often are a major determinant in substrate selectivity of proteases. Building on evidence from deletion constructs [12], we and others have recently demonstrated that Leu1603 and Val1604, which are located amino-terminal to the scissile bond are also important for cleavage [10,22]. The large set of P2 variants investigated in the present study now demonstrates that Val1604 does not itself contribute specific interactions to substrate recognition, but rather suggests that it imposes restraints on the main chain conformation and thereby positions the principal specificity elements Leu1603 (P3) and Tyr1605 (P1). Interestingly, we find that the substrate tolerance at P1 is far narrower than that at P1'. Hence, ADAMTS-13 - similar to ADAMTS-4 [42,43] - appears to differ from the related MMPs, for which P1' is generally assumed to be the main determinant of substrate selectivity [30]. Similarly, structural flexibility of the S1' pocket has also been observed for inhibitor binding by ADAMTS-5 [32], suggesting that broad specificity at this site may be a general property of the ADAMTS family.

Substrate specificity in general can arise from differences in binding affinity (as expressed by the Michaelis-Menten constant K_M), or from differences in the catalytic rate constant (k_{cat}), which is related to 'productive binding', i.e. the ability of the substrate to adopt a particular geometry at the active site that lowers the activation free energy of the enzymatic reaction. Catalytic parameters of hGH-VWF73 cleavage suggest that it is primarily Leu1603 at P3 that determines substrate binding affinity. In contrast, substitutions at P1 and P1' appear to have little effect on binding, but strongly affect the catalytic rate constant k_{cat} (see **Fig. 3A,B**). Apparently, firm binding is therefore brought about by amino-terminal anchoring at the S3 subsite, whereas selectivity at substrate positions P1 and P1' appears to be primarily related to the ability of the scissile peptide bond to adopt the appropriate geometry for maximum catalytic activity. This view is supported by the observation that the substitution of Tyr1605 and Met1606 with smaller residues impedes cleavage by severely reducing turnover rates, whereas variants with sterically demanding residues at these positions are cleaved efficiently [26]. Our simulations lend further support to this hypothesis in demonstrating the importance of non-polar interactions between the $\beta_3\beta_4$ loop of ADAMTS-13 and Tyr1605 for the confinement of Tyr1605 (see **Fig. 4B**, and **Supplementary Fig. S2**), which may be an important factor in productive positioning of the scissile bond. It is of importance to note that all data presented in this study are based on static assays and equilibrium simulations. It will therefore be interesting to investigate to what extent the conformational restraints observed for positioning of the scissile residues are modulated in the physiologically more relevant scenario, in which the substrate peptide chain is subject to tensile forces.

Shear-induced exposure of exosite-binding sequences and the scissile bond appear to be modulated by physiological calcium concentrations. Specifically, we have shown that calcium binding restricts accessibility of the scissile bond by increasing the force required for A2 unfolding and promoting refolding into its native conformation [10]. So

far, no naturally occurring mutations have been reported for any of the residues directly involved in calcium binding. The side chain of P4 residue Asn1602 contributes one of the coordinating ligands for calcium binding by A2. Although located in close proximity to the scissile bond, this residue is not directly involved in substrate recognition by ADAMTS-13 [10,22]. Intriguingly however, sequence variations exist for both of the adjacent residues Pro1601 and Leu1603 [26,39,41]. We observe that ADAMTS-13 cleaves both Pro1601Thr and Leu1603Pro variants of our hGH fusion substrates less efficiently than wild type hGH-VWF73. The Pro1601Thr variant, when introduced into the context of the full-length A2 domain, shows comparable behavior in thermal stability and ADAMTS-13 cleavage assays as the wt-A2 domain. Although this variant binds calcium less tightly than wt-A2, the micromolar affinity implies that the calcium-binding site is saturated in vivo. These observations are consistent with the absence of a type 2A VWD phenotype associated with the Pro1601Thr variant. The Leu1603Pro mutation, in contrast, does cause type 2A VWD [39,41]. The Leu1603Pro variant of the hGH-VWF73 construct is cleaved less efficiently by ADAMTS-13 and to explain the type 2A VWD disease phenotype this mutation therefore must increase susceptibility to cleavage by exposing the scissile bond in the A2 domain. Inspection of the VWF-A2 crystal structure suggests that substitution of Leu1603 with proline would compromise main chain hydrogen bonding of the central β_4 strand and significantly distort the local main chain conformation, which, presumably, could also affect calcium-binding by Asn1602 (see Figure 1C). Indeed, our observation that calcium does not stabilize Leu1603Pro-A2 in thermal stability assays confirms disruption of calcium binding. Interestingly, the unfolding temperature of the Leu1603Pro mutant is similar to that of wild-type A2 without calcium, suggesting that its inability to bind calcium may be the principle cause of the observed type 2A VWD phenotype for the Leu1603Pro variant. The significance of calcium binding for mechanosensory properties of the A2 domain is evident in vitro [10]. Our results suggest that these principles may also be also relevant for the pathogenesis of 2A VWD and provide an interesting starting point to explore their significance in physiologically relevant model systems.

Acknowledgements
We thank Jan Voorberg of Sanquin Research (Amsterdam) for providing recombinant ADAMTS-13 and Adrien Melquiond (Utrecht University) for advice in using HADDOCK.

Funding
This work was supported by ECHO grant 700.55.012 from the Council of Chemical Sciences of the Netherlands Organization for Scientific Research (NWO) to EGH.

Author contributions
Conceived and designed the experiments: AJ EGH. Performed the experiments: AJ. Analyzed the data: AJ EGH. Wrote the manuscript: AJ EGH.

Material and methods

Cloning, Expression and Purification of hGH-VWF73 variants

VWF73 constructs (residues 1596-1668) were PCR amplified from VWF cDNA (pNUT-VWFcass1 [44]). Mutations were introduced in the forward amplification oligonucleotides. Constructs were cloned between the human growth hormone fusion and a carboxyl-terminal $(StrepII)_2$ tag of an mammalian expression vector optimized for transient expression in HEK cells. hGH-VWF73 variants and recombinant VWF-A2 (residues 1478-1674) were expressed in HEK293-EBNA1 cells and purified as described previously [10]. Sequence variants Pro1601Thr and Leu1603Pro of the VWF-A2 domain were generated by Quickchange mutagenesis (Stratagene) and expressed and purified following the same protocol as applied for the wild-type construct.

Thermal stability assays

Thermofluor stability assays were performed essentially as described previously [10]. For the Pro1601Thr variant, the apparent Ca^{2+} dissociation constant (K_D) was determined from the thermal unfolding data in the presence of 5 mM EDTA and various concentrations of $CaCl_2$ according to [45].

ADAMTS-13 cleavage experiments

To determine relative cleavage efficiencies of individual VWF73 substrate variants, 5 µl of 2 nM enzyme (4 nM for Val1604Gly and Val1604Ala) in 25 mM Tris pH 7.5, 150 mM NaCl, 5 mM $CaCl_2$ (TBS-Ca^{2+}) were incubated for 15 min at 37 °C before 5 µl of the individual hGH-VWF73 variants in TBS-Ca^{2+} were added to a final substrate concentration of 6 µM. After 1h at 37 °C reactions were stopped with 5 mM EDTA in SDS sample preparation buffer. Substrate and cleavage products were separated by SDS gel electrophoresis on 15% Tris-Tricine gels. Quantitative analysis of VWF73 proteolysis was performed by densitometry of Coomassie stained gels on a ChemiDocTM MP system (Bio-Rad) using Quantity-One software (BioRad). Average cleavage efficiencies (n=3-6) for individual variants were expressed as relative cleavage levels normalized to proteolysis of the wild-type VWF73 sequence under the same assay conditions. wt-VWF73 loading controls were run on every gel to account for differences in staining efficiency. For determination of individual catalytic constants, initial proteolysis rates v_i (in μMs^{-1}) were determined at varying substrate concentrations and computed from integrated densitometric volumes according to

$$v_i = \frac{\left[\frac{V_N + V_C}{V_{tot}}\right] \times c_i\left(VWF73\right)}{t}$$

where V_N and V_C are the densitometric volumes of amino- and carboxyl-terminal cleavage products, respectively, and V_{tot} is the integrated volume of cleavage products and uncleaved substrate. V_{max} and K_M were derived from non-linear least squares fit of the Michaelis-Menten equation to the data, when these rates were plotted against substrate concentration. Cleavage assays for wt-A2, Pro1601Thr and Leu1603Pro-A2 in the presence of calcium and barium were performed as described previously [10].

Homology modeling and molecular dynamics

Homology modeling of the ADAMTS-13 metalloprotease domain was performed with MODELLER-9v7 [46], based on a MUSCLE multiple sequence alignment of human ADAMTS metalloprotease domains and using the high-resolution crystal structure of ADAMTS-5 metalloprotease domain (PDB ID 3b8z) as the template structure. ADAMTS-13 models were ranked according to the DOPE statistical potential score. The best ranking model was used for subsequent substrate docking and molecular simulations. The catalytic Zn^{2+} ion was added to the model based on superposition with PDB ID 3b8z, and three Ca^{2+} ions were included at the corresponding sites identified in other structurally characterized ADAMTS metalloprotease domains. The substrate peptide (Leu1603-Met1606) was modeled into the active site by manual model building in Coot [47]. GROMACS 4.5.2 [48] was employed for molecular simulations and analysis of trajectories. Distances between the zinc ion and coordinating histidine residues were restrained to the reference values [39] by harmonic potentials (1500 $kJmol^{-1}nm^{-2}$). Geometry-optimized structures were solvated in TIP4P in cubic boxes with a minimum distance of 10 Å between solute and box edge. Sodium and chloride ions were added to neutralize the system and establish an ionic strength of 150 mM. The OPLS-AA all-atom force field [49] was used during geometry optimization, solvent equilibration (250 ps) and acquisition phase molecular simulations (n=3; 25 ns), applying a 10 Å cutoff for van der Waals interactions. Harmonic restraints on main chain atoms were removed during the acquisition phase simulations. Time ranges from 0-5 ns of the acquisition runs were omitted during analysis.

References

1. Federici AB, Bader R, Pagani S, Colibretti ML, De Marco L, et al. (1989) Binding of von Willebrand factor to glycoproteins Ib and IIb/IIIa complex: affinity is related to multimeric size. *Br J Haematol* **73**: 93–99.
2. Moake JL, Turner NA, Stathopoulos NA, Nolasco LH, Hellums JD (1986) Involvement of large plasma von Willebrand factor (vWF) multimers and unusually large vWF forms derived from endothelial cells in shear stress-induced platelet aggregation. *J Clin Invest* **78**: 1456–1461.
3. Tsai H (1996) Physiologic cleavage of von Willebrand factor by a plasma protease is dependent on its conformation and requires calcium ion. *Blood* **87**: 4235-4244.
4. Furlan M, Robles R, Lämmle B (1996) Partial purification and characterization of a protease from human plasma cleaving von Willebrand factor to fragments produced by in vivo proteolysis. *Blood* **87**: 4223–4234.
5. Furlan M, Robles R, Galbusera M, Remuzzi G, Kyrle PA, et al. (1998) von Willebrand factor-cleaving protease in thrombotic thrombocytopenic purpura and the hemolytic-uremic syndrome. *N Engl J Med* **339**: 1578–1584.
6. Zheng X, Sadler J (2008) Pathogenesis of Thrombotic Microangiopathies. *Annu Rev Pathol* **3**: 249–277
7. Sadler JE (2002) A new name in thrombosis, ADAMTS13. *Proc Natl Acad Sci USA* **99**: 11552-11554.
8. Sadler JE (2005) New concepts in von Willebrand disease. *Annu Rev Med* **56**: 173–191.
9. Tsai H, Sussman I, Nagel R (1994) Shear stress enhances the proteolysis of von Willebrand factor in normal plasma. *Blood* **83**: 2171.
10. Jakobi AJ, Mashaghi A, Tans SJ, Huizinga EG (2011) Calcium modulates force sensing by the von Willebrand factor A2 domain. *Nature Communications* **2**: 385
11. Gao W, Anderson PJ, Majerus EM, Tuley EA, Sadler JE (2006) Exosite interactions contribute to tension-induced cleavage of von Willebrand factor by the antithrombotic ADAMTS13 metalloprotease. *Proc Natl Acad Sci USA* **103**: 19099–19104.
12. Gao W, Anderson P, Sadler J (2008) Extensive contacts between ADAMTS13 exosites and von Willebrand factor domain A2 contribute to substrate specificity. *Blood* **112**: 1713–9.
13. Feys HB, Anderson PJ, Vanhoorelbeke K, Majerus EM, Sadler JE (2009) Multi-step binding of ADAMTS-13 to von Willebrand factor. *J Thromb Haemost* **7**: 2088–2095.
14. De Groot R, Bardhan A, Ramroop N, Lane D, Crawley J (2009) Essential role of the disintegrin-like domain in ADAMTS13 function. *Blood* **113**: 5609–5616.
15. Zhang P, Pan W, Rux AH, Sachais BS, Zheng XL (2007) The cooperative activity between the carboxyl-terminal TSP1 repeats and the CUB domains of ADAMTS13 is crucial for recognition of von Willebrand factor under flow. *Blood* **110**: 1887–1894.
16. Tao Z, Wang Y, Choi H, Bernardo A, Nishio K, et al. (2005) Cleavage of ultralarge multimers of von Willebrand factor by C-terminal-truncated mutants of ADAMTS-13 under flow. *Blood* **106**: 141–143.
17. Ai J, Smith P, Wang S, Zhang P, Zheng XL (2005) The proximal carboxyl-terminal domains of ADAMTS13 determine substrate specificity and are all required for cleavage of von Willebrand factor. *J Biol Chem* **280**: 29428–29434.
18. Majerus EM, Anderson PJ, Sadler JE (2005) Binding of ADAMTS13 to von Willebrand factor. *J Biol Chem* **280**: 21773–21778.
19. Soejima K, Matsumoto M, Kokame K, Yagi H, Ishizashi H, et al. (2003) ADAMTS-13 cysteine-rich/spacer domains are functionally essential for von Willebrand factor cleavage. *Blood* **102**: 3232–3237.
20. De Groot R, Lane DA, Crawley JTB (2010) The ADAMTS13 metalloprotease domain: roles of subsites in enzyme activity and specificity. *Blood* **116**: 3064–3072.
21. Gardner M, Chion C, De Groot R, Shah A, Crawley J, et al. (2009) A functional calcium-binding site in the metalloprotease domain of ADAMTS13. *Blood* **113**: 1149.
22. Xiang Y, De Groot R, Crawley JTB, Lane DA (2011) Mechanism of von Willebrand factor scissile bond cleavage by a disintegrin and metalloproteinase with a thrombospondin type 1 motif, member 13 (ADAMTS13) *Proc Natl Acad Sci USA* **108**: 11602–11607.
23. Zanardelli S, Crawley JTB, Chion CKNCK, Lam JK, Preston RJS, et al. (2006) ADAMTS13 substrate recognition of von Willebrand factor A2 domain. *J Biol Chem* **281**: 1555–1563.
24. Anderson PJ, Kokame K, Sadler JE (2006) Zinc and calcium ions cooperatively modulate ADAMTS13 activity. *J Biol Chem* **281**: 850–857.
25. Zanardelli S, Chion ACK, Groot E, Lenting PJ, McKinnon TAJ, et al. (2009) A novel binding site for ADAMTS13 constitutively exposed on the surface of globular VWF. *Blood* **114**: 2819–2828.
26. Pruss CM, Notley CRP, Hegadorn CA, O'Brien LA, Lillicrap D (2008) ADAMTS13 cleavage efficiency is altered by mutagenic and, to a lesser extent, polymorphic sequence changes in the A1 and A2 domains of von Willebrand factor. *Br J Haematol* **143**: 552–558. .
27. Chakrabarti P, Pal D (2001) The interrelationships of side-chain and main-chain conformations in proteins. *Prog Biophys Mol Biol* **76**: 1–102.
28. Deane CM, Allen FH, Taylor R, Blundell TL (1999) Carbonyl-carbonyl interactions stabilize the partially allowed Ramachandran conformations of asparagine and aspartic acid. *Protein Eng* **12**: 1025–1028.
29. Manzetti S, Mcculloch DR, Herington AC, Van Der Spoel D (2003) Modeling of enzyme–substrate complexes for the metalloproteases MMP-3, ADAM-9 and ADAM-10. *J Comput Aided Mol Des* **17**: 551–565.

30. Tallant C, Marrero A, Gomis-Rüth FX (2010) Matrix metalloproteinases: fold and function of their catalytic domains. *Biochim Biophys Acta* **1803**: 20–28.

31. Jones GC, Riley GP (2005) ADAMTS proteinases: a multi-domain, multi-functional family with roles in extracellular matrix turnover and arthritis. *Arthritis Res Ther* **7**: 160–169.

32. Shieh H-S, Tomasselli AG, Mathis KJ, Schnute ME, Woodard SS, et al. (2011) Structure analysis reveals the flexibility of the ADAMTS-5 active site. *Protein Science* **20**: 735–744.

33. Gerhardt S, Hassall G, Hawtin P, McCall E, Flavell L, et al. (2007) Crystal structures of human ADAMTS-1 reveal a conserved catalytic domain and a disintegrin-like domain with a fold homologous to cysteine-rich domains. *J Mol Biol* **373**: 891–902.

34. Shieh H-S, Mathis KJ, Williams JM, Hills RL, Wiese JF, et al. (2008) High resolution crystal structure of the catalytic domain of ADAMTS-5 (aggrecanase-2). *J Biol Chem* **283**: 1501–1507.

35. Tortorella MD, Tomasselli AG, Mathis KJ, Schnute ME, Woodard SS, et al. (2009) Structural and inhibition analysis reveals the mechanism of selectivity of a series of aggrecanase inhibitors. *J Biol Chem* **284**: 24185-91

36. Mosyak L, Georgiadis K, Shane T, Svenson K, Hebert T, et al. (2008) Crystal structures of the two major aggrecan degrading enzymes, ADAMTS4 and ADAMTS5. *Protein Sci* **17**: 16–21.

37. Akiyama M, Takeda S, Kokame K, Takagi J, Miyata T (2009) Crystal structures of the noncatalytic domains of ADAMTS13 reveal multiple discontinuous exosites for von Willebrand factor. *Proc Natl Acad Sci USA* **106**: 19274–19279.

38. de Vries SJ, van Dijk M, Bonvin AMJJ (2010) The HADDOCK web server for data-driven biomolecular docking. *Nature Protocols* **5**: 883–897.

39. Enayat M, Guilliatt A, Bradbury M, Tait R, Williams M, et al. (2006) Five novel candidate mutations in type 2A, 2M and 2N von Willebrand disease patients from the west of Scotland. *Br J Haematol* **133**: 41.

40. Meyer D, Fressinaud E, Gaucher C, Lavergne JM, Hilbert L, et al. (1997) Gene defects in 150 unrelated French cases with type 2 von Willebrand disease: from the patient to the gene. INSERM Network on Molecular Abnormalities in von Willebrand Disease. *Thromb Haemost* **78**: 451–456.

41. Berber E, Pehlevan F, Akin M, Yalcin Capan O, Kavakli K, et al. (2012) A Common VWF Exon 28 Haplotype in the Turkish Population. *Clin Appl Thromb Hemost* [Epub ahead of print]

42. Tortorella M, Pratta M, Liu RQ, Abbaszade I, Ross H, et al. (2000) The thrombospondin motif of aggrecanase-1 (ADAMTS-4) is critical for aggrecan substrate recognition and cleavage. *J Biol Chem* **275**: 25791-25797.

43. Kashiwagi M, Enghild JJ, Gendron C, Hughes C, Caterson B, et al. (2004) Altered proteolytic activities of ADAMTS-4 expressed by C-terminal processing. *J Biol Chem* **279**: 10109–10119.

44. Lankhof H, Wu YP, Vink T, Schiphorst ME, Zerwes HG, et al. (1995) Role of the glycoprotein Ib-binding A1 repeat and the RGD sequence in platelet adhesion to human recombinant von Willebrand factor. *Blood* **86**: 1035–1042.

45. Lo M-C, Aulabaugh A, Jin G, Cowling R, Bard J, et al. (2004) Evaluation of fluorescence-based thermal shift assays for hit identification in drug discovery. *Anal Biochem* **332**: 153–159.

46. Eswar N, Eramian D, Webb B, Shen M-Y, Sali A (2008) Protein structure modeling with MODELLER. *Methods Mol Biol* **426**: 145–159.

47. Emsley P, Cowtan K (2004) Coot: model-building tools for molecular graphics. A*cta Crystallogr D Biol Crystallogr* **60**: 2126–2132.

48. Hess B, Kutzner C, Van Der Spoel D, Lindahl E (2008) GROMACS 4: Algorithms for highly efficient, load-balanced, and scalable molecular simulation. J Chem Theory Comput 4: 435–447

49. Jorgensen W, Tirado-Rives J (1988) The OPLS potential functions for proteins. Energy minimizations for crystals of cyclic peptides and crambin. *J Am Chem Soc* **110**: 1657–1666.

Supplementary Fig. S1

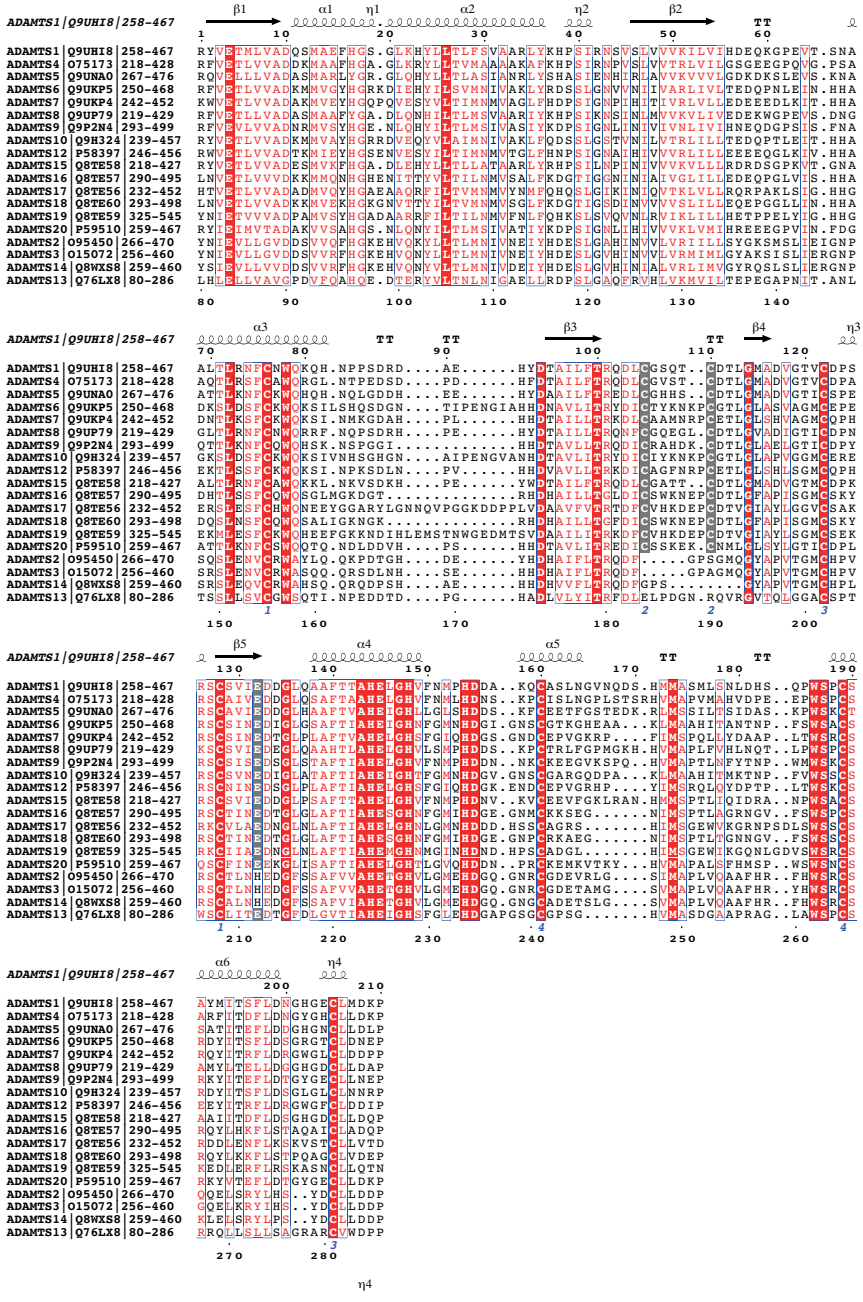

Supplementary Fig. S1 Multiple sequence alignment of the human ADAMTS family. The official residue numbering of ADAMS-13 (Uniprot accession Q76LX8) is shown at the bottom of each block.The cysteine bridge in the $\beta_3\beta_4$ loop (gray boxes) is absent is ADAMTS-2,-3,-13,-14. Note the high variability among the $\beta_3\beta_4$ loop regions. Leu151 and the calcium-coordinating Asp182 and Glu212 are strongly conserved.

Supplementary Fig. S2

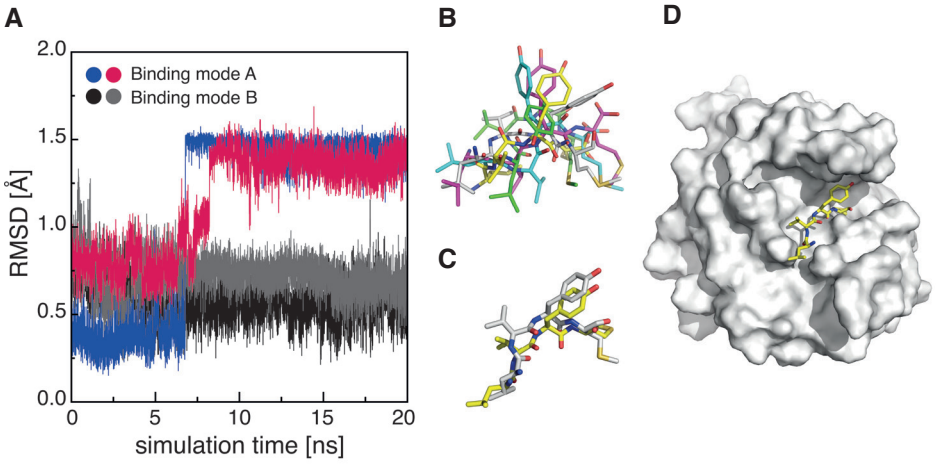

Supplementary Fig. S2 Confinement of Tyr1605 by the $\beta_3\beta_4$ loop and HADDOCK results. (A) RMSD of Tyr1605 in trajectories of binding mode A and B. Note that Tyr1605 is spatially confined only in binding mode B. (B) Clustered molecular dynamics ensemble of the Leu1603-Met1606 substrate peptide used for docking with HADDOCK. (C) Substrate conformations of binding modes from manual model building (gray) and highest scoring cluster representative from HADDOCK (yellow) after superimposition of the metalloprotease domains. (D) Substrate binding mode of the HADDOCK model in the highest scoring cluster. Comparison with Fig. 4A demonstrates that the HADDOCK mode and substrate binding mode B from manual model building are very similar.

CHAPTER 4

A rapid cloning method employing orthogonal end protection

Arjen J. Jakobi and Eric G. Huizinga
Crystal & Structural Chemistry, Bijvoet Center for Biomolecular Research, Department of Chemistry, Utrecht University, Padualaan 8, 3584 CH Utrecht, The Netherlands

PLoS One **7**: e37617 (2012)

We describe a novel in vitro cloning strategy that combines standard tools in molecular biology with a basic protecting group concept to create a versatile framework for the rapid and seamless assembly of modular DNA building blocks into functional open reading frames. Analogous to chemical synthesis strategies, our assembly design yields idempotent composite synthons amenable to iterative and recursive split-and-pool reaction cycles. As an example, we illustrate the simplicity, versatility and efficiency of the approach by constructing an open reading frame composed of tandem arrays of a human fibronectin type III (FNIII) domain and the von Willebrand Factor A2 domain (VWFA2), as well as chimeric $(FNIII)_n$-VWFA2-$(FNIII)_n$ constructs. Although we primarily designed this strategy to accelerate assembly of repetitive constructs for single-molecule force spectroscopy, we anticipate that this approach is equally applicable to the reconstitution and modification of complex modular sequences including structural and functional analysis of multi-domain proteins, synthetic biology or the modular construction of episomal vectors.

The design and construction of DNA sequences by assembly of modular DNA fragments lies at the core of protein engineering. The advent of synthetic biology with associated technological advances in manufacturing of DNA sequences has recently matured *de novo* synthesis of custom genes into an important resource. In spite of these advances, however, there remains a continuous demand for robust and cost-effective alternatives, adaptable by individual laboratories, to aid downstream processing of DNA sequences. This is reflected by the copious and diverse set of elegant tools and strategies that have been developed to facilitate *ad hoc* combinatorial manipulation of DNA sequences and their transfer into episomal vectors by PCR-based [1-4], ligation-based [5-7], or recombination-based methods [8,9]. Among the plethora of available techniques, each has its unique advantages and not all individual assembly requirements can be met by a single strategy. For instance, one difficulty encountered by several applications is the

recurrent seamless integration of DNA modules into serial or tandem arrays. As one such example, single-molecule force spectroscopy frequently employs repeat proteins to facilitate the identification of characteristic mechanical fingerprints in the experimental force-distance data and to accelerate the generation of statistically relevant datasets. However, only a minor fraction of proteins biologically occur in a repetitive context. Artificial repeat constructs (often referred to as "polyproteins") are therefore typically obtained by recombinant expression of engineered constructs in which proteins or protein domains are arranged in tandem arrays [10,11]. At the DNA level, sequential assembly of such constructs by conventional methods typically relies on asymmetric recognition sites for restriction endonucleases [12] or on recycling of restriction sites [2,13]. These methods either lack control over the exact composition of the assembly product or they require multi-fragment cloning and a series of time-consuming subcloning steps [14]. To accelerate the assembly of such constructs, we recognized the need for a simple and robust strategy permitting the modular recombination of DNA fragments *in vitro*. In multi-step chemical synthesis, efficient strategies have been developed to systematically assemble combinations of molecular building blocks into large assortments of diverse compounds. Surprisingly, several core concepts of these strategies have not yet been adapted to the assembly of recombinant DNA sequences, although the prerequisites for the efficient use of such formats are similar. For instance, chemical synthesis strategies frequently employ transient protecting groups that allow modular building blocks (synthons) to be assembled at specific reactive sites in a defined synthetic sequence. This concept is supported by the ability to selectively remove these protecting groups with a set of mutually exclusive (orthogonal) reaction conditions. In the context of DNA engineering, such molecular building blocks can be defined as DNA synthons and reactive sites as mutually compatible, cohesive overhang sequences that permit DNA ligase-mediated assembly reactions. Likewise, protecting groups may represent peripheral sequences that can be selectively eliminated, by for instance specific restriction enzymes, to reveal cohesive overhang sequences. Directional and recurrent recombination strategies for DNA synthons can accordingly be realized by orthogonal de-protection reactions that expose cohesive overhang sequences at opposite ends of the modules. In the course of any such assembly process, the selective de-protection of defined sequences permits pasting together complementary synthons. To our knowledge there has been no reported gene assembly strategy that exploits the concept of protecting groups for *in vitro* assembly of DNA sequences. We here validate applicability of these principles to the assembly of expression cassettes encoding tandem arrays of protein domains for single-molecule force spectroscopy.

Results

General Assembly Strategy

A restriction and ligation-based approach to DNA assembly is introduced that follows the general concept of protecting group-based chemical synthesis strategies. We implement this strategy by designing DNA synthons flanked by protecting groups, which can be selectively removed to expose cohesive overhang sequences. These attributes allow

synthons to enter repeated cycles of selective de-protection and fusion reactions *in vitro*, without requiring subcloning steps. As a key concept of our design, any assembly operation performed on an arbitrary pair of synthons will yield an idempotent composite synthon. That is, product synthons may serve as entry synthons for subsequent assembly steps. The resulting versatility of this *split-and-pool* approach allows sequential, parallel and hierarchical strategies for the assembly of DNA modules to be employed with minimal screening efforts.

Synthon Design

The concept of protecting groups builds on the ability to selectively control the site of modification in a scaffolding synthon, and hence, to precisely define the reaction sequence leading to the final assembly product. For our purpose this requires the introduction of two types of protective groups that can be removed with site-specific (orthogonal) de-protection reactions. Within the framework of DNA assembly this can be readily met by exploiting the excellent specificity of restriction endonucleases towards recognizing and cleaving DNA sequences. In particular, type IIS restriction endonucleases are able to cleave arbitrary sequences at a precise distance from their non-palindromic recognition site and thereby expose user-defined overhang sequences. This unique property of IIS enzymes has the advantage that no artifacts are introduced into the synthons if the recognition site for the enzyme is contained within a flanking sequence that does not become part of the final assembly.

Table 1 Reaction conditions of IIS endonucleases

Endonuclease	Recognition Sequence	NEB buffer	T (°C)
BsaI	**GGTCTC***N/NNNN*	4 or 3	50
BsmBI	**CGTCTC***N/NNNN*	3	55
BsmAI	**GTCTC***N/NNNN*	3	50

The application of IIS endonucleases in DNA assembly is not new, and a number of resourceful strategies have recently emerged [5,7,15,16]. We here attempt to extend these methods by introducing a general protecting group strategy that exploits the unique properties of IIS endonucleases. In our general design, the ends of synthons are flanked by oppositely oriented recognition sites for two different IIS endonucleases (**Fig. 1A**). The choice of the endonuclease used for excision of the synthon from an entry vector determines which end of the synthon is protected and which end is reactive/cohesive. The orthogonal motif, together with appropriately selected overhang sequences, supports unidirectional and site-specific assembly of (composite) modules on either end of the entry synthon (**Fig. 1B**). In our design we have chosen IIS endonucleases with 6 base pair recognition sequences, whose theoretical frequency of occurrence is approximately once in 2048 base pairs ($4^6/2$), depending on the GC content of the donor genome. This is sufficiently rare to allow application of this approach to typical gene fragments; however, prior mutagenesis may occasionally be required to remove internal sites. From the wealth of commercially available IIS endonucleases, we chose BsmBI and BsaI for reasons of robustness and

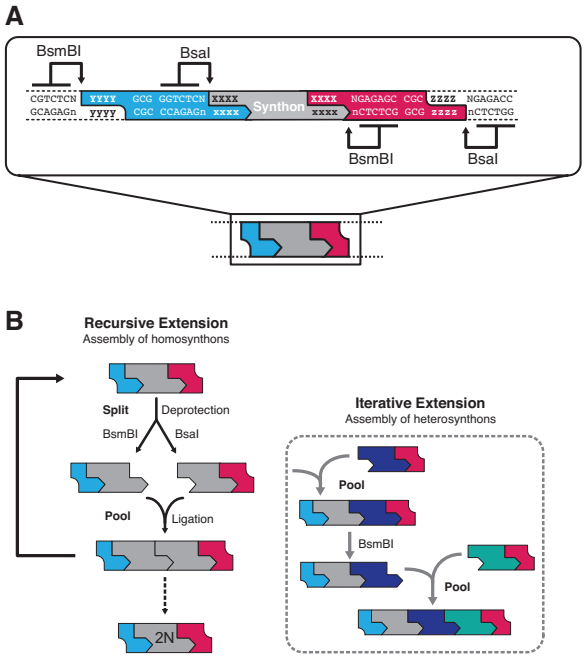

Figure 1 Split-and-pool assembly of DNA synthons (A) Entry synthons are flanked on both sides by recognition sequences for the type IIS endonucleases BsaI and BsmBI. Restriction by either BsaI or BsmBI selectively exposes user-definable 4-base cohesive overhang sequences (5'-XXXX vs. 5'-xxxx) at one end of the synthon, while maintaining orthogonal protection groups (with 5'-YYYY vs. 5'-zzzz overhangs) at the opposite end. (B) Schematic representation of the 'split-and-pool' assembly principle. Cohesive ends of entry synthons are selectively de-protected by digestion with either BsaI or BsmBI. Pooling of the de-protected synthons in the presence of ligase results in unidirectional assembly, affording an idempotent tandem repeat synthon by restoration of orthogonal protecting groups on opposite ends. Each product module can recursively enter the assembly cycle (left panel) N times to yield concatameric synthons with 2N elements. The same strategy can be applied to the assembly of heterosynthons (dashed box), which allows for the engineering of chimeric and multimodular proteins or polycistronic genes.

similarity in buffer and temperature requirements (**Table 1**). The recognition sequences of BsmBI and BsaI differ only in a single nucleotide. Conveniently, another IIS endonuclease, BsmAI, recognizes the common subset of these recognition sequences, so that one can optionally combine both cleavage reactions to yield synthons that are deprotected on both ends.

The IIS endonucleases selected generate 4-base 5'-overhangs. The optimal sequences for these overhangs will depend on the purpose of the particular assembly design, but several factors should be carefully considered. First, palindromic overhang sequences carry the risk of unintended self-ligation. Second, GC-rich sequences are generally favored in compatible overhangs for their increased annealing efficiency. This is particularly important in the context of the short reaction times used in our *in vitro* assembly strategy. Third, for designs related to the manipulation of sequences such as tandem domain assemblies, the choice of sequences for the junctions primarily depends on which amino acid sequences will most likely be tolerated within the domain linker. While we purposely introduced scar sequences in the application of the strategy reported here, the design in principle supports seamless assembly formats if the cohesive sequences are chosen appropriately.

Protecting groups also carry 4-base overhang sequences because they are excised together with the synthon from an entry vector. These overhangs must comply with the requirement of being non-palindromic, mutually non-complimentary and, at the same time, orthogonal to the cohesive assembly overhangs.

A Split-and-Pool Strategy for Rapid Construct Assembly

The assembly procedure consists of three stages. First, entry vectors are digested with either of the two IIS endonucleases such that in each case the resulting entry synthon has a 4-base cohesive overhang exposed at one end while one of the orthogonal protecting groups is retained at the opposite end (**Fig. 1B**). Subsequently, complementary entry synthons are pooled and fused by ligation, yielding composite synthons that are idempotent to the entry synthons by restoration of the orthogonal protecting group configuration. At each assembly level, the synthons are digested in parallel with one of the IIS endonucleases essentially as in the first step. The procedure is reminiscent of *split-and-pool* assembly strategies frequently applied in combinatorial chemistry. Within this framework synthons can enter iterative or recursive assembly cycles until the required target construct is obtained (**Fig. 1B**). Since the assembly of orthogonally de-protected synthons is unidirectional, only a single product can be formed. Finally, the assembled product synthons can be ligated back into the empty entry vector, which may serve as a general repository vector (see **Fig. 1A**). Alternatively, the synthons can be directly cloned into a shuttle vector (pShuttle) for subsequent transfer into expression plasmids (**Fig. 2A**). In our laboratory we utilize a standardized set of expression vectors that uniformly contain 5'-BamHI and 3'-NotI restriction sites to facilitate rapid subcloning of constructs into vectors for different expression hosts and are equipped with a variety of tag- or signal peptide decorations. The pShuttle vector is a modified pCR8-TOPO vector carrying a stuffer sequence that is flanked on both sites by BsaI restriction sites, which create cohesive overhangs compatible with those from the de-protected synthons; and additional 5'-BamHI and 3'-NotI restriction sites compatible to our in-house library of expression vectors.

Donor and Acceptor Vectors for Facile Synthon Shuffling

Common to most concatamerization strategies, one technical limitation arising from our assembly design is that it does not support the exchange or insertion of synthons in the final assembly product. We realized that such additional versatility can be added by introducing modular assembly vectors and therefore designed a compatible pair of donor and acceptor vectors (pDA-N and pDA-C) that support modular recombination of synthons and insertion of synthons into a nearly completed assembly product (**Fig. 2B**). Similar to the pShuttle vector, these vectors carry a stuffer sequence flanked by restriction sites for IIS endonucleases to create overhang sequences compatible with the overhangs of de-protected synthons. Synthons can be subcloned into pDA-N and pDA-C vectors, which can either serve as the source of donor synthons or act as acceptor vectors but differ in the relative position, amino- or carboxyl-terminal, of the synthons that they contribute to the translated assembly product (**Fig. 2B,** product 1 and 2). Our design supports two alternative strategies: (i) Recombination of donor and acceptor vectors using the BsaI restriction site together with the BamHI or NotI restriction sites as appropriate, leads to products that have defined 5'- and 3'-synthons (**Fig. 2B,** product 3a). (ii) Recombination of

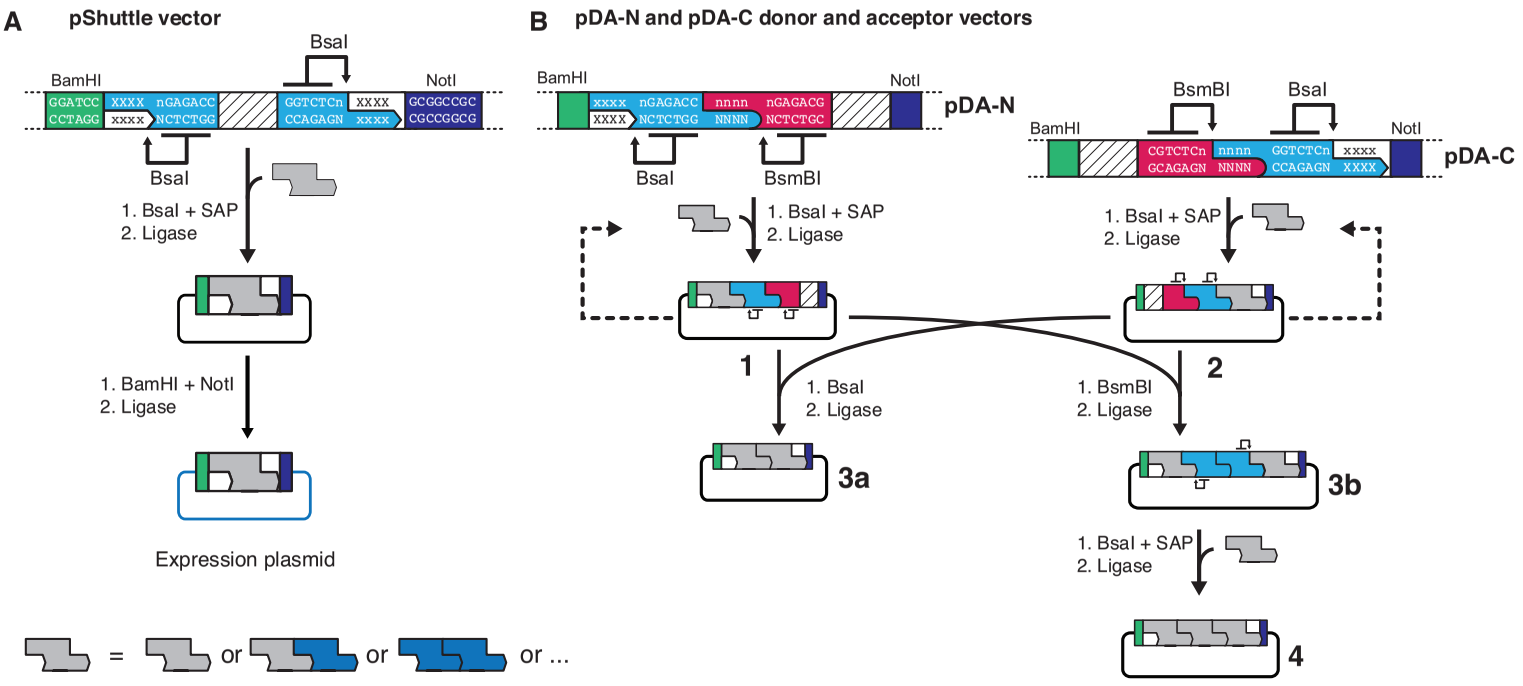

Figure 2 Vectors for synthon recombination and transfer to expression plasmids (A) De-protected synthons can be ligated into a BsaI-digested shuttle vector (pShuttle) that contains 5'-BamHI and 3'-NotI restriction sites compatible with our in-house collection of expression vectors. (B) For applications that require modular recombination or insertion of individual elements, synthons can be ligated into the modular assembly vectors pDA-N or pDA-C. pDA-N vectors that carry synthons encoding amino-terminal elements of protein constructs (**1**) can be combined with synthons encoding carboxyl-terminal elements from pDA-C vectors (**2**) to yield a composite product (**3a**), optionally leaving an additional entry point via BsaI restriction sites to insert additional synthons (**3b**). Final assemblies (**3a** and **4**) contain 5'-BamHI and 3'-NotI restriction sites for transfer into expression vectors.

donor and acceptor vectors using the BsmBI restriction site together with the BamHI or NotI restriction sites as appropriate, leads to products that have defined 5'- and 3'-synthons, while retaining two BsaI sites that provide an additional entry point (**Fig. 2B,** product 3b). As an example, this design supports the rapid insertion of proteins of interest to be sandwiched between fingerprint domains as used frequently in single-molecule force spectroscopy, or the one-step modification of open reading frames by insertion of mutant domains (**Fig. 2B,** product 4).

Assembly of ^{13}FNIII and von Willebrand Factor A2 domain tandem repeats

We tested the applicability of our approach during the construction of a series of expression cassettes harboring tandem arrays of homologous protein domains for single-molecule force spectroscopy. DNA synthons encoding Asn1813 to Thr1901 of a fibronectin type III (^{13}FNIII) domain of human fibronectin [17] were prepared according to the design principles outlined in **Fig. 1A**. The flanking sequences were chosen such that digestion

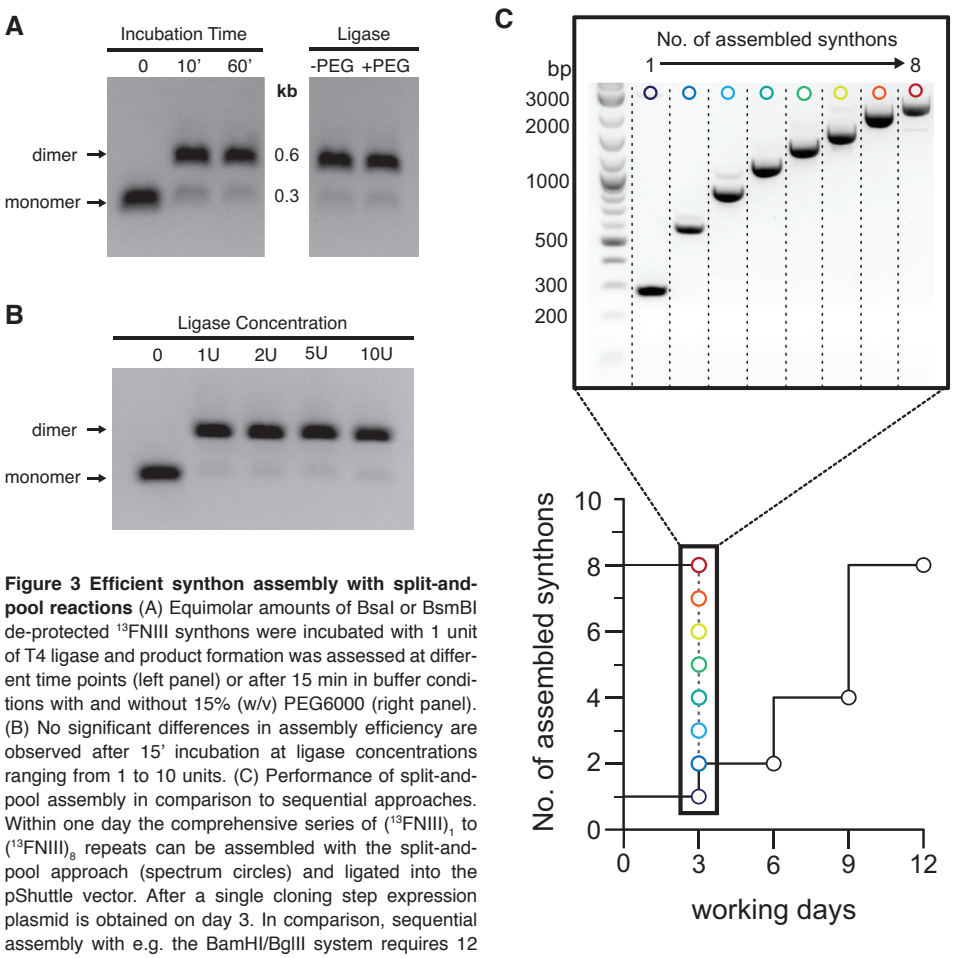

Figure 3 Efficient synthon assembly with split-and-pool reactions (A) Equimolar amounts of BsaI or BsmBI de-protected ^{13}FNIII synthons were incubated with 1 unit of T4 ligase and product formation was assessed at different time points (left panel) or after 15 min in buffer conditions with and without 15% (w/v) PEG6000 (right panel). (B) No significant differences in assembly efficiency are observed after 15' incubation at ligase concentrations ranging from 1 to 10 units. (C) Performance of split-and-pool assembly in comparison to sequential approaches. Within one day the comprehensive series of $(^{13}FNIII)_1$ to $(^{13}FNIII)_8$ repeats can be assembled with the split-and-pool approach (spectrum circles) and ligated into the pShuttle vector. After a single cloning step expression plasmid is obtained on day 3. In comparison, sequential assembly with e.g. the BamHI/BglII system requires 12 days to obtain the $(^{13}FNIII)_8$ construct.

with BsaI produces a 5'-GGGG overhang capable of annealing with a 5'-CCCC overhang present on synthons restricted with BsmBI. The ligation site between synthons translates to a GlyGly sequence in the final protein. BsaI and BsmBI restricted synthons retain a protective group on one end with orthogonal 5'-AAAA overhangs. Entry synthons were processed during three recursive assembly cycles. Relatively short reaction times (10-15 min) at ligase concentrations of 1 unit sufficed to covalently link complementary synthons with excellent yield (**Fig. 3A,B).** We note, however, that we did not assess the efficiency of our approach with overhang sequences other than the cohesive GGGG/CCCC system exemplified in this report.

Using this protocol it proved feasible, in one working day, to assemble the series of constructs comprising one up to eight ^{13}FNIII synthons (denoted $(^{13}FNIII)_1$ through $(^{13}FNIII)_8$; **Fig. 3C**). The cumulative yield loss resulting from repeated restriction-ligation cycles and associated gel purifications prohibited the assembly of even larger constructs. This should be possible, however, by increasing the amount of starting material. Alternatively, selected assemblies could be ligated back into the empty entry vector and amplified in bacterial cultures for further processing (see **Fig. 1**). Compared to conventional methods based on sequential subcloning (e.g. BamHI/BgIII system), our approach saved at least 9 days to yield the largest $(^{13}FNIII)_8$ construct (**Fig. 3C**). Finally, the composite synthons were ligated into the pShuttle vector, as well as the donor/acceptor vectors pDA-N and pDA-C from which they may be recombined with other synthons to yield heterocomposite constructs (see below).

In a similar fashion we constructed multimeric constructs containing tandem repeats encoding residues Val1478 to Gly1674 of the human von Willebrand factor A2 domain (VWFA2). In this case we used the donor and acceptor vector system to clone the assembled $(A2)_2$, $(A2)_4$ and $(A2)_6$ repeats into both of the pDA-N and pDA-C vectors and then combined the appropriate donor synthons and acceptor vectors (see **Fig. 2B**) to construct the final $(A2)_6$, $(A2)_8$ and $(A2)_{10}$ assemblies for recombinant protein expression. The VWFA2 domain has a roughly spherical shape of ~ 30 Å diameter with the amino- and carboxyl-termini protruding from the same side of the domain [18,19]. To facilitate independent folding and to prevent steric clashes between adjacent domains during stretching in single-molecule experiments, we engineered $(GlySer)_3$ repeats on either side of the domain. The resulting 12-residue linker, together with amino- and carboxyl-terminal residues that appear unstructured form the crystal structure [18], leads to an average end-to-end distance of at least 16 Å between the termini of adjacent domains in the concatameric construct as estimated by the worm-like chain model [20].

To verify our assembly format, constructs $(^{13}FNIII)_{2,4,6,8}$ and $(A2)_{6,8,10}$ were expressed in HEK293-EBNA1 (HEK-E) cells and purified by immobilized metal affinity chromatography followed by size exclusion chromatography (**Fig. 4A-D**). We performed thermal denaturation assays to assess the folding state of the purified proteins and to investigate the effect of repeat number on thermal stability. All constructs display a two-state unfolding transition from a stable fluorescence baseline (**Fig. 4E,F**). We observed a gradual decrease in melting temperature (T_m) with increasing number of tandem repeats for the concatameric

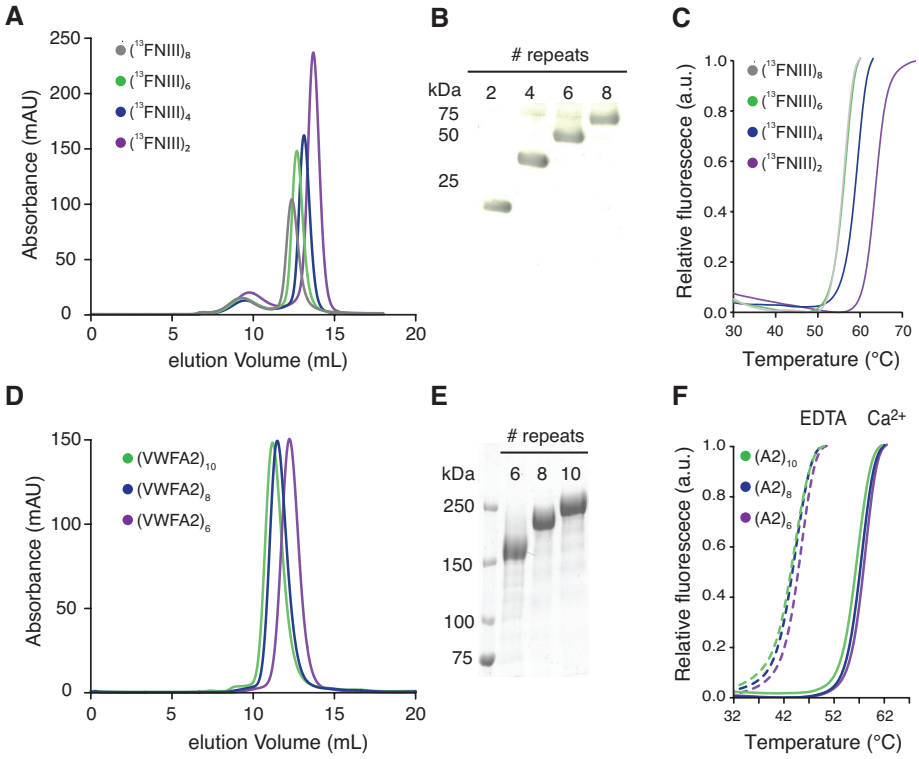

Figure 4 Superposed elution profiles from size exclusion chromatography of $(^{13}FNIII)_{2\text{-}8}$ proteins (A) and $(VWFA2)_{6\text{-}10}$ (B). (C,D) Coomassie stained SDS-PAGE of the purified proteins. (E,F) Unfolding curves from Thermofluor analysis suggest that the concatameric constructs are properly folded. Note the consistent shift of the $(VWFA2)_n$ unfolding curves in the presence and absence of Ca^{2+}.

Table 1 Melting temperatures

Construct	T_m (°C)
$(^{13}FNIII)_2$	62.3 ± 0.2
$(^{13}FNIII)_4$	57.4 ± 0.3
$(^{13}FNIII)_6$	54.5 ± 0.1
$(^{13}FNIII)_8$	54.2 ± 0.1
$(VWFA2)_6 + Ca^{2+}$	57.7 ± 0.01
$(VWFA2)_8 + Ca^{2+}$	57.0 ± 0.1
$(VWFA2)_{10} + Ca^{2+}$	56.1 ± 0.1
$(VWFA2)_6$ + EDTA	44.7 ± 0.01
$(VWFA2)_8$ + EDTA	43.3 ± 0.3
$(VWFA2)_{10}$ + EDTA	43.1 ± 0.1

$(^{13}FNIII)_n$ constructs (Table 2). Consistently, the unfolding temperature of 62.3±0.2 °C for the dimeric $^{13}FNIII$ construct is lower than the value of 72 °C reported for the monomer [21]. In contrast, the series of concatameric VWFA2 constructs showed little variation in thermal stability. We have previously reported on the modulation of thermodynamic and mechanical stability of VWFA2 by binding of Ca^{2+} to a highly conserved calcium-binding site [18]. In accordance, we find a marked T_m shift for buffer conditions containing either Ca^{2+} or EDTA for the tandem domain constructs, indicating that the VWFA2 domains fold into their native structure also in this repetitive context.

Recombinant expression of repetitive DNA sequences carries the risk of genetic instability, potentially resulting in synthesis of truncated or rearranged protein chains. Contrary to our concerns, we found very little contaminants in the supernatant of expression cultures

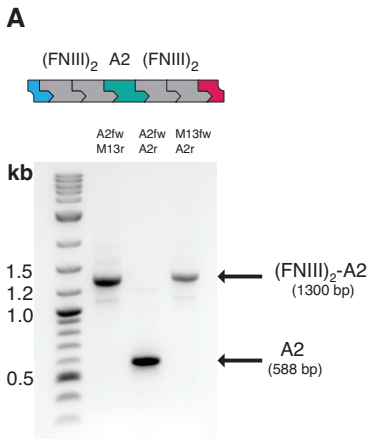

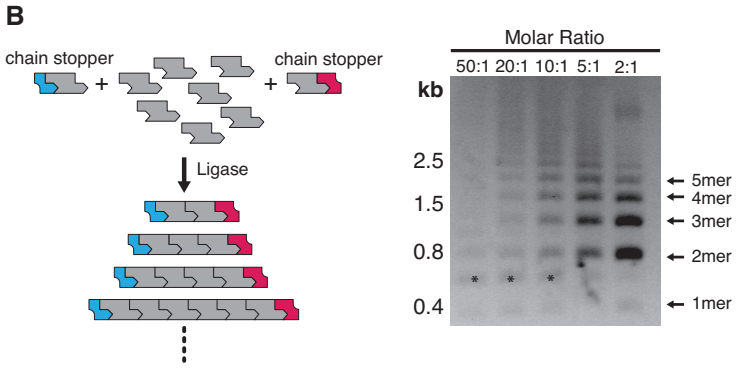

Figure 5 (A) Assembly of $(FNIII)_2$-VWFA2-$(FNIII)_2$ sandwich constructs from a modular assembly vector (top). PCR amplification with specific primers (indicated above the lanes; Table 1) show that the A2 synthon is sandwiched between two ^{13}FNIII repeats. (B) One-pot concatamer formation with orthogonal chain stoppers. Fully de-protected synthons are mixed in different molar ratios with orthogonal chain stoppers (equivalent synthons with protecting groups on one end). Increasing the concentration of chain stoppers shifts the size distribution towards shorter concatamers. Molar ratios of unprotected synthons:chain stoppers are indicated at the top of the lanes. Bands marked with asterisks presumably correspond to circularized dimers.

with a molecular weight different from that expected from the transfected DNA construct (**Fig. 4C,D and Supplementary Fig. S1**). Although we did not perform transcriptional analysis to assess whether these contaminating bands are a consequence of genetic recombination or proteolysis, our data indicates genetic instability is not a major problem in HEK-E cells for our constructs.

Assembly of chimeric (^{13}FNIII)$_2$-VWFA2-(^{13}FNIII)$_2$ constructs

Repetitive constructs are frequently used in single-molecule experiments for reasons of accelerated data sampling and confidence in distinguishing specific tethers from non-specific background. However, such constructs can hamper the identification of intermediates owing to simultaneous unfolding of structural elements in other domains of the repetitive context. In such cases, the unambiguous assignment of unfolding traces is facilitated if individual domains of interest are sandwiched between a repetitive series of protein domains whose elastic properties are well characterized, such as immunoglobulin-like domains of titin [13,14], *Dyctostelium discoideum* filamin (ddFLN) [22] or fibronectin FNIII domains [17]. Our donor and acceptor vectors support the rapid assembly of such constructs and we illustrate this process by sandwiching single VWFA2 domains between amino- and carboxyl-terminal $^{13}(FNIII)_2$ repeats (**Fig. 5A**). For this purpose, a $^{13}(FNIII)_2$-

X-$^{13}(FNIII)_2$ vector construct was created that contains inversely oriented BsaI sites between the ^{13}FNIII repeats to form the entry point for synthon insertion (**see Fig. 2B**). $^{13}(FNIII)_2$ synthons were subcloned into both pDA-N and pDA-C vectors and subsequently recombined by ligating the BsmBI/BamHI fragment from the resulting pDA-N-$^{13}(FNIII)_2$ vector (acting as the donor) into the BsmBI/BamHI-linearized pDA-C-$^{13}(FNIII)_2$ vector (acting as the acceptor). A synthon encoding residues Val1478 to Gly1674 of the VWFA2 domain and flanking $(GlySer)_3$ linkers was subsequently inserted between the $^{13}(FNIII)_2$ repeats using the BsaI restriction sites. The successful assembly was verified by PCR (**Fig. 5A**).

Discussion

We have demonstrated that the application of IIS restriction endonucleases can be readily combined with a simple protecting group concept to create a versatile framework for the rapid assembly of modular DNA building blocks into functional gene constructs. Several features distinguish our approach from previously reported strategies: Contrary to conventional restriction enzyme or recombination-based methods that require subcloning steps between consecutive assembly cycles, the application of enzymatically cleavable protecting groups and the restoration of idempotent composite synthons permits assembly of any arbitrary sequence of modular DNA units into a functional gene product *in vitro*. As we illustrate with the construction of ^{13}FNIII and VWFA2 tandem repeats, this approach considerably accelerates the assembly procedure. One detriment that comes with our strategy is that it requires repeated cycles of gel purification, making it labor-intensive and, as of yet, unsuitable for automation. Considering the remarkable efficiency of the ligation reactions that we observed in the assembly steps process, one could consider omitting the purification steps and submit samples to direct split-and-pool reaction cycles. This will be applicable only if the project concerns the construction of a series of homologous repeats, since obviously even spurious reactive contaminants are unacceptable if a defined set of heterogeneous synthons is to be assembled into a particular sequence.

Several multi-fragment strategies [5,7,16,23] that have been recently developed to address a similar scenario depend on a distinct pair of cohesive overhang sequences for each sub-fragment. Due to restricted redundancy of the genetic code, this becomes a limitation if the amino acid sequences of the linkers between domains are to be identical. The concept of orthogonal protecting groups straightforwardly bypasses these constraints and linker sequences can be readily standardized by appropriate primer design. Common to all cloning strategies that rely on restriction enzymes, however, our approach is hampered by the probability of the recognition sequences to occur within the target gene fragments. Although these sites may be removed by silent mutagenesis or excluded a priori by employing custom-designed synthetic gene units, this may represent a limitation regarding applications that involve larger DNA modules. Alternative to the presented sequential assembly strategy, mixtures of products with a varying repeat number can be obtained by mixing fully de-protected synthons with singly deprotected synthons acting as orthogonal chain stopper units. Depending on the stochiometric ratios used for these

reactions, libraries of composite modules can be constructed in a one-pot reaction (**Fig. 5B**). We introduce further versatility by establishing a three-point entry vector system based on donor and acceptor vectors. These vectors form a cassette framework for the rapid modification of open reading frames to revise assemblies that have failed in recombinant expression trials, the insertion of mutated or truncated synthons or to sandwich target domains between internal standards in force spectroscopy applications.

Perspective

The directional *in vitro* assembly strategy based on orthogonal protecting groups is robust, technically simple and can be readily tailored to suit individual assembly scenarios. We anticipate that our method will significantly facilitate and accelerate protein engineering for single-molecule force spectroscopy experiments, and may find broader applicability in other settings involving the reconstitution and modification of complex modular sequences.

Supporting Information
This text contains supplementary figures.

Funding
This work was supported by ECHO grant 700.55.012 from the Council of Chemical Sciences of the Netherlands Organization for Scientific Research (NWO) to EGH.

Author contributions
Conceived and designed the experiments: AJ EGH. Performed the experiments: AJ. Analyzed the data: AJ EGH. Wrote the manuscript: AJ EGH.

Experimental Procedures

General. Sequences of oligonucleotides are provided in the supplementary data. All entry synthons and vectors were verified by DNA sequencing.

Preparation of DNA synthons. A DNA fragment encoding residues 1813 – 1901 of human ^{13}FNIII (UniProt accession P02751) flanked by 5'-BsmBI-BsaI and 3'-BsaI-BsmBI restriction sites was optimized for mammalian codon usage, RNA structure, and GC content and synthesized (DNA 2.0, Menlo Park, CA). Overhang sequences were chosen as AAAA for the protection group overhangs and GGGG for the cohesive overhangs in the 5'-BsmBI-BsaI sequence vs. AAAA and CCCC for protection group and cohesive overhangs in the 3'-BsaI-BsmBI sequence (compare Fig. 1A). To preserve the reading frame the 3' CCCC bases are preceded by two additional C nucleotides. A DNA fragment encoding residues 1478 – 1674 of the human VWFA2 domain (UniProt accession P04275; p.V1565A polymorphism) and containing the same overhang sequences was constructed as described [18] using oligos VWFA2.fw and VWFA2.rev. A silent mutation was introduced by QuikChange mutagenesis to remove the internal BsmBI site in the A2 fragment. Both constructs were cloned into pCR8-TOPO (Invitrogen) for DNA amplification.

Construction of shuttle and donor/acceptor vectors. A DNA stuffer fragment encoding part of the VWF cDNA was amplified by PCR with oligos containing a 5'-BamHI-BsaI-BsmBI sequence for pDA-N (oligos pDA-N.fw and pDA-N.rev) or a 5'-NotI-BsaI-BsmBI sequence for pDA-C (oligos pDA-C.fw and pDA-C.rev), respectively. The PCR products were then cloned into pCR8-TOPO and a fragment of the stuffer sequence containing internal BsaI sites was excised by NsiI digestion to create the donor/acceptor vectors pDA-N and pDA-C, respectively. The plasmid backbone of pCR8-TOPO does not contain internal BsaI, BsmBI or BsmAI sites. Similarly, the pShuttle vector was obtained from PCR amplification of the stuffer fragment using oligos pShuttle.fw and pShuttle.rev.

Assembly of ^{13}FNIII and VWFA2 repeats. Plasmid DNA of pCR8-^{13}FNIII and pCR8-VWFA2 was prepared from 50 mL o/n cultures using a Midiprep kit (Sigma Aldrich) and concentrated by ethanol precipitation to obtain ~ 0.7 mg DNA at 1.5 – 2.5 μg/μl. 50 - 100 μg DNA was mixed with 10x NEB reaction buffer 3 and either 5 μl BsaI or BsmBI (New England Biolabs) in a total volume of 50 - 100 μl and incubated at 50 °C for 1h on a thermal cycler (Bio-Rad S1000). After a 30 min gel electrophoresis run on 2% (w/v) agarose gels, synthon fragments were excised and gel purified using a DNA gel purification kit (Promega). Usually around 10.5 μg of $(^{13}FNIII)_{mono}$ synthon were recovered (~ 85 % yield). Equal molar amounts (typically 250 - 500 ng at ~ 100 – 250 ng/μl) of orthogonally protected synthons were mixed, 0.5 - 1 unit T4 ligase (Fermentas) and T4 ligase buffer (Fermentas) were added and the ligation mixture was incubated for 10-20 min at 16 °C. Adding additional ligase had little effect on ligation efficiency. A 30 min gel electrophoresis run on 0.8 - 1.5 % (w/v) agarose gels provided sufficient separation of product from unreacted synthons. Product synthons were gel purified as described above and split into two equal volumes, which were treated with either BsaI or BsmBI to yield orthogonally protected dimers. This assembly process was repeated until the target constructs were obtained. For further processing, the target synthons were digested for 30 min with BsaI and BsmBI to de-protect both ends and purified over a DNA purification spin column (Promega). 1 μg pShuttle, pDA-N and pDA-C vectors were digested with BsaI for 1h at 50 °C after which the vectors were de-phosphorylated by the addition of 0.5 units shrimp alkaline phosphatase (SAP, Fermentas) for 1h at 37 °C. We found that self-ligation could be significantly reduced by repeating this treatment, without adding new BsaI endonuclease. $(FNIII)_n$ synthons were ligated directly into the BsaI-linearized pShuttle vector whereas $(A2)_n$ constructs were ligated into pDA-N and pDA-C donor and acceptor vectors using low vector concentrations of 0.3-0.6 ng/μl and vector:insert ratios below 4:1, which we found to reduce synthon self-assembly.

Assembly of $(FNIII)_2$-(VWFA2)-$(FNIII)_2$ constructs
$(FNIII)_2$ synthons were assembled as described above and ligated into BsaI-linearized pDA-N and pDA-C vectors. Next, the $(FNIII)_2$ synthon was digested from the pDA-N-$(FNIII)_2$ vector (3 μg) using BsmBI and BamHI and ligated into the BsmBI/BamHI-linearized pDA-C-$(FNIII)_2$ acceptor vector. The resulting vector pDA-$(FNIII)_2$-X-$(FNIII)_2$ was linearized with BsaI to create an entry point for the A2 synthon. The BsmBI/BsaI de-protected A2 synthon was subsequently ligated into the linearized vector to create the chimeric pDA-$(FNIII)_2$-A2-$(FNIII)_2$ construct.

Protein Expression and Purification. Tandem repeat constructs of ^{13}FNIII and VWF-A2 were ligated into the BamHI and NotI sites of a modified pTT3 vector carrying a cystatin S signal peptide, an amino-terminal hexahistidine tag and a carboxyl-terminal biotin acceptor peptide sequence (GLNDIFEAQKIEWHE). Human embryonic kidney cells stably expressing EBNA1 were transiently transfected as described [24]. Proteins were purified by Ni-sepharose affinity chromatography (GE Healthcare), followed by size exclusion chromatography in 20 mM HEPES (pH 7.5), 150 mM NaCl on Superdex 200 10/300 column (GE Healthcare). Proteins were concentrated to 1 mg/mL and stored at -80 ºC.

Thermal denaturation assays
Thermal denaturation assays were performed essentially as described [18]. Briefly, 6.25 μl of 10x Sypro Orange (Sigma-Aldrich) was mixed with 6.25 μl of a 0.4 mg/mL protein solution in 20 mM HEPES (pH 7.5), 150 mM NaCl and immediately mixed with 12.5 μl of assay buffer containing 50 mM HEPES (pH 7.5), 150 mM NaCl for ^{13}FNIII concatamers or assay buffer containing additionally 1 mM $CaCl_2$ or 5 mM EDTA for VWFA2 concatamers. The apparent T_m of individual unfolding curves (n=3) was determined from a sigmoidal fit to the normalized fluorescence data [25].

References

1. Benoit RM, Wilhelm RN, Scherer-Becker D, Ostermeier C (2006) An improved method for fast, robust, and seamless integration of DNA fragments into multiple plasmids. *Protein Expr Purif* **45**: 66–71.
2. McIntyre GJ, Groneman JL, Tran A, Applegate TL (2008) An infinitely expandable cloning strategy plus repeat-proof PCR for working with multiple shRNA. *PLoS ONE* **3**: e3827.
3. Geu-Flores F, Nour-Eldin HH, Nielsen MT, Halkier BA (2007) USER fusion: a rapid and efficient method for simultaneous fusion and cloning of multiple PCR products. *Nucleic Acids Res* **35**: e55.
4. Zhu B, Cai G, Hall EO, Freeman GJ (2007) In-fusion assembly: seamless engineering of multidomain fusion proteins, modular vectors, and mutations. *BioTechniques* **43**: 354-359
5. Engler C, Kandzia R, Marillonnet S (2008) A One Pot, One Step, Precision Cloning Method with High Throughput Capability. *PLoS ONE* **3**: e3647.
6. Fernandes S, Tijssen P (2008) Seamless cloning and domain swapping of synthetic and complex DNA. *Anal Biochem* **385**: 171-173.
7. Weber E, Engler C, Gruetzner R, Werner S, Marillonnet S (2011) A modular cloning system for standardized assembly of multigene constructs. *PLoS ONE* **6**: e16765.
8. Bieniossek C, Nie Y, Frey D, Olieric N, Schaffitzel C, et al. (2009) Automated unrestricted multigene recombineering for multiprotein complex production. *Nat Methods* **6**: 447. doi:10.1038/nmeth.1326
9. Suzuki Y, Kagawa N, Fujino T, Sumiya T, Andoh T, et al. (2005) A novel high-throughput (HTP) cloning strategy for site-directed designed chimeragenesis and mutation using the Gateway cloning system. *Nucleic Acids Res* **33**: e109.
10. Bornschlögl T, Rief M (2011) Single-molecule protein unfolding and refolding using atomic force microscopy. *Methods Mol Biol* **783**: 233–250.
11. Marszalek PE, Lu H, Li H, Carrion-Vazquez M, Oberhauser AF, et al. (1999) Mechanical unfolding intermediates in titin modules. *Nature* **402**: 100–103.
12. Carrion-Vazquez M, Oberhauser AF, Fisher TE, Marszalek PE, Li H, et al. (2000) Mechanical design of proteins studied by single-molecule force spectroscopy and protein engineering. P*rog Biophys Mol Biol* **74**: 63–91.
13. Carrion-Vazquez M, Oberhauser AF, Fowler SB, Marszalek PE, Broedel SE, et al. (1999) Mechanical and chemical unfolding of a single protein: a comparison. *Proc Natl Acad Sci USA* **96**: 3694–3699.
14. Steward A, Toca-Herrera JL, Clarke J (2002) Versatile cloning system for construction of multimeric proteins for use in atomic force microscopy. *Protein Sci* **11**: 2179–2183.
15. Blake W, Chapman B, Zindal A, Lee M, Lippow S, et al. (2010) Pairwise selection assembly for sequence-independent construction of long-length DNA. *Nucleic Acids Res* **38**: 2594.
16. Engler C, Gruetzner R, Gruetzner R, Kandzia R, et al. (2009) Golden Gate Shuffling: A One-Pot DNA Shuffling Method Based on Type IIs Restriction Enzymes. *PLoS ONE* **4**: e5553
17. Oberhauser AF, Badilla-Fernandez C, Carrion-Vazquez M, Fernandez JM (2002) The mechanical hierarchies of fibronectin observed with single-molecule AFM. *J Mol Biol* **319**: 433–447.
18. Jakobi AJ, Mashaghi A, Tans SJ, Huizinga EG (2011) Calcium modulates force sensing by the von Willebrand factor A2 domain. *Nature Communications* **2**: 385.
19. Zhang Q, Zhou Y-F, Zhang C-Z, Zhang X, Lu C, et al. (2009) Structural specializations of A2, a force-sensing domain in the ultralarge vascular protein von Willebrand factor. *Proc Natl Acad Sci USA* **106**: 9226–9231.
20. Zhou H-X (2004) Polymer models of protein stability, folding, and interactions. *Biochemistry* **43**: 2141–2154.
21. Novokhatny V, Schwarz F, Atha D, Ingham K (1992) Domain structure and domain-domain interactions in the carboxy-terminal heparin binding region of fibronectin. *J Mol Biol* **227**: 1182–1191.
22. Dietz H, Rief M (2004) Exploring the energy landscape of GFP by single-molecule mechanical experiments. *Proc Natl Acad Sci USA* **101**: 16192–16197.
23. Matsumoto A, Itoh TQ (2011) Self-assembly cloning: a rapid construction method for recombinant molecules from multiple fragments. BioTechniques 51: 55–56.
24. Durocher Y, Perret S, Kamen A (2002) High-level and high-throughput recombinant protein production by transient transfection of suspension-growing human 293-EBNA1 cells. *Nucleic Acids Res* **30**: E9.
25. Lo M-C, Aulabaugh A, Jin G, Cowling R, Bard J, et al. (2004) Evaluation of fluorescence-based thermal shift assays for hit identification in drug discovery. *Anal Biochem* **332**: 153–159.

Supplementary Information

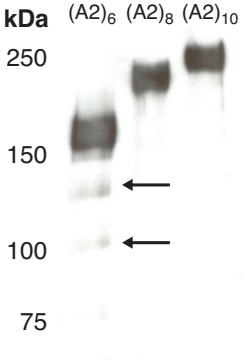

Figure S1 Western blot of $(VWFA2)_n$ in expression medium demonstrating minor contamination by concatamers with a molecular weight different from the target construct (indicated by arrows). These contaminants may either result from genetic recombination or proteolysis. Horse radish peroxidase-coupled α-VWF (Dako) was used to stain the blot.

CHAPTER 5

General Discussion

Arjen J. Jakobi
Crystal & Structural Chemistry, Bijvoet Center for Biomolecular Research, Department of Chemistry, Utrecht University, Padualaan 8, 3584 CH Utrecht, The Netherlands

The formation of a platelet plug after vessel injury is critical to prevent blood loss from severed vessels. In the microcirculation, one of the essential steps in the formation of haemostatic plugs is the recruitment of platelets to the site of vessel injury by the adhesive glycoprotein von Willebrand Factor (VWF). The capacity of VWF to bind platelets is dependent on shear forces, which induce conformational changes leading to activation, but also regulate proteolytic feedback inhibition of thrombus growth. Here we discuss the insights that structural, biochemical and single-molecule studies have provided into the molecular mechanisms by which force-dependent proteolytic cleavage at the A2 domain regulates multimer length and platelet-adhesive potential of VWF.

VWF is a central player of haemostasis in assisting the adhesion of platelets to components of the damaged vessel wall in the rapid flow environment of capillaries and precapillary arterioles [1,2]. In this process, VWF acts as an adaptor molecule capable of tethering platelets to the extracellular matrix by providing a multivalent binding platform for exposed subendothelial matrix collagen at the lesion, and adhesion receptors on the platelet surface [3]. Regulation of VWF-mediated platelet adhesion and aggregation is of critical importance for haemostasis. Qualitative defects and quantitative deficiency of VWF result in severe bleeding disorders that are formally categorized into the various subtypes of von Willebrand disease (VWD) [4]. Conversely, haemostatic imbalance may also result from inhibition of a feedback mechanism regulating VWF multimer length through proteolytic cleavage by the plasma metalloprotease ADAMTS-13 (a disintegrin and metalloprotease with thrombospondin-1 type motif, member 13), which may lead to the persistance of ultra-large VWF multimers and predisposes to the formation of occlusive intravascular platelet aggregates associated with thrombotic thrombocytopenic purpura (TTP) [5,6].

VWF is synthesized by endothelial cells and platelet precursor megakaryocytes [7]. Mature VWF is a 2,050 amino acid residue protein [8] that polymerizes through the formation of amino- and carboxyl-terminal disulfide bridges into multimers composed of up to 250-3000 monomers [9]. These ultra-large multimers (ULVWF) are secreted by stimulated

endothelial cells from specialized intracellular storage organelles [10], and upon secretion are rapidly proteolyzed by ADAMTS-13 into smaller forms [11]. The ability of VWF to recruit platelets to sites of vascular injury is dependent on hydrodynamic shear forces [2] and tightly linked to the length of these multimers [1]. Importantly, the interdependence of haemostatic potential and multimer length is not only a consequence of avidity effects, but, of equal importance, the length of the multimers also critically defines their hydrodynamic properties determining susceptibility to conformational changes in shear flow [12-14]. Shear forces on polymer chains depend on the distance between opposite ends of the chain in different shear lamina, and therefore scale with the effective length rather than the molecular weight of the polymer [15-17]. VWF is a complex, mosaic multi-domain protein containing a number of repetitive VWA, VWB, VWC, VWD domain motifs that are eponymous for a range of extracellular matrix proteins [18,19]. VWF multimers appear as elongated, highly flexible strings with repeating symmetry units in electron microscopy (EM) [20-22]. Very recently, an elegant study has provided the first high contrast micrographs that permitted the assignment of individual domains along the entire length of VWF monomers [23]. Prominent globular densities concentrate at the amino-terminal VWD and VWA domains, while much of the length of VWF monomers is contributed by the carboxyl-terminal VWC and VWC-like B domains, both of which appear as prolate spheroids with comparable dimensions in negatively-stained electron micrographs [23]. The atomic resolution structures of homologous VWC domains from collagen II [24] and crossveinless 2 bound to bone morphogenic protein 2 (BMP-2) [25] reveal that these domains are devoid of a hydrophobic core, but instead contain an intertwined arrangement of two extended subdomains that are connected by disulfide bridges. This arrangement maximizes extension, while at the same time preserving a stable fold. The specific properties of its domains, the great flexibility and length arising from their spatial arrangement and the dependence of effective shear forces on chain length suggests that VWF has evolved a unique molecular architecture allowing it to sense and respond to particular hydrodynamic environments by force-dependent conformational changes. The particular arrangement of VWF domains furthermore suggests that such conformational changes will primarily involve unraveling of the globular array of amino-terminal VWD and VWA domains, likely by disruption of domain-domain interactions in these regions. Interestingly, the core elements of the haemostatic functionality are present in this amino-terminal region (see chapter 1). Moreover, the D'D3 and A2 domains appear to modulate the platelet-binding potential of the A1 domain under shear [26,27], lending further support to our considerations.

The effect of shear stress on conformation and adhesive capacity of VWF is highly relevant. VWF multimers undergo reversible globule-stretch transitions from a compact to an extended conformation in response to high shear forces [13,16,22], a process that activates VWF for platelet binding [1]. However, shear stress also induces local conformational changes in the A2 domain that expose the scissile bond for cleavage by ADAMTS-13 [17,28], reducing multimer length and thrombogenicity. Large VWF multimers are most responsive to shear forces [12,13,16] and, consequently, are most potent in their capacity to recruit platelets [29,30]. At the same time, these multimers are also most susceptible to

proteolysis by ADAMTS-13 [11]. Hence, the maintenance of the balance between these disparate processes is of central importance in regulating platelet adhesion and aggregation in the microvascular circulation.

We have recently seen rapid progress in understanding the complexity of VWF conformational dynamics. Biophysical studies and concepts from polymer theory have contributed significant conceptual advances in describing the physical basis of conformational transitions that VWF multimers undergo in shear flow [13,16,17,31-33]. In particular, single-molecule force spectroscopy permits to study the effect of mechanical cues on the conformation of individual molecules [34] and reveals dynamic details inaccessible by ensemble methods [35,36]. By monitoring (one-dimensional) conformational fluctuations at high spatial resolution, these techniques, in combination with structural data, allow dissecting molecular pathways connecting distinct structural states [37]. With the identification and structure elucidation of a novel calcium-binding site in the A2 domain of VWF and its functional characterization by single-molecule techniques described in this thesis, we add relevant new insight into the mechanism of force sensing by the A2 domain and emphasize the dynamic complexity underlying the regulation of VWF function by conformational change.

Evolutionary adaption and structural specializations of a force sensor domain

The topology of secondary structure motifs and their orientation relative to the tensile force vector is interrelated with the mechanical stability of a protein. In particular, disulfide bridges formed between distant cysteine residues can effectively protect secondary structure elements grafted between these covalent bonds against external torque or stretching forces [38]. The sequence of VWF is remarkably cysteine-rich [39] and all cysteine residues appear to form intra- or interchain disulfide bridges [40-42]. Importantly, the A2 domain is the only domain within VWF that is devoid of long-range cysteine bridges; unlike its neighboring and structurally homologous A1 [43] and A3 [44] domains, A2 does not have a disulfide bond connecting the amino- and carboxyl termini. Instead, two adjacent cysteine residues form a vicinal disulfide bond at the carboxyl terminus ([45] and chapter 2). The absence of a long-range cysteine bridge renders A2 susceptible to conformational changes induced by tensile stretching forces and thereby places this domain in a central position to operate as a mechanoresponsive element of VWF. The A2 domain has acquired additional structural specializations supporting its function as a force sensor domain. Uniquely in A2, the α_4-helix is replaced by an elongated loop (α_4-less loop) ([45] and chapter 2) that presumably destabilizes the structure and sets the topology of A2 apart from other structurally characterized VWA type domains in VWF [44,46], integrins [47] and complement factor B [48]. As we show in chapter 2, A2 binds calcium with its $\alpha_3\beta_4$-loop. The location of the calcium-binding site is fundamentally different from metal binding sites of other VWA domains, such as the metal-ion dependent adhesion sites found in integrin I domains [49,50], and is the first metal-binding site identified in VWA domains at this position. The topology of A2 reveals that the calcium-binding site at the $\alpha_3\beta_4$-loop is located

in a critical position, precisely at the hinge between the two lobes of the Rossmann-like fold (see chapter 1). Interestingly, metal binding sites are frequently characterized by local fluctuation minima and as such are often located at key mechanical positions [51]. Molecular dynamics simulations (chapter 2) indicate that calcium, by restraining mobility of the $\alpha_3\beta_4$-loop and stabilizing the hydrogen-bonding network of the central β-sheet, occupies a similar site in A2, suggesting that calcium binding by A2 is an important evolutionary adaption to its function as a force sensor domain.

Unfolding and refolding: A delicate equilibrium regulating ADAMTS-13 cleavage?

Very recently, several single-molecule studies have estimated unfolding forces of the A2 domain with the atomic force microscope (AFM) [52] and optical tweezers [17,53]. These studies revealed that A2 unfolds at forces ranging between 5 and 25 pN, similar to the force distributions we observed for unfolding of single A2 domains with the optical trap (chapter 2). Theoretical considerations predict that peak forces on VWF multimers scale as the square of monomer number from each free end [15,17]. One can infer from such calculations that, at shear rates typically found in the microcirculation, A2 domains will experience tensile forces that are of the same order of magnitude as those required for A2 unfolding in single-molecule assays (see chapter 1). Importantly, the second power dependence of force on length directs cleavage toward the center of VWF multimers [54], which maximizes the effective reduction in haemostatic potential of fragmented multimers generated by cleavage.

Unfolding activates A2 for proteolysis, and the average unfolding force therefore is a critical parameter determining the effective substrate concentration under a particular hydrodynamic condition. Calcium binding in A2 modulates substrate activation by increasing the threshold force required for A2 unfolding (chapter 2) and thereby effectively limits unfolding to conditions of high shear stress. Intriguingly, such stresses are maximal in the confined vessel lumen of capillaries and arterioles [55], precisely where the requirement of VWF for platelet adhesion, but also the acute risk of VWF-mediated thrombus formation, are highest. Our experimentally determined force distributions imply that, under such conditions, a significant part of the A2 domains will be unfolded (chapter 2). Substrate-activated proteolysis in the presence of constitutively active ADAMTS-13 and the absence of known inhibitors would then suggest that all unfolded A2 domains are cleaved, which contradicts the existence of characteristic multimer distributions of VWF in plasma of healthy individuals [4]. This apparent discrepancy can be resolved by assuming that the conformational change leading to substrate activation is reversible and, consequently, that the reverse process leading to deactivation of the substrate limits VWF cleavage and contributes to regulating ADAMTS-13 cleavage. The K_M of 1.7 μM [56] for enzymatic cleavage of A2 by ADAMTS-13 is substantially higher than the plasma concentration of ADAMTS-13 of 3-7 nM [57]. In combination with a catalytic constant k_{cat} ~1.3 s^{-1} (chapter 3 and [56]) for hydrolysis of the scissile bond, this difference leads to a minimum time scale for proteolysis of ~ 190-440 s and suggests that, *in vivo*, VWF cleavage is limited by ADAMTS-13 concentration. As a consequence, the refolding rate of A2 as a function of tensile force is a major

determinant for the extent of ADAMTS-13 cleavage *in vivo*. Single-molecule experiments have contributed significantly to our understanding of this process and have emphasized the critical role of calcium in maintaining a balanced level of scissile bond accessibility (chapter 2). We have demonstrated that refolding of A2 in the presence of calcium is accelerated approximately sixfold and our data stress the importance of the conformational dynamics underlying this mechanism in showing that refolding to the native state proceeds via distinct intermediates. Interestingly, a very recent study that also used the optical trap to investigate A2 refolding has confirmed our estimated increase of the refolding rate in the presence of calcium, but does not observe transient intermediates [58]. The existence of calcium-induced refolding intermediates as identified in our study and the effect of such states on the folding landscape provide an attractive explanation for increased refolding rates [59] and the ability of a polypeptide chain to compact against applied force [60-62]. In contrast, such effects are difficult to rationalize in the absence of productive folding intermediates. We therefore believe that the apparent dissimilarities between refolding pathways observed in the two studies are a result of differences in instrument resolution and experimental parameters like force loading rates, trap stiffness and compliance of the tethers, which strongly affect the dynamics of the system [63,64] and may facilitate, or obscure, the detection of transient intermediates. Irrespective of these differences, both studies converge in their major conclusion and numerical estimates of refolding dynamics of A2, underscoring the relevance of the force-dependent refolding rate constant as one of the prime parameters determining ADAMTS-13 cleavage and stressing the critical role of calcium in this process.

Important questions remain. Whereas our data demonstrate the relevance, and map out the overall mechanism of calcium-assisted force sensing of A2, the precise structural transitions along the folding and unfolding pathways are less obvious. We currently do not know the exact structure of the calcium-stabilized intermediate, nor do we know whether this intermediate is on- or off-pathway to the native state. Interestingly, the force required for unfolding of the intermediate (I) is higher than that required for disruption of the native state (N). Moreover, force distributions for the transitions from the native to the unfolded state (N -> U) in the absence of calcium, and those for the transition from the native state to intermediate (N -> I) in the presence of calcium, are similar. These observations imply that, at low force, the intermediate state is more stable than the native state, effectively increasing the height of the unfolding energy barrier to the transition state. Assuming that unfolding starts at the carboxyl-terminus [17,65] as expected from the topology of A2, this model would be consistent with the location of the calcium-binding site in our crystal structure, which presumably does not affect unfolding of the carboxyl-terminus up to the $\alpha_3\beta_4$-loop. Importantly, this fragment contains all elements required for substrate recognition and cleavage by ADAMTS-13 [56,66,67]. However, the worm-like chain fits to our data suggest that the intermediate does not have native calcium coordination. Most of the calcium-binding site is formed by a continuous sequence in the $\alpha_3\beta_4$-loop, which makes it tempting to speculate that this sequence is also involved in calcium coordination of the

intermediate. Such a model would imply that, in the intermediate structure, the amino-terminal calcium ligand is substituted by the formation of new, non-native contacts that maintain the stability of the intermediate under force and facilitate refolding in the rate-limiting transition from the unfolded to the intermediate state (I <- U). A related mechanism, involving dislocation of a peripheral β-strand, has been proposed for immunoglobulin domains in titin [68] and in fibronectin [69]. Further investigations, using force-clamp experiments and mutant constructs, ideally in combination with single-molecule fluorescence techniques, will be required to (i) reveal the identity of the individual structural states along the unfolding and refolding trajectories, (ii) characterize structural dynamics associated with these states and (iii) clarify whether the intermediates can be cleaved by ADAMTS-13.

The relevance of calcium in ADAMTS-13 activity assays

Our findings also have practical implications for the characterization of ADAMTS-13 activity in biochemical assays, and for clinical laboratory assays in the diagnosis of TTP [70]. A long-standing debate involves the preferential use of barium [71] or calcium [72] for optimal activity in ADAMTS-13 cleavage assays. The significant effect of calcium on stability and ADAMTS-13 cleavage of A2 that we have revealed in our analysis sheds new light on this controversy. In a comprehensive study using unstructured VWF substrates it has been convincingly demonstrated that cleavage requires zinc and calcium to maximally activate ADAMTS-13, but that comparable activity is preserved if calcium is substituted by barium [73]. If ADAMTS-13 assays such as the FRETS-VWF73 assay [74] employ partial, unstructured VWF substrates that do not bind calcium (chapter 2), the effective substrate concentration is equivalent independent of whether buffer conditions contain calcium or barium. The situation is different in alternative proteolysis assays using multimeric VWF [75] or recombinant A2 [76] as the substrate. In these assays the substrate conformation and hence the efficiency of ADAMTS-13 cleavage is sensitive to the presence of calcium, but not of barium. As we have shown in chapter 2, absolute activities determined from such assays will therefore differ significantly depending on the buffer conditions used. These considerations may provide an explanation for the broad variability of absolute activity levels among different assay protocols [70]. Our results advocate the use of FRETS-VWF73 assays, which are indiscriminate to the presence of calcium, and prompt a cautionary note for the comparison of absolute activities derived from ADAMTS-13 cleavage assays using multimeric VWF or recombinant A2.

A mechanistic picture of ADAMTS-13 substrate recognition and cleavage

The previous paragraphs have underlined the importance of unfolding and refolding dynamics for the population of particular substrate conformations regulating availability of the scissile bond for ADAMTS-13 cleavage. ADAMTS-13 cleaves VWF with high specificity at the Tyr1605-Met1606 peptide bond [77]. The carboxyl-terminal residues Asp1596-Arg1668 (VWF73) of the A2 domain contain most of the elements required for full proteolytic activity of ADAMTS-13 [56,78] and, in the unfolded state, bind via several exosite interactions to the metalloprotease, disintegrin, thrombospondin-1, cysteine-rich

and spacer domains of ADAMTS-13 [78,79]. Incremental addition of these domains in recombinant ADAMTS-13 constructs increases the rate of cleavage up to 300-fold [78]. The metalloprotease domain alone does not show significant activity, or, after extended incubation loses specificity for the Tyr1605-Met1606 peptide bond [79]. Although this suggests that the metalloprotease domain does not appreciably contribute to substrate recognition, deletion of residues Asp1596-Val1604 abolishes cleavage [56]. We and others have clarified the role of these residues in substrate recognition and demonstrated that Leu1603 and Val1604 are the only amino-terminal elements required for cleavage of the Tyr1605-Met1606 bond (chapter 2 and 3, [80]). In particular, we have shown in chapter 3 that efficient cleavage of VWF by ADAMTS-13 depends on amino-terminal anchoring of VWF via interactions of Leu1603 with the metalloprotease domain, as also proposed by Xiang et al. [80]. The metalloprotease domain alone, however, does not cleave VWF efficiently and does not retain specificity for the Tyr1605-Met1606 peptide bond [79]. On the basis of this data, a recognition and cleavage mechanism emerges in which amino-terminal anchoring via Leu1603 and carboxyl-terminal anchoring via auxiliary exosite interactions [56,78,79] act cooperatively in productive positioning of the Tyr1605-Met1606 scissile bond [80,81], which is geometrically constrained for maximum catalytic efficiency by confinement of Tyr1605 via the β3β4-loop in ADAMTS-13 (chapter 3).

Even under optimal conditions, catalytic turnover by ADAMTS-13 is relatively slow. It is particularly interesting to note that k_{cat} values of 0.14-1.3 s^{-1} measured for various different substrates ([56,78,82] and chapter 3) are of the same order of magnitude as the refolding rate constant of A2 (k_0 = 0.65 s^{-1} [58]), lending additional support to the hypothesis that once unfolding has activated A2 for proteolysis, the refolding rate of A2 is the major determinant for the time window during which it is possible for ADAMTS-13 to bind and cleave. The mechanism of recognition and cleavage of VWF by ADAMTS-13 appears to be highly specialized to the challenging environment under which this process occurs in vivo. First, ADAMTS-13 can bind VWF at exosites outside the A2 domain [83,84] and has been shown to be associated with VWF in plasma [84], suggesting that ADAMTS-13 could already be primed for binding and cleavage of A2 under sub-critical shear conditions. Second, ADAMTS-13 binds unfolded A2 tightly [78] and this interaction is characterized by fast on- and slow off-rates [82]. Since refolding of A2 restricts accessibility of the scissile bond, it is tempting to speculate that binding of ADAMTS-13 to A2 stabilizes the unfolded state of the A2 domain, decelerating refolding and increasing the available time window for cleavage to occur. Further, the slow off-rate implies that ADAMTS-13 can still bind cleaved A2 with significant affinity. The main determinant of this interaction is binding of carboxyl-terminal residues Glu1660-Arg1668 of A2 to the spacer domain of ADAMTS-13 [56], suggesting that the carboxyl-terminal cleavage product inhibits dissociation of ADAMTS-13 from the substrate and further proteolysis. Apart from A2 substrate activation and refolding dynamics, product inhibition possibly is a third regulatory element in balancing ADAMTS-13 cleavage.

Implications for von Willebrand disease

Physiological calcium concentrations determine unfolding and refolding dynamics of the A2 domain in the presence of force, suggesting an important role of calcium binding for the regulation of ADAMTS-13 cleavage *in vivo*. This hypothesis raises the questions whether mutations disturbing the structure and function of the calcium-binding site in A2 lead to the development of pathologic symptoms. To date, no mutations or naturally occurring sequence variations in the A2 domain have been mapped to residues directly involved in calcium binding [85]. However, such variations have been reported for VWF residues Pro1601 [86], Leu1603 [87,88] and Val1604 [89], which are located adjacent to residues acting as calcium ligands. Two mutations affecting these residues, Leu1603Pro and Val-1604Phe, are associated with type 2A von Willebrand disease [87-89]. In chapter 3 we have demonstrated that Leu1603Pro mutant impedes calcium binding and increases susceptibility to ADAMTS-13 cleavage by affecting stability of the A2 domain. Our results thus suggest that mutations causing disruption of calcium binding may be a relevant risk factor of type 2A von Willebrand disease. Further support for this hypothesis may come from the prominent 2A mutation Arg1597Trp. Like Leu1603, Arg1597 is located within the calcium-binding $\alpha_3\beta_4$-loop and coordinates calcium via its main chain carbonyl oxygen. In addition, its side chain engages in a salt bridge, which presumably stabilizes the $\alpha_3\beta_4$-loop (chapter 2). It will be interesting to investigate whether abrogated calcium binding may also contribute to the phenotype observed for this mutant. Our results and considerations suggest that mutations impeding calcium binding in A2 predispose to the development of 2A VWD and provide an interesting starting point for additional studies involving multimeric VWF in flow assays and animal models, together with a detailed analysis of the multimer triplet patterns and platelet-derived VWF from patient samples to confirm our mechanistic hypothesis.

Conclusion

The identification and functional characterization of the calcium-binding site in the A2 domain has contributed important concepts to further our understanding of conformational dynamics in the regulation of ADAMTS-13 cleavage and haemostasis. By virtue of the significant advances in apprehending other aspects of VWF function in relation to shear flow [12,13,16,23,90-92], our model view of the molecular processes underlying platelet adhesion and aggregation has has greatly improved. However, several conceptual challenges remain. The susceptibility of VWF multimers to shear-induced conformational changes is evident [16]. Experimental evidence that such globule-stretch transitions are indeed the activation trigger for platelet binding remains, however, still elusive. Single-molecule studies have highlighted the relevance of the structural dynamics that lie at the basis of the force-dependence of A1-GPIα interaction [30,91,93] and ADAMTS-13 cleavage (chapter 2, [17,58,94]). Nevertheless, our understanding of how these concepts integrate into the mosaic domain architecture of VWF and larger-scale conformational dynamics in shear flow is still very limited.

References

1. Savage B, Saldívar E, Ruggeri ZM (1996) Initiation of platelet adhesion by arrest onto fibrinogen or transloca tion on von Willebrand factor. *Cell* **84**: 289–297.
2. Moake JL, Turner NA, Stathopoulos NA, Nolasco LH, Hellums JD (1986) Involvement of large plasma von Willebrand factor (vWF) multimers and unusually large vWF forms derived from endothelial cells in shear stress-induced platelet aggregation. *J Clin Invest* **78**: 1456–1461. doi:10.1172/JCI112736.
3. Sakariassen KS, Bolhuis PA, Sixma JJ (1979) Human blood platelet adhesion to artery subendothelium is mediated by factor VIII-Von Willebrand factor bound to the subendothelium. *Nature* **279**: 636–638.
4. Sadler JE (2005) New concepts in von Willebrand disease. *Annu Rev Med* **56**: 173–191.
5. Moake JL, Rudy CK, Troll JH, Weinstein MJ, Colannino NM, et al. (1982) Unusually large plasma factor VIII:von Willebrand factor multimers in chronic relapsing thrombotic thrombocytopenic purpura. *N Engl J Med* **307**: 1432–1435.
6. Zheng X, Sadler J (2008) Pathogenesis of Thrombotic Microangiopathies. *Annu Rev Pathol* **3**: 249–277
7. Wagner D, Marder V (1984) Biosynthesis of von Willebrand protein by human endothelial cells: processing steps and their intracellular localization. *J Cell Biol* **99**: 2123–2130.
8. C L Verweij, Diergaarde PJ, M Hart, H Pannekoek (1986) Full-length von Willebrand factor (vWF) cDNA en codes a highly repetitive protein considerably larger than the mature vWF subunit. *EMBO J* **5**: 1839–1847.
9. Sadler JE (2009) von Willebrand factor assembly and secretion. *J Thromb Haemost* **7** Suppl 1: 24-27
10. L A Sporn, V J Marder, D D Wagner (1986) Inducible secretion of large, biologically potent von Willebrand fac tor multimers. *Cell* **46**: 185–190.
11. Dong J-F, Moake JL, Nolasco L, Bernardo A, Arceneaux W, et al. (2002) ADAMTS-13 rapidly cleaves newly secreted ultralarge von Willebrand factor multimers on the endothelial surface under flowing conditions. *Blood* **100**: 4033–4039.
12. Alexander-Katz A, Schneider MF, Schneider SW, Wixforth A, Netz RR (2006) Shear-flow-induced unfolding of polymeric globules. *Phys Rev Lett* **97**: 138101.
13. Schneider SW, Nuschele S, Wixforth A, Gorzelanny C, Alexander-Katz A, et al. (2007) Shear-induced unfold ing triggers adhesion of von Willebrand factor fibers. *Proc Natl Acad Sci USA* **104**: 7899–7903.
14. Sing CE, Alexander-Katz A (2011) Giant nonmonotonic stretching response of a self-associating polymer in shear flow. *Phys Rev Lett* **107**: 198302.
15. Shankaran H, Neelamegham S (2004) Hydrodynamic forces applied on intercellular bonds, soluble molecules, and cell-surface receptors. *Biophys J* **86**: 576–588.
16. Sing CE, Alexander-Katz A (2010) Elongational flow induces the unfolding of von Willebrand factor at physi ological flow rates. *Biophys J* **98**: L35–L37.
17. Zhang X, Halvorsen K, Zhang C-Z, Wong WP, Springer TA (2009) Mechanoenzymatic cleavage of the ultra large vascular protein von Willebrand factor. *Science* **324**: 1330–1334.
18. Whittaker CA, Hynes RO (2002) Distribution and evolution of von Willebrand/integrin A domains: widely dis persed domains with roles in cell adhesion and elsewhere. *Mol Biol Cell* **13**: 3369–3387.
19. Sadler JE (1998) Biochemistry and genetics of von Willebrand factor. *Annu Rev Biochem* **67**: 395–424.
20. Fowler WE, Fretto LJ, Hamilton KK, Erickson HP, McKee PA (1985) Substructure of human von Willebrand fac tor. *J Clin Invest* **76**: 1491–1500.
21. Slayter H, Loscalzo J, Bockenstedt P, Handin RI (1985) Native conformation of human von Willebrand protein. Analysis by electron microscopy and quasi-elastic light scattering. *J Biol Chem* **260**: 8559–8563.
22. Siediecki C, Lestini B, Kottke-Marchant K, Eppell S, Wilson D, et al. (1996) Shear-dependent changes in the three-dimensional structure of human von Willebrand factor. *Blood* **88**: 2939–2950.
23. Zhou Y-F, Eng ET, Nishida N, Lu C, Walz T, et al. (2011) A pH-regulated dimeric bouquet in the structure of von Willebrand factor. *EMBO J* **30**: 4098–4111
24. O'Leary JM, Hamilton JM, Deane CM, Valeyev NV, Sandell LJ, et al. (2004) Solution structure and dynamics of a prototypical chordin-like cysteine-rich repeat (von Willebrand Factor type C module) from collagen IIA. *J Biol Chem* **279**: 53857–53866.
25. Zhang J-L, Qiu L-Y, Kotzsch A, Weidauer S, Patterson L, et al. (2008) Crystal structure analysis reveals how the Chordin family member crossveinless 2 blocks BMP-2 receptor binding. *Dev Cell* **14**: 739–750.
26. Ulrichts H, Udvardy M, Lenting PJ, Pareyn I, Vandeputte N, et al. (2006) Shielding of the A1 domain by the D'D3 domains of von Willebrand factor modulates its interaction with platelet glycoprotein Ib-IX-V. *J Biol Chem* **281**: 4699–4707.
27. Martin C, Morales LD, Cruz MA (2007) Purified A2 domain of von Willebrand factor binds to the active con formation of von Willebrand factor and blocks the interaction with platelet glycoprotein Ibalpha. *J Thromb Haemost* **5**: 1363–1370.
28. Tsai H, Sussman I, Nagel R (1994) Shear stress enhances the proteolysis of von Willebrand factor in normal plasma. *Blood* **83**: 2171–9.
29. Furlan M (1996) Von Willebrand factor: molecular size and functional activity. *Ann Hematol* **72**: 341–348.
30. Arya M, Kolomeisky A, Romo G, Cruz M, Lopez J, et al. (2005) Dynamic Force Spectroscopy of Glycoprotein Ib-IX and von Willebrand Factor. *Biophys J* **88**: 4391–4401.

31. Steppich DM, Angerer JI, Sritharan K, Schneider SW, Thalhammer S, et al. (2008) Relaxation of ultra large VWF bundles in a microfluidic-AFM hybrid reactor. *Biochem Biophys Res Commun* **369**: 507–512.

32. Sing C, Alexander-Katz A (2010) Globule– Stretch Transitions of Collapsed Polymers in Elongational Flow Fields. *Macromolecules* **43**: 3532–3541.

33. Ying J, Ling Y, Westfield LA, Sadler JE, Shao J-Y (2010) ScienceDirect.com - Biophysical Journal - Unfolding the A2 Domain of Von Willebrand Factor with the Optical Trap. *Biophys J* **98**: 1685–1693.

34. Bustamante C (2008) In singulo biochemistry: when less is more. *Annu Rev Biochem* **77**: 45–50.

35. Cecconi C, Shank E, Bustamante C, Marqusee S (2005) Direct observation of the three-state folding of a single protein molecule. *Science* **309**: 2057–2060.

36. Shank EA, Cecconi C, Dill JW, Marqusee S, Bustamante C (2010) The folding cooperativity of a protein is controlled by its chain topology. *Nature* **465**: 637–640.

37. Stigler J, Ziegler F, Gieseke A, Gebhardt JCM, Rief M (2011) The Complex Folding Network of Single Calmod ulin Molecules. *Science* **334**: 512–516.

38. Mickler M, Dima RI, Dietz H, Hyeon C, Thirumalai D, et al. (2007) Revealing the bifurcation in the unfolding pathways of GFP by using single-molecule experiments and simulations. *Proc Natl Acad Sci USA* **104**: 20268–20273.

39. Titani K, Kumar S, Takio K, Ericsson LH, Wade RD, et al. (1986) Amino acid sequence of human von Willebrand factor. *Biochemistry* **25**: 3171–3184.

40. Marti T, Rösselet SJ, Titani K, Walsh KA (1987) Identification of disulfide-bridged substructures within human von Willebrand factor. *Biochemistry* **26**: 8099–8109.

41. Katsumi A, Tuley E, Bodo I, Sadler J (2000) Localization of Disulfide Bonds in the Cystine Knot Domain of Hu man von Willebrand Factor. *J Biol Chem* **275**: 25585–25594.

42. Dong Z, Thoma RS, Crimmins DL, McCourt DW, Tuley EA, et al. (1994) Disulfide bonds required to assemble functional von Willebrand factor multimers. *J Biol Chem* **269**: 6753–6758.

43. Emsley J, Cruz M, Handin R, Liddington R (1998) Crystal structure of the von Willebrand Factor A1 domain and implications for the binding of platelet glycoprotein Ib. *J Biol Chem* **273**: 10396–10401.

44. Huizinga EG, Martijn van der Plas R, Kroon J, Sixma JJ, Gros P (1997) Crystal structure of the A3 domain of human von Willebrand factor: implications for collagen binding. *Structure* **5**: 1147–1156.

45. Zhang Q, Zhou Y-F, Zhang C-Z, Zhang X, Lu C, et al. (2009) Structural specializations of A2, a force-sensing domain in the ultralarge vascular protein von Willebrand factor. *Proc Natl Acad Sci USA* **106**: 9226–9231.

46. Emsley J, Cruz M, Handin R, Liddington R (1998) Crystal Structure of the von Willebrand Factor A1 Domain and Implications for the Binding of Platelet Glycoprotein Ib. *J Biol Chem* **273**: 10396–10401.

47. Springer TA (2006) Complement and the multifaceted functions of VWA and integrin I domains. *Structure* **14**: 1611–1616.

48. Milder FJ, Gomes L, Schouten A, Janssen BJC, Huizinga EG, et al. (2007) Factor B structure provides insights into activation of the central protease of the complement system. *Nat Struct Mol Biol* **14**: 224–228. doi:10.1038/nsmb1210.

49. Tozer EC, Liddington RC, Sutcliffe MJ, Smeeton AH, Loftus JC (1996) Ligand binding to integrin alphaIIbbeta3 is dependent on a MIDAS-like domain in the beta3 subunit. *J Biol Chem* **271**: 21978–21984.

50. Loftus JC, Liddington RC (1997) New insights into integrin-ligand interaction. *J Clin Invest* **100**: S77–S81.

51. Dutta A, Bahar I (2010) Metal-binding sites are designed to achieve optimal mechanical and signaling properties. *Structure* **18**: 1140–1148.

52. Wu T, Lin J, Cruz M, Dong J-F, Zhu C (2010) Force-induced cleavage of single VWFA1A2A3 tridomains by ADAMTS-13. *Blood* **115**: 370–8.

53. Ying J, Ling Y, Westfield LA, Sadler JE, Shao J-Y (2010) Unfolding the A2 domain of von Willebrand factor with the optical trap. *Biophys J* **98**: 1685–1693.

54. Springer TA (2011) Biology and physics of von Willebrand factor concatamers. *J Thromb Haemost* **9** Suppl 1: 130–143.

55. Popel AS, Johnson PC (2005) Microcirculation and Hemorheology. *Annu Rev Fluid Mech* **37**: 43–69.

56. Gao W, Anderson PJ, Majerus EM, Tuley EA, Sadler JE (2006) Exosite interactions contribute to tension-induced cleavage of von Willebrand factor by the antithrombotic ADAMTS13 metalloprotease. *Proc Natl Acad Sci USA* **103**: 19099–19104.

57. Soejima K, Nakamura H, Hirashima M, Morikawa W, Nozaki C, et al. (2006) Analysis on the molecular species and concentration of circulating ADAMTS13 in Blood. *J Biochem* **139**: 147–154.

58. Xu AJ, Springer TA (2012) Calcium stabilizes the von Willebrand factor A2 domain by promoting refolding. *Proc Natl Acad Sci USA* **109**: 3742–3747.

59. Wagner C, Kiefhaber T (1999) Intermediates can accelerate protein folding. *Proc Natl Acad Sci USA* **96**: 6716–6721.

60. Schwaiger I, Kardinal A, Schleicher M, Noegel AA, Rief M (2004) A mechanical unfolding intermediate in an actin-crosslinking protein. *Nat Struct Mol Biol* **11**: 81–85.

61. Schwaiger I, Schleicher M, Noegel AA, Rief M (2005) The folding pathway of a fast-folding immunoglobulin domain revealed by single-molecule mechanical experiments. *EMBO Rep* **6**: 46–51.

62. Schlierf M, Berkemeier F, Rief M (2007) Direct observation of active protein folding using lock-in force spec-

troscopy. *Biophys J* **93**: 3989–3998.

62. Forns N, de Lorenzo S, Manosas M, Hayashi K, Huguet JM, et al. (2011) Improving signal/noise resolution in single-molecule experiments using molecular constructs with short handles. *Biophys J* **100**: 1765–1774

64. de Messieres M, Brawn-Cinani B, La Porta A (2011) Measuring the folding landscape of a harmonically con strained biopolymer. *Biophys J* **100**: 2736–2744.

65. Baldauf C, Schneppenheim R, Stacklies W, Obser T, Pieconka A, et al. (2009) Shear-induced unfold - ing activates von Willebrand factor A2 domain for proteolysis. *J Thromb Haemost* **7**: 2096–2105.

66. Kokame K, Matsumoto M, Fujimura Y, Miyata T (2004) VWF73, a region from D1596 to R1668 of von Willebrand factor, provides a minimal substrate for ADAMTS-13. *Blood* **103**: 607–612.

67. Majerus EM, Anderson PJ, Sadler JE (2005) Binding of ADAMTS13 to von Willebrand factor. *J Biol Chem* **280**: 21773–21778.

68. Fowler SB, Best RB, Toca-Herrera JL, Rutherford TJ, Steward A, et al. (2002) Mechanical unfolding of a titin Ig domain: structure of unfolding intermediate revealed by combining AFM, molecular dynamics simulations, NMR and protein engineering. *J Mol Biol* **322**: 841–849.

69. Gao M, Craig D, Lequin O, Campbell ID, Vogel V, et al. (2003) Structure and functional significance of mechanically unfolded fibronectin type III1 intermediates. *Proc Natl Acad Sci USA* **100**: 14784–14789.

70. Peyvandi F, Palla R, Lotta LA, Mackie I, Scully MA, et al. (2010) ADAMTS-13 assays in thrombotic thrombocytopenic purpura. *J Thromb Haemost* **8**: 631–640.

71. Furlan M, Robles R, Lämmle B (1996) Partial purification and characterization of a protease from human plasma cleaving von Willebrand factor to fragments produced by in vivo proteolysis. *Blood* **87**: 4223–4234.

72. Tsai H (1996) Physiologic cleavage of von Willebrand factor by a plasma protease is dependent on its conformation and requires calcium ion. *Blood* **87**: 4235–4244.

73. Anderson PJ, Kokame K, Sadler JE (2006) Zinc and calcium ions cooperatively modulate ADAMTS13 activity. *J Biol Chem* **281**: 850–857.

74. Kokame K, Nobe Y, Kokubo Y, Okayama A, Miyata T (2005) FRETS-VWF73, a first fluorogenic substrate for ADAMTS13 assay. *Br J Haematol* **129**: 93–100.

75. van der Plas RM, Schiphorst ME, Huizinga EG, Hené RJ, Verdonck LF, et al. (1999) von Willebrand factor proteolysis is deficient in classic, but not in bone marrow transplantation–associated, thrombotic thrombocytopenic purpura. *Blood* **93**: 3798–3802.

76. Cruz MA, Whitelock J, Dong J-F (2003) Evaluation of ADAMTS-13 activity in plasma using recombinant von Willebrand Factor A2 domain polypeptide as substrate. *Thromb Haemost* **90**: 1204–1209.

77. Dent JA, Berkowitz SD, Ware J, Kasper CK, Ruggeri ZM (1990) Identification of a cleavage site directing the immunochemical detection of molecular abnormalities in type IIA von Willebrand factor. *Proc Natl Acad Sci USA* **87**: 6306–6310.

78. Gao W, Anderson P, Sadler J (2008) Extensive contacts between ADAMTS13 exosites and von Willebrand factor domain A2 contribute to substrate specificity. *Blood* **112**: 1713–9.

79. Ai J, Smith P, Wang S, Zhang P, Zheng XL (2005) The proximal carboxyl-terminal domains of ADAMTS13 determine substrate specificity and are all required for cleavage of von Willebrand factor. *J Biol Chem* **280**: 29428–29434.

80. Xiang Y, De Groot R, Crawley JTB, Lane DA (2011) Mechanism of von Willebrand factor scissile bond cleavage by a disintegrin and metalloproteinase with a thrombospondin type 1 motif, member 13 (ADAMTS13). *Proc Natl Acad Sci USA* **108**: 11602–11607.

81. Crawley JTB, De Groot R, Xiang Y, Luken BM, Lane DA (2011) Unraveling the scissile bond: how ADAMTS13 recognizes and cleaves von Willebrand factor. *Blood* **118**: 3212–3221.

82. Zanardelli S, Crawley JTB, Chion CKNCK, Lam JK, Preston RJS, et al. (2006) ADAMTS13 substrate recognition of von Willebrand factor A2 domain. *J Biol Chem* **281**: 1555–1563.

83. Zanardelli S, Chion ACK, Groot E, Lenting PJ, McKinnon TAJ, et al. (2009) A novel binding site for ADAMTS13 constitutively exposed on the surface of globular VWF. *Blood* **114**: 2819–2828.

84. Feys HB, Anderson PJ, Vanhoorelbeke K, Majerus EM, Sadler JE (2009) Multi-step binding of ADAMTS-13 to von Willebrand factor. *J Thromb Haemost* **7**: 2088–2095.

85. ISTH-SSC VWF Online Database http://www.vwf.group.shef.ac.uk/. Accessed 4 May 2012.

86. Pruss CM, Notley CRP, Hegadorn CA, O'Brien LA, Lillicrap D (2008) ADAMTS13 cleavage efficiency is altered by mutagenic and, to a lesser extent, polymorphic sequence changes in the A1 and A2 domains of von Willebrand factor. *Br J Haematol* **143**: 552–558.

87. Enayat M, Guilliatt A, Bradbury M, Tait R, Williams M, et al. (2006) Five novel candidate mutations in type 2A, 2M and 2N von Willebrand disease patients from the west of Scotland. *Br J Haematol* **133**: 41.

88. Berber E, Pehlevan F, Akin M, Yalcin Capan O, Kavakli K, et al. (2012) A Common VWF Exon 28 Haplotype in the Turkish Population. *Clin Appl Thromb Hemost* [Epub ahead of print]

89. Meyer D, Fressinaud E, Gaucher C, Lavergne JM, Hilbert L, et al. (1997) Gene defects in 150 unrelated French cases with type 2 von Willebrand disease: from the patient to the gene. INSERM Network on Molecular Abnormalities in von Willebrand Disease. *Thromb Haemost* **78**: 451–456.

90. Chen H, Alexander-Katz A (2011) Polymer-based catch-bonds. *Biophys J* **100**: 174–182.

91. Kim J, Zhang C-Z, Zhang X, Springer TA (2010) A mechanically stabilized receptor-ligand flex-bond important in the vasculature. Nature 466: 992–995.

Nederlandse samenvatting

Als men zich te diep snijdt, gaat het bloeden. Na een beschadiging van de vaatwand zet ons lichaam een reeks mechanismen in gang om het bloedverlies in te perken. Een normaal functionerend bloedstollingproces is dan ook van levensbelang. De allereerste stap in het stoppen van de bloeding en het begin van wondheling is de vorming van een prop die uit bloedplaatjes bestaat. Onder invloed van het collageen dat bloot komt te liggen ten gevolge van een beschadiging van de vaatwand worden bloedplaatjes aangetrokken naar de wond. Deze bloedplaatjes worden geactiveerd om zich, door middel van eiwitten op hun celoppervlak, op de plaats van de wond te hechten aan de beschadigde vaatwand, waarna ze samen klonteren en zo het gat dichten. Op moleculair niveau is dit proces een gecompliceerd samenspel van moleculen en cellen.

Adhesie, oftewel het hechten van bloedplaatjes aan de vaatwand, wordt beïnvloed door de stroomsnelheid en door afschuifkrachten in de bloedstroom. Op moleculair niveau maken deze krachten van de stevige verankering van bloedplaatjes aan de beschadigde vaatwand een hele klus. Dit geldt in het bijzonder in haarvaten en kleine slagaders. Hier zijn door de kleine diameters de afschuifkrachten namelijk buitengewoon hoog. Dit heeft ten eerste als gevolg dat er voortdurend scheuren in de gevoelige binnenste cellaag van het bloedvat ontstaan. Daarnaast werken de afschuifkrachten de adhesie van bloedplaatjes aan de beschadigde vaatwand aanzienlijk tegen, waardoor vaak geen bloedstelpende prop gevormd kan worden. Onder dergelijke omstandigheden helpt het eiwit von Willebrand factor (VWF) de bloedplaatjes om zich toch aan de beschadigde vaatwand te hechten door te werken als een soort eiwitlijm.

VWF is een lange eiwitketen bestaande uit een groot aantal repeterende eenheden. In elk van die afzonderlijke eenheden heeft VWF bindingsplaatsen voor het collageen, dat bloot komt te liggen aan de beschadigde vaatwand, en het eiwit GPIbα, dat op het celoppervlak van bloedplaatjes zit. Zijn structuur stelt dit eiwit dus in staat als een soort klittenband bloedplaatjes in contact te brengen met de beschadigde vaatwand. Hoewel VWF en GPIbα beide in de bloedbaan voorkomen, binden ze normaal niet aan elkaar. Hoe kan dat? VWF strengen circuleren in het bloed opgevouwen tot een soort bol, en in die toestand zitten de bindingplaatsen voor plaatjesreceptoren opgesloten in de kern van de bol. In deze toestand, of conformatie, kan VWF dus geen bloedplaatjes binden. In aanwezigheid van hoge afschuifkrachten in het bloed ondergaat VWF echter een structurele verandering van een inactieve, bolvormige toestand in een actieve, uitgerekte vorm. Als het ware veranderd de bol in een lange sliert. Hierdoor legt VWF zijn bindingsplaatsen voor GPIbα bloot en werkt het als een soort landingsbaan voor bloedplaatjes, waarop ze al rollende kunnen afremmen. Hierna kunnen de bloedplaatjes steviger hechten en vormen ze een prop die de bloeding stopt.

Het ligt voor de hand dat dit proces nauw gereguleerd moet worden. Bloedplaatjesadhesie door VWF is essentieel voor vorming van een bloedstelpende prop, maar bij een

overdreven reactie dreigt het bloedvat afgesloten te raken. Het opmerkelijke aan het regulatiemechanisme van VWF is dat het vermogen van VWF om aan de plaatjesreceptor GPIbα te binden door krachten in de bloedstroom gemoduleerd blijkt te worden.

Hoofdstuk 1 levert een overzicht van de huidige kennis van VWF-afhankelijke bloedplaatjesadhesie en de rol van hydrodynamische krachten in de regulatie van dit proces. Dit hoofdstuk vormt daarmee de basis van de volgende hoofdstukken, waarin de moleculaire mechanismen van het effect dat mechanische krachten op de conformatie van VWF blijken te hebben in detail bestudeerd worden.

In **hoofdstuk 2** beschrijven we de driedimensionale structuur van het A2 domein van VWF op atomair niveau. De structuur konden we bepalen door gebruik te maken van röntgen diffractie. Het A2 domein is een onderdeel van VWF dat een knipsite voor het enzym ADAMTS-13 heeft. Dit enzym kan multimere VWF ketens in kleinere stukken knippen, waardoor ze minder goed aan bloedplaatjes binden. Afbraak van lange VWF strengen door ADAMTS-13 is dus een regulatiemechanisme dat het plaatjesbindende vermogen van VWF mede bepaalt.

Uit de structuur blijkt dat het A2 domein op een cruciale plek een calcium ion bindt. Door middel van simulaties konden we aantonen dat dit calcium ion de aminozuurketen van het A2 domein in een compacte driedimensionale structuur stabiliseert waarin de knipplek voor ADAMTS-13 in de kern van het eiwit verborgen ligt. Eerder was al aangetoond dat de aminozuurketen van het eiwit open moet vouwen om de knipsite bloot te leggen. Calcium zorgt ervoor dat dit minder gemakkelijk gebeurt.

Zoals reeds beschreven functioneert VWF in de dynamische omgeving van de bloedbaan en werken er voortdurend mechanische krachten op het eiwit in. Als VWF op collageen vast komt te zitten en er vervolgens bloedplaatjes aan VWF binden, is het daar net een soort touwtrekken aan die VWF strengen. Om te onderzoeken of calcium binding ook onder dergelijke omstandigheden het A2 domein beschermt voor open vouwen en de knip door ADAMTS-13 hebben we een optisch pincet gebruikt om de krachten in de bloedstroom na te bootsen en aan afzonderlijke A2 moleculen te trekken. In deze opstelling zitten de uiteinden van het eiwit gekoppeld aan twee minuscule polystyreen kraaltjes waarvan er een met een laserbundel werd vastgegrepen en de ander op een miljoenste meter nauwkeurig mechanisch kon worden aangestuurd. Op die manier konden we het eiwit tussen die kraaltjes strak spannen en konden we de krachten meten die nodig zijn om het A2 domein te ontvouwen. Uit deze proeven bleek dat calcium ook de mechanische eigenschappen van het A2 domein fundamenteel beïnvloedt. Vergeleken met proeven zonder calcium zijn in aanwezigheid van calcium hogere krachten nodig om het A2 domein te ontvouwen en de knipplaats bloot te leggen. Bovendien blijkt calcium ook nog eens te bevorderen dat het A2 domein zich weer netjes op kan vouwen als de kracht iets minder wordt. Dit heeft belangrijke gevolgen voor het regulatiemechanisme van VWF dat ten grondslag ligt aan zijn bloedstelpende functie. Lange VWF strengen zijn het efficiëntst in het verzamelen van bloedplaatjes in de omgeving van een plaatselijke wond. Hoe korter de strengen, hoe slechter ze bloedplaatjes binden. Het is dus belangrijk dat in de acute fase van wondheling voornamelijk lange VWF strengen in het bloed circuleren die heel

efficiënt bloedplaatjes bijeen kunnen rapen. Werkt dit proces echter te goed dan dreigt trombose. Omdat de kracht op VWF strengen groter wordt naarmate het aantal gebonden bloedplaatjes toeneemt, is de kans dat de kracht zodanig groot wordt dat het A2 domein ontvouwt het grootst voor de langste strengen. Die worden dan ook bij voorkeur door ADAMTS-13 geknipt.

Uit onze kristalstructuur blijkt ook dat de bindingsite voor calcium voor het grootste deel gevormd wordt door een lus van opeenvolgende aminozuren vlak vóór de plek waar ADAMTS-13 kan knippen. Bovendien blijkt dat in sommige patiënten met een bloedingsneiging een aantal van aminozuren in die lus gemuteerd zijn in een ander aminozuur. Gezien het belang van calcium binding voor de regulatie van VWF suggereert dit, dat deze mutaties mogelijk de binding van calcium aan het A2 domein beïnvloeden. In het onderzoek zoals beschreven in **hoofdstuk 3** hebben we deze hypothese met biochemische methodes getoetst. Onze proeven laten zien dat één van die mutaties de structuur van de calcium bindende lus op een manier lijkt te veranderen dat calcium niet meer aan het A2 domein kan binden. Hierdoor wordt, zoals we in hoofdstuk 2 hebben aangetoond, het A2 domein gevoeliger voor ontvouwing door de bloedstroom en kunnen VWF strengen dus makkelijker door ADAMTS-13 worden opgeknipt. Dit heeft weer tot gevolg dat er uiteindelijk voornamelijk heel korte VWF ketens in het bloed circuleren die dan ook niet erg efficiënt zijn in het binden van bloedplaatjes. Dat verhoogt de kans op bloedingen. Onze waarnemingen leiden dus tot te conclusie dat verstoorde calcium binding één mogelijke verklaring voor de bloedingsneiging van deze patiënten zou kunnen zijn. Dit verband onderstreept eens te meer een belangrijke functie van calcium in het krachtafhankelijke regulatiemechanisme van bloedstelping door VWF.

Tot slot beschrijven we in **hoofdstuk 4** een nieuwe methode die we hebben geïntroduceerd om op een eenvoudige manier stukken DNA aan elkaar te plakken. Dit soort technieken zijn van groot belang voor het doelgericht ontwerpen van eiwitten. DNA bouwstenen bevatten de blauwdruk voor de unieke volgorde van de individuele aminozuren die een eiwitketen vormen. Door stukken DNA aan elkaar te plakken kan men dus de blauwdruk voor nieuwe eiwitten maken. Een beperking van de in hoofdstuk 2 beschreven proeven met de optisch pincet is bijvoorbeeld dat men voor een enkele waarneming soms heel vaak moet meten. Dit komt omdat men aan enkele moleculen meet, die vanzelfsprekend niet altijd makkelijk te vinden zijn. Als je nu een reeks identieke eiwitmoleculen achter elkaar zet en vervolgens strak spant met de optisch pincet kun je met één meting aan één enkel molecuul een aantal vergelijkbare waarnemingen doen. Dat bespaart veel tijd. Om zulke repeterende eiwitten te maken moet men dus eerst een keten van identieke stukken DNA in elkaar zetten. Er zijn tal van methodes ontwikkelt om dit te doen, maar deze zijn allemaal niet bijzonder efficiënt. Wij wisten dat in de chemische synthese vergelijkbare probleemstellingen bestaan en dat daar wel efficiënte methodes zijn ontwikkelt om dit soort moleculen te maken. We hebben dus concepten uit de chemische synthese toegepast op het aan elkaar plakken van DNA bouwstenen en het bleek dat onze methode het proces aanzienlijk kon bespoedigen.

Dankwoord

Ik weet heel goed dat de lezer helemaal niet zo'n behoefte heeft dit allemaal te weten, maar ik heb er behoefte aan hun dit te vertellen. Jean-Jacques Rousseau, de auteur van deze zin, wist vast niet dat hij een aardige omschrijving zou geven van wat er soms door je hoofd spookt als je een proefschrift schrijft. Gelukkig geldt het eerste zinsdeel niet voor alle lezers en al beslist niet voor dit deel van het proefschrift. Ik heb de afgelopen jaren met veel plezier onderzoek gedaan. Iedereen die op enige wijze heeft bijgedragen aan de totstandkoming van dit boekje wil ik op deze plaats bedanken, waarvan een aantal mensen in het bijzonder.

Eric, jouw enthousiasme, betrokkenheid en kennis hebben veel bijgedragen aan dit werk. Bedankt dat ik ten alle tijden bij je binnen kon lopen voor advies en discussie. Je hebt mij alle kansen gegeven om me te ontwikkelen als wetenschapper door mij en mijn ideeën altijd serieus te nemen. Dank voor het vertrouwen, we vormden een goed team. Piet, vaak waren we 's ochtends de eersten op het lab maar nog niet helemaal klaar voor het grote werk. Het was dan altijd een plezier om even de wereld met je door te nemen. Je deur stond altijd open en het kritisch volgen van mijn verrichtingen hield ons scherp, bedankt.

Sander, jouw optisch pincet speelt een belangrijke rol in dit proefschrift. Bedankt voor de samenwerking. Alireza, your company turned the long days at AMOLF into diverting hours. Thanks for sharing your expertise and help. Flip en Jan, dankzij jullie konden we onze biofysische theorieën vaak weer in de juiste context zetten. Rolf, bedankt voor de Biacore lessen. Hopelijk pakken je kristallografie plannen uiteindelijk nog uit. Aike, helaas niet in dit proefschrift terecht gekomen, heb ik toch veel van onze TIRF experimenten geleerd.

Arie, op congressen de laatste in de bar en als eerste bij het ontbijt. Je stond altijd klaar om te helpen en aan humor geen tekort, bedankt. Martin, de koffietafel bij K&S was minder legendarisch zonder jouw scherpe kijk op de Nederlandse samenleving. Bedankt voor de inleiding kleine stof (ehm, hoge resolutie) kristallografie. Toine, door de herrie van mijn simulaties kreeg je op je kamer nogal wat te verduren. Bedankt voor de vele trucjes en scriptjes die je me hebt geleerd. Loes, helaas was je poging om van mij een tenniskampioen te maken tevergeefs. Het was wel altijd gezellig. Cécile, de afdeling heeft wel geboft met een secretaresse zoals jij, bedankt.

Mijn paranimfen. Dennis, ik had me geen betere kamergenoot voor kunnen stellen. Rondje Ijsselmeer (kan in één dag, toch?), Bergkirchweih Erlangen (ooh, schöne Bärli!), Bhut Jolokia op broodje kaas en fanatieke squash partijen. Het was en blijft altijd lachen. Fijn dat je achter me staat als paranimf. Tom, I will never forget the surreal pub crawl in Antwerp. At that time none of us knew that this was only the beginning of a series. Our cycling trips were great fun. Luckily you could not see my heart rate when I was trying to keep up with you (stroopwafels vs. karnemelk?). Looking forward to the next ride.

Samen onderzoek doen is vele malen leuker dan alleen. Talloze discussies met collega's op de gang, op de fiets, in de kroeg en tijdens de koffie hebben veel bijgedragen aan mijn proeven. Ook zorgden die collega's en hun humor ervoor dat ik iedere dag met veel plezier naar mijn werk ging. Iedereen bedankt hiervoor. Michael, de wekelijkse squashavonden en de daaran verbonden kroegentochten waren een onuitputtelijke bron van inspiratie en dit beslist niet beperkt tot wetenschap. Mooi dat je weer in Utrecht bent. Jin, thanks for the birthday cake at ID23-2. You probably did not know what you started by taking me to a Szichuan restaurant. Els, ook voor jou zit het er nu bijna op. Succes met afronden. Eddie, nooit iemand gezien die zo lang in bad ligt. Bedankt voor het gidsen in de Arnhemse heuvels. Louris, met André Hazes groeien de kristallen nog sneller. Harma, jouw kennis van de moleculaire biologie kwam vaak goed van pas. Succes in Groningen. Xiaoguang, master of bewildering poems. Thanks for the Chinese lessons. Peng, I much appreciated your guide to Singapore's secrets. If you would only run a little you could beat anyone at squash. Federico, always good fun to see the world through the eyes of an Italian. Thanks for cheese and chocolates. Chris, blobology is a contagious disease. Pramod and Ramesh, you significantly improved my knowledge of Indian delights. De UPE ploeg, Wieger, Roland en Lucio: Geen eiwit zonder jullie cellen. Bedankt ook voor de humor aan de koffietafel. Studenten Remco en Matti, bedankt voor jullie inzet en enthousiasme. Nu allebei zelf AIO, dat maakt me wel een beetje trots. Bert, succes me je eigen groep.

I have much enjoyed the squash shoot-outs with the "Magneto-Men": Adrien, Mikael, Andrea, Christoph and Marie, *Merci* for always standing up to defend your honor. Klaartje, jouw metingen leverden het bewijs dat calcium werkelijk bindt, bedankt. Gert, mijn eerste thermofluor experiment vormde uiteindelijk de basis voor dit proefschrift. Bedankt dat de deur bij NMR altijd open stond voor proeven doen en grappen maken.

I shared many memorable moments with friends from Utrecht and abroad: Catalina, Adriaan, Anne, Hugo, Roman, Natalia, Juan, Monica, Ana, Bea, Paola, Francesca, Sigrid, Nikola, Nada, Gérman, Asia, Becky, Sylvia, Meritxell, Serena, Elif, Axel, Cata, Houjiang, Kathrin, Julia, Bruno, Nico, Peter. Dank jullie wel! Het tennisclubje Hans, Eric, Rob en Bert, het was altijd goed om de dingen weer even te relativeren. Familie was er gelukkig ook: David, Rosanne, Mirjam, bedankt voor de gezellige etentjes, zeilen, Noorwegen en spannende verhalen uit China, Nepal en waar dan ook. Anneke en Tet, ook jullie kwamen altijd even kijken als jullie in Utrecht waren, bedankt. Esteban, Hector, Javier. I cannot imagine living with better friends than you.

Papa, Mama, Kai-Marten en Minke. Waarschijnlijk is het nooit helemaal duidelijk geworden wat ik daar nou precies deed met die eiwitten en of dat nou zo belangrijk was. Desondanks bleven jullie onophoudelijk vragen of er al kristallen waren, en juichten jullie mee toen die er eindelijk kwamen. Vaak was ik zo druk dat er weinig tijd overbleef voor thuis. Ik zou hier niet staan zonder jullie. Dank voor alles. Jessica, jij ook bedankt. Als we samen zijn is het goed.

Arjen

Curriculum Vitae

Arjen Jakobi werd geboren op 29 oktober 1980 te Wiesbaden, Duitsland. In 2002 begon hij met de studie Molecular Science aan de Friedrich-Alexander Universität Erlangen-Nürnberg. In 2005 sloot hij het laatste jaar van zijn bachelor af aan de Universiteit Leiden. Zijn bacheloronderzoek deed hij bij het Leiden/Amsterdam Center of Drug Research, waar onder begeleiding van Prof. Dr. Erik Biessen onderzoek werd verricht naar de rol van vetzuurbindende eiwitten bij aderverkalking. Vervolgens zette hij zijn studie voort in Erlangen. Hierbij werden twee afstudeerstages gelopen. Bij de vakgroep Computational Chemistry werd onder begeleiding van Dr. Harald Lanig het inductiemechanisme van DNA repressor eiwitten met moleculaire dynamica onderzocht. De tweede stage deed hij bij de afdeling Discovery Chemistry van F. Hoffmann-La Roche in Basel, Zwitserland. Hier werd onder begeleiding van Dr. Harald Mauser en Prof. Timothy Clark en computerprogramma ontwikkeld dat door middel van kwantummechanische berekeningen bindingseigenschappen van molecuulfragmenten voorspelt. Na het behalen van zijn diploma startte hij in Juni 2007 als assistent in opleiding bij de vakgroep Kristal- en Structuurchemie aan de Universiteit Utrecht waar het in dit proefschrift beschreven onderzoek werd verricht onder begeleiding van Dr. Eric Huizinga. Sinds Mei 2012 is hij als postdoctoraal onderzoeker werkzaam bij het European Molecular Biology Laboratory (EMBL) in Heidelberg en Hamburg.